AFRL-PR-WP-TR-2000-2118

NUMERICAL ANALYSIS OF FULLY DEVELOPED LAMINAR FLOW IN TRAPEZOIDAL AND SINUSOIDAL GROOVES WITH SHEAR STRESS AT THE LIQUID-VAPOR INTERFACE

SCOTT K. THOMAS
RICHARD C. LYKINS
KIRK L. YERKES

WRIGHT STATE UNIVERSITY
DEPT. OF MECHANICAL AND MATERIALS ENGINEERING
DAYTON, OHIO 45435-0001

SEPTEMBER 2000

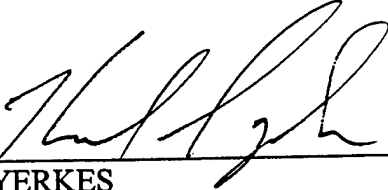INTERIM REPORT FOR PERIOD 21 AUGUST – 20 AUGUST 2000
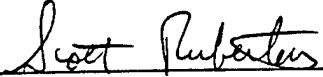
20010226 048

NOTICE

USING GOVERNMENT DRAWINGS, SPECIFICATIONS, OR OTHER DATA INCLUDED IN THIS DOCUMENT FOR ANY PURPOSE OTHER THAN GOVERNMENT PROCUREMENT DOES NOT IN ANY WAY OBLIGATE THE US GOVERNMENT. THE FACT THAT THE GOVERNMENT FORMULATED OR SUPPLIED THE DRAWINGS, SPECIFICATIONS, OR OTHER DATA DOES NOT LICENSE THE HOLDER OR ANY OTHER PERSON OR CORPORATION; OR CONVEY ANY RIGHTS OR PERMISSION TO MANUFACTURE, USE, OR SELL ANY PATENTED INVENTION THAT MAY RELATE TO THEM.

THIS REPORT IS RELEASABLE TO THE NATIONAL TECHNICAL INFORMATION SERVICE (NTIS). AT NTIS, IT WILL BE AVAILABLE TO THE GENERAL PUBLIC, INCLUDING FOREIGN NATIONS.
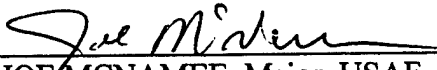
THIS TECHNICAL REPORT HAS BEEN REVIEWED AND IS APPROVED FOR PUBLICATION.

KIRK YERKES
Mechanical Engineer
Power Generation & Thermal Branch

SCOTT RUBERTUS
Chief
Power Generation & Thermal Branch

JOE MCNAMEE, Major, USAF
Deputy Chief
Power Division

Do not return copies of this report unless contractual obligations or notice on a specific document requires its return.

REPORT DOCUMENTATION PAGE

Public reporting burden for this collection of information is estimated to average 1 hour per response, including the time for reviewing instructions, searching existing data sources, gathering and maintaining the data needed, and completing and reviewing the collection of information. Send comments regarding this burden estimate or any other aspect of this collection of information, including suggestions for reducing this burden, to Washington Headquarters Services, Directorate for Information Operations and Reports, 1215 Jefferson Davis Highway, Suite 1204, Arlington, VA 22202-4302, and to the Office of Management and Budget, Paperwork Reduction Project (0704-0188), Washington, DC 20503.

1. AGENCY USE ONLY (Leave Blank)	2. REPORT DATE SEPTEMBER 2000	3. REPORT TYPE AND DATES COVERED INTERIM REPORT FOR 08/21/1999 - 08/20/2000

4. TITLE AND SUBTITLE
NUMERICAL ANALYSIS OF FULLY DEVELOPED LAMINAR FLOW IN TRAPEZOIDAL AND SINUSOIDAL GROOVES WITH SHEAR STRESS AT THE LIQUID-VAPOR INTERFACE

5. FUNDING NUMBERS
C   F33615-98-1-2844
PE   62203
PR   3145
TA   20
WU   C5

6. AUTHORS
SCOTT K. THOMAS
RICHARD C. LYKINS
KIRK L. YERKES

7. PERFORMING ORGANIZATION NAME(S) AND ADDRESS(ES)
WRIGHT STATE UNIVERSITY
DEPARTMENT OF MECHANICAL AND MATERIALS ENGINEERING
DAYTON, OHIO 45435-0001

8. PERFORMING ORGANIZATION REPORT NUMBER

9. SPONSORING / MONITORING AGENCY NAME(S) AND ADDRESS(ES)
PROPULSION DIRECTORATE
AIR FORCE RESEARCH LABORATORY, AIR FORCE MATERIEL COMMAND
WRIGHT-PATTERSON AFB, OHIO 45433-7251
POC: KIRK L. YERKES, AFRL/PRPG, 937-255-6241

10. SPONSORING / MONITORING AGENCY REPORT NUMBER
AFRL-PR-WP-TR-2000-2118

11. SUPPLEMENTARY NOTES

12a. DISTRIBUTION / AVAILABILITY STATEMENT
APPROVED FOR PUBLIC RELEASE, DISTRIBUTION UNLIMITED.

12b. DISTRIBUTION CODE

13. ABSTRACT (Maximum 200 words)

The primary goal of the present research was to numerically determine the behavior of fully developed laminar flow of trapezoidal and sinusoidal grooves with shear stress at the liquid-vapor interface. A computer model was developed using a finite difference solution which finds the mean velocity, Poiseuille number, and volumetric flow rate in terms of the groove geometry, meniscus contact angle, and interfacial shear stress for flow in trapezoidal and sinusoidal grooves. A comparison with archival literature is provided for fully developed laminar flow in rectangular and sinusoidal ducts and rectangular and triangular grooves. An extensive parametric analysis was performed. A semi-analytical solution is presented for the dimensionless mean velocity as a function of dimensionless shear stress, and was used in computing the capillary limit in axially grooved, revolving heat pipes. A previously written code to compute the capillary limit in revolving heat pipes was updated to include the effects of groove fill ratio and interfacial shear stress, and a comparison with experimental data is provided.

14. SUBJECT TERMS
Heat pipe, Revolving, Laminar Flow, Grooves, Working Fluid Inventory

15. NUMBER OF PAGES
96

16. PRICE CODE

17. SECURITY CLASSIFICATION OF REPORT UNCLASSIFIED	18. SECURITY CLASSIFICATION OF THIS PAGE UNCLASSIFIED	19. SECURITY CLASSIFICATION OF ABSTRACT UNCLASSIFIED	20. LIMITATION OF ABSTRACT SAR

NSN 7540-01-280-5500

Standard Form 298 (Rev. 2-89)
Prescribed by ANSI Std. Z39-1
298-102

i

Contents

iv

List of Figures

List of Tables

1 Fully Developed Laminar Flow in Trapezoidal Grooves

1.1 Introduction

Internally grooved ducts are used in process equipment to improve heat transfer during condensation and evaporation. In some cases, such as a refrigeration cycle evaporator or condenser with internal grooves, the vapor flow is cocurrent with respect to the liquid flow. In axially grooved heat pipes, the vapor flow is countercurrent to the liquid flow. The interfacial shear stress due to the cocurrent or countercurrent vapor flow contributes to the liquid pressure drop, which can significantly affect the heat transfer capacity of the grooved surface. The objective of the present research was to numerically model the flow of liquid in trapezoidal grooves using a finite difference approach in order to provide accurate information on the effects of cocurrent and countercurrent vapor flow on the pressure drop in the liquid. This geometry was chosen due to the fact that rectangular and triangular grooves are special cases of the trapezoidal groove, thus making the analysis as general as possible.

DiCola (1968) solved the conservation of momentum equation for the laminar flow of liquid in rectangular grooves with a uniform shear stress imposed at the liquid-vapor interface using separation of variables. Unfortunately, this manuscript is no longer available in the open literature. Schneider and DeVos (1980) provided the exact solution determined by DiCola (1968), along with an expression for the friction factor which approximates the exact solution to within 1% by using the first term of the infinite series solution. This expression was used by Schneider and DeVos to determine the nondimensional heat transport capacity of axially-grooved heat pipes. Upon examination of the DiCola equation, it is obvious that the rectangular groove is completely full; i.e., the meniscus contact angle is $\phi = 90°$.

Ayyaswamy et al. (1974) used the Galerkin boundary method to solve the Poisson equation to determine the fluid velocity in triangular grooves. In this study, interfacial

shear stress was zero, and the groove half-angle and contact angle were varied from $\theta = 5$ to $60°$ and $\phi = 0.1°$ to the full groove condition $(\theta + \phi = 90°)$. The results were presented graphically and in tabular form, which included the cross-sectional area, mean velocity, hydraulic diameter, and Poiseuille number. It was found that the Poiseuille number increased monotonically with meniscus contact angle.

Ma et al. (1994) determined the Poiseuille number for the flow of liquid in triangular grooves with liquid-vapor frictional interaction. The groove half-angle ranged from $20 \le \theta \le 60°$ and the meniscus contact angle was varied from $\phi = 0$ to $60°$. The conservation of momentum equation was transformed into the Laplace equation in terms of liquid velocity, which was solved using separation of variables and linear superposition. Difficulties were encountered with respect to application of the liquid-vapor interface boundary condition, since the liquid-vapor interface velocity is an unknown function of the vapor velocity. The methodology used to overcome this difficulty required an experimentally determined coefficient. A dimensionless liquid-vapor interface flow number was introduced to account for the interfacial shear stress. This value determined the relative velocities of the liquid and vapor at the liquid-vapor interface, which impacted the magnitude of the Poiseuille number. It was found that the friction factor increased with the interface flow number and contact angle. Results from the experiment executed by Ayyaswamy et al. (1974) for no liquid-vapor shear stress showed an excellent comparison with the analytical solution over the ranges of groove half-angle and contact angle mentioned above.

Romero and Yost (1996) analyzed the flow of liquid in a triangular groove with no shear stress at the liquid-vapor interface. In particular, the flow from a sessile drop into the groove was of interest. A nonlinear partial differential diffusion equation was presented which described the time-dependent height of liquid in the groove in terms of the groove geometry, meniscus contact angle, and fluid properties. A simplified similarity solution was presented for the region which was far from the sessile drop. A full similarity solution was also shown which accounted for the region near the fluid droplet. It was found that the wetting front position was proportional to $(Dt)^{1/2}$, where the diffusion coefficient D was related to the groove geometry, liquid viscosity,

2

and liquid-vapor surface tension.

Lin and Faghri (1997) modeled the flow of liquid in the triangular grooves of a rotating miniature heat pipe. A correlation for the friction factor was provided in terms of the shear stress at the liquid-vapor interface. The laminar flow in the triangular groove was solved using a finite element technique for side lengths ranging from $h\sqrt{1 + \tan^2\theta} = 0.2$ to 0.65 mm and liquid-vapor shear stress $\tau_{lv} = 7.7 \times 10^{-5}$ to 0.055 N/m^2 for a groove half-angle of $\theta = 20°$ and meniscus contact angle $\phi = 30°$. A regression analysis was used to represent the data to within $\pm 2.8\%$.

Khrustalev and Faghri (1999) analyzed the fully developed laminar flow of liquid and vapor in miniature heat pipes using a finite element solution. In particular, the case in which the vapor velocity was high and the cross-sectional areas of the vapor and liquid were comparable was of interest. It was assumed that, with respect to the vapor flow, the liquid velocity at the liquid-vapor interface was zero. For the liquid flow, the shear stress at the interface was equal and opposite to that of the vapor. This meant that the velocity gradient in the liquid was related to that of the vapor via a ratio of absolute viscosities. The momentum equation for the vapor domain was first solved to determine the shear stress distribution at the liquid-vapor interface. Then the momentum equation for the liquid domain was solved using the shear stress information from the vapor solution. The results presented were for a specific heat pipe geometry that matched a previous experimental study. It was found that the shear stress at the liquid-vapor interface was not uniform, being greater near the point of contact with the solid groove wall. This effect was more significant for smaller values of meniscus contact angle. In addition, the shear stress at the interface became more uniform as the vapor space became more restricted.

Kolodziej et al. (1999) analyzed the gravity-driven flow of liquid in a triangular groove with no shear at the liquid-vapor interface. The shape of the liquid-vapor interface was determined in terms of the Bond number and meniscus contact angle. Starting with the Young-Laplace relation, a nonlinear boundary-value problem for the liquid-vapor interface shape was solved. The flow field was then solved for the friction factor using the boundary collocation method. The range of parameters was

3

as follows: groove half-angle $\theta = 5$ to $70°$, meniscus contact angle $\phi = 5$ to $45°$, and Bond number Bo $= \rho g b^2/\sigma = 0.001, 0.01, 0.1, 1.0$ and 5.0, where b is the vertical distance from the liquid-vapor interface to the bottom of the groove. It was found that the Bond number had a significant effect on the friction factor of the flow.

The objective of the present study was to determine the mean velocity, volumetric flow rate, and Poiseuille number for the flow of liquid in trapezoidal grooves. The effect of vapor flowing over the liquid-vapor interface was accounted for by relating the liquid velocity gradient to the friction factor of the vapor. This approach assumed that the liquid velocity did not affect the vapor velocity; i.e., the vapor velocity at the interface was zero. In addition, the variation of the shear stress along the liquid-vapor interface (Khrustalev and Faghri, 1999) was neglected. The conservation of momentum equation was solved using Gauss-Seidel iteration with successive over-relaxation. The analysis was validated using the results of several previous studies including the flow of liquid in rectangular and triangular grooves with liquid-vapor interaction. The mean velocity, volumetric flow rate, and Poiseuille number are presented in graphical and tabular form in terms of the groove aspect ratio ($0 \leq \beta \leq 1.5$), groove half-angle ($0 \leq \theta \leq 60°$), meniscus contact angle ($0 \leq \phi \leq 90° - \theta$), and dimensionless shear stress at the liquid-vapor interface ($-0.45 \leq \tau_{lv}^* \leq 5.0$). The results were used to determine the effects of groove fill amount on the capillary limit of revolving helically-grooved heat pipes. The predictions of the improved capillary limit model were compared to the experimental data obtained by Castle et al. (2000).

1.2 Mathematical Model

A constant property liquid flows steadily in a trapezoidal groove as shown in Fig. 1. A meniscus, which is assumed to be circular, comprises the liquid-vapor interface (Bo $<< 1$). For fully developed laminar flow, $u = w = 0$ and $v = v(x, z)$.

4
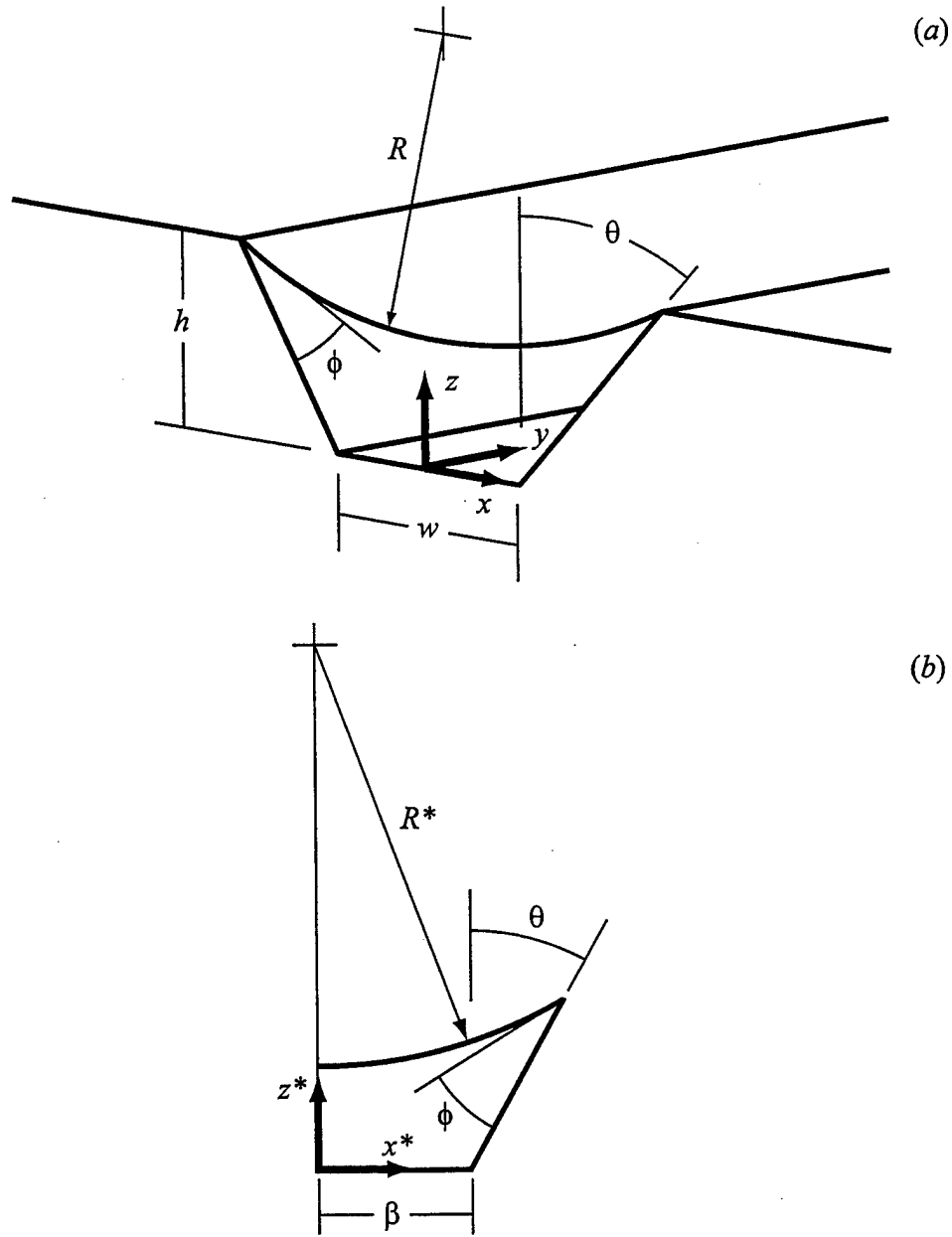
Figure 1: Flow of liquid in a trapezoidal groove: (a) Coordinate system; (b) Solution domain.

The conservation of mass and momentum equations reduce to (White, 1991)

$$\text{Continuity}: \quad \frac{\partial v}{\partial y} = 0$$

$$\text{Momentum}: \quad \frac{\partial^2 v}{\partial x^2} + \frac{\partial^2 v}{\partial z^2} = \frac{1}{\mu}\frac{\partial p}{\partial y} \tag{1}$$

$$\frac{\partial p}{\partial x} = \frac{\partial p}{\partial z} = 0$$

Since v is invariant with y, the pressure gradient $\partial p/\partial y$ is constant. Therefore, the conservation equations reduce to the classic Poisson equation.

$$\frac{\partial^2 v}{\partial x^2} + \frac{\partial^2 v}{\partial z^2} = \frac{1}{\mu}\frac{dp}{dy} \tag{2}$$

The dimensionless conservation of momentum equation and boundary conditions are presented below.

$$\frac{\partial^2 v^*}{\partial x^{*2}} + \frac{\partial^2 v^*}{\partial z^{*2}} = -1 \tag{3}$$

On the groove walls, the no-slip condition is in effect.

$$v^* = 0 : \quad \begin{cases} 0 \leq x^* \leq \beta, \quad z^* = 0 \\[2mm] \beta \leq x^* \leq \beta + \tan\theta, \quad z^* = (x^* - \beta)\cot\theta \quad \text{for} \quad \theta > 0 \\[2mm] x^* = \beta, \quad 0 \leq z^* \leq 1 \quad \text{for} \quad \theta = 0 \end{cases} \tag{4}$$

At the line of symmetry, the velocity gradient is zero in the x^* direction

$$\frac{\partial v^*}{\partial x^*} = 0 : \quad x^* = 0, \quad 0 \leq z^* \leq (1 + d^*) - R^* \tag{5}$$

where

$$d^* = R^*\sqrt{1 - \left(\frac{\beta + \tan\theta}{R^*}\right)^2} \tag{6}$$

The dimensionless radius of curvature is given by

$$R^* = \begin{cases} (\beta + \tan\theta)\sqrt{1 + \left[\cot\theta - \dfrac{\sin\phi}{\sin\theta\sin(\theta + \phi)}\right]^{-2}} \quad \text{for} \quad \theta > 0 \\[4mm] \beta\sec\phi \quad \text{for} \quad \theta = 0 \end{cases} \tag{7}$$

On the liquid-vapor interface, a uniform shear stress in the y direction is imposed.

$$\frac{\partial v^*}{\partial n^*} = \tau_{lv}^* : \; 0 \le x^* \le \beta + \tan\theta, \; z^* = (1 + d^*) - \sqrt{R^{*2} - x^{*2}} \qquad (8)$$

The dimensional liquid-vapor interface shear stress can be cast in terms of the friction factor of the vapor.

$$\tau_{lv} = \begin{cases} \left[\dfrac{\rho_v \, (\overline{v_v})^2}{2}\right] f_v & \text{for cocurrent flow} \\[4mm] -\left[\dfrac{\rho_v \, (\overline{v_v})^2}{2}\right] f_v & \text{for countercurrent flow} \end{cases} \qquad (9)$$

The Poiseuille number of the liquid in the groove is given by

$$\text{Po} = f\text{Re} = \frac{D_h^{*2}}{2\overline{v^*}} \qquad (10)$$

The dimensionless hydraulic diameter is

$$D_h^* = \begin{cases} 2\left[\beta + (\beta + \tan\theta)(1 + d^*) - R^{*2}\cos^{-1}\left(\dfrac{d^*}{R^*}\right)\right](\beta + \sec\theta)^{-1} & \text{for } \theta + \phi < \pi/2 \\[4mm] 2\,(2\beta + \tan\theta)\,(\beta + \sec\theta)^{-1} & \text{for } \theta + \phi = \pi/2 \end{cases}$$
$$(11)$$

The mean velocity is defined as

$$\overline{v^*} = \frac{2}{A_l^*} \int_0^{\beta + \tan\theta} \int_0^{z^*} v^* \, dz^* \, dx^* \qquad (12)$$

where the dimensionless cross-sectional area is given by

$$A_l^* = \begin{cases} \beta + (\beta + \tan\theta)(1 + d^*) - R^{*2}\cos^{-1}\left(\dfrac{d^*}{R^*}\right) & \text{for } \theta + \phi < \pi/2 \\[4mm] 2\beta + \tan\theta & \text{for } \theta + \phi = \pi/2 \end{cases} \qquad (13)$$

See Appendix A for derivations of the dimensionless Poisson equation, dimensionless boundary conditions, and dimensionless hydraulic diameter and area.

1.3   Numerical Model

The elliptic Poisson equation given in eqn. (3) with mixed boundary conditions [eqns. (4), (5) and (8)] was solved using Gauss-Seidel iteration with successive over-relaxation and a second-order central differencing scheme (Burden and Faires, 1985).

7

The symmetry boundary condition was modeled using a first-order forward difference, where the shear stress boundary condition employed a first-order backward difference. The convergence criteria for the iterative solution was set to $\epsilon = 10^{-8}$ for each case. A grid independence check was made in which the number of grids in each direction was doubled. When the value for the Poiseuille number did not change by more than 3%, grid independence was considered to be reached. The convergence criteria was then reduced by an order of magnitude while maintaining the highest number of grids. If the Poiseuille number did not change by more than 2%, the solution was considered to be independent of both grid size and ϵ. Otherwise, a grid independence check was made at the smaller value of ϵ until a converged solution was obtained. In fact, the grid independence for 423 of the 446 data points reported was less than 1% as documented in Appendix C.

The numerical model was tested against several existing solutions, such as rectangular ducts (Fig. 32 and Table 4), triangular grooves without interfacial shear stress (Fig. 33 and Table 5), and rectangular and triangular grooves with shear stress (Figs. 34 and 35 and Tables 6 and 7). See Appendix B for details.

Shah (1975) determined the friction factors for the laminar flow within ducts of various cross sections using a least-squares-matching technique. A comparison was made of the Poiseuille number between the present solution and those given by Shah (1975) and Shah and London (1978) for laminar flow in a family of rectangular ducts ($\theta = 0°$, $0.01 \leq \beta \leq 1.0$). The maximum difference was 0.9%.

Ayyaswamy et al. (1974) presented the friction factors obtained for laminar flow in triangular grooves using the Galerkin method of solution. Romero and Yost (1996) derived an equation for the dimensionless volumetric flow rate of liquid in a triangular groove using asymptotic methods and a regression analysis. Kolodziej et al. (1999) used the boundary collocation method to solve the same problem, except that the liquid-vapor interface was not assumed to be circular. The present solution was compared to that obtained by Ayyaswamy et al. for $\theta = 5°$ and $60°$ for the full range of meniscus contact angle ($0.1° \leq \phi \leq 90° - \theta$). The maximum percent differences for $\theta = 5°$ and $60°$ were 3.7% and 0.9%, respectively. In comparison to the results

8

by Romero and Yost (1996), the maximum percent differences were 2.2% for $\theta = 5°$ and 2.3% for $\theta = 60°$. The maximum differences in the comparison with the results provided by Kolodziej et al. for the lowest value of Bond number presented (Bo = 0.001) was 4.5% for $\theta = 5°$, and 19.9% for $\theta = 60°$. This may be due to the approximate nature of the solution by Kolodziej et al., which was in terms of a truncated infinite summation.

DiCola (1968) presented the solution for the Poiseuille number for the laminar flow of a constant property fluid within a rectangular groove. While interfacial shear stress at the liquid-vapor interface was accounted for, the groove was assumed to be completely full, with a meniscus contact angle of $\phi = 90°$. The comparison between the equation by DiCola and the results of the present analysis for laminar flow in a family of rectangular grooves at the full groove condition ($\phi = 90°$, $0.1 \leq \beta \leq 1.0$, $\tau_{lv}^* = -0.1, 0.0,$ and 1.0) resulted in a maximum percent difference of 2.3%.

The present model was compared to the correlation presented by Lin and Faghri (1997), where the friction factor for the flow of liquid in triangular grooves with liquid-vapor shear was presented. Unfortunately, not enough information was provided by Lin and Faghri to precisely determine the limits of applicability for their equation. Therefore, the correlation was evaluated over a fairly wide range for comparison with the present solution. In the range of $0.075 \leq -\tau_{lv}^* \leq 0.1$, the maximum percent difference was 2.2%.

1.4 Results and Discussion

1.4.1 Parametric Analysis

A numerical study has been completed in which the flow field in a trapezoidal groove has been solved. Specifically, values of the mean velocity, Poiseuille number, and volumetric flow rate are reported for various values of the groove aspect ratio, groove half-angle, meniscus contact angle, and dimensionless shear stress at the liquid-vapor interface (Tables 8-25). Figures 2 and 3 show contour plots of the dimensionless velocity obtained for two trapezoidal groove geometries. Figure 2 shows that the flow

9

behavior changes significantly with shear stress, even though the variation of τ_{lv}^* is relatively small for this case. The maximum velocity is located along the liquid-vapor interface for $\tau_{lv}^* = 0$ and 0.25, and within the interior of the flow field for $\tau_{lv}^* = -0.25$. For countercurrent flow [Fig. 2(c)], a region of reversed flow occurs near the intersection of the groove wall and the liquid-vapor interface. Figure 3 shows the velocity field in which the fluid depth is less than that in Fig. 2. In addition, the shear stress τ_{lv}^* varies over a wider range in Fig. 3. In contrast to Fig. 2, the maximum velocity does not occur at the centerline of the groove, but near the corner of the groove due to the greater depth at that location. The length of the groove wall that is affected by the reversed flow is greater in Fig. 3(c) due to the fact that the angle between the liquid-vapor interface and the groove wall is more acute than that in Fig. 2(c).

Figure 4 and Tables 8, 11, and 14 present the mean velocity versus shear stress at the liquid-vapor interface for several values of the groove half-angle. The range of the meniscus contact angle ($0 \le \phi \le 90° - \theta$) was divided equally to show the behavior of the mean velocity with ϕ. The mean velocity increases linearly with shear stress since the flow is aided by τ_{lv}^*. In addition, $\overline{v^*}$ increases with groove half-angle and meniscus contact angle, which is a result of an increase in cross-sectional area. As the groove half-angle θ increases, $\overline{v^*}$ becomes more sensitive to the meniscus contact angle ϕ due to the increased length of the perimeter of the liquid-vapor interface.

Figure 5 and Tables 9, 12, and 15 show that the Poiseuille number decreases dramatically as the shear stress at the liquid-vapor interface increases. For counter-current flow ($\tau_{lv}^* < 0$), the Poiseuille number is a strong function of shear stress since the mean velocity approaches zero. In addition, the Poiseuille number decreases with increasing meniscus contact angle for a given value of shear stress. For cocurrent flow ($\tau_{lv}^* > 0$), the Poiseuille number is a lesser function of the shear stress, but increases significantly with meniscus contact angle. The Poiseuille number is a weak function of the groove half-angle.

The volumetric flow rate versus shear stress for various meniscus contact angles can be seen in Fig. 6 and Tables 10, 13, and 16. The volumetric flow rate and mean
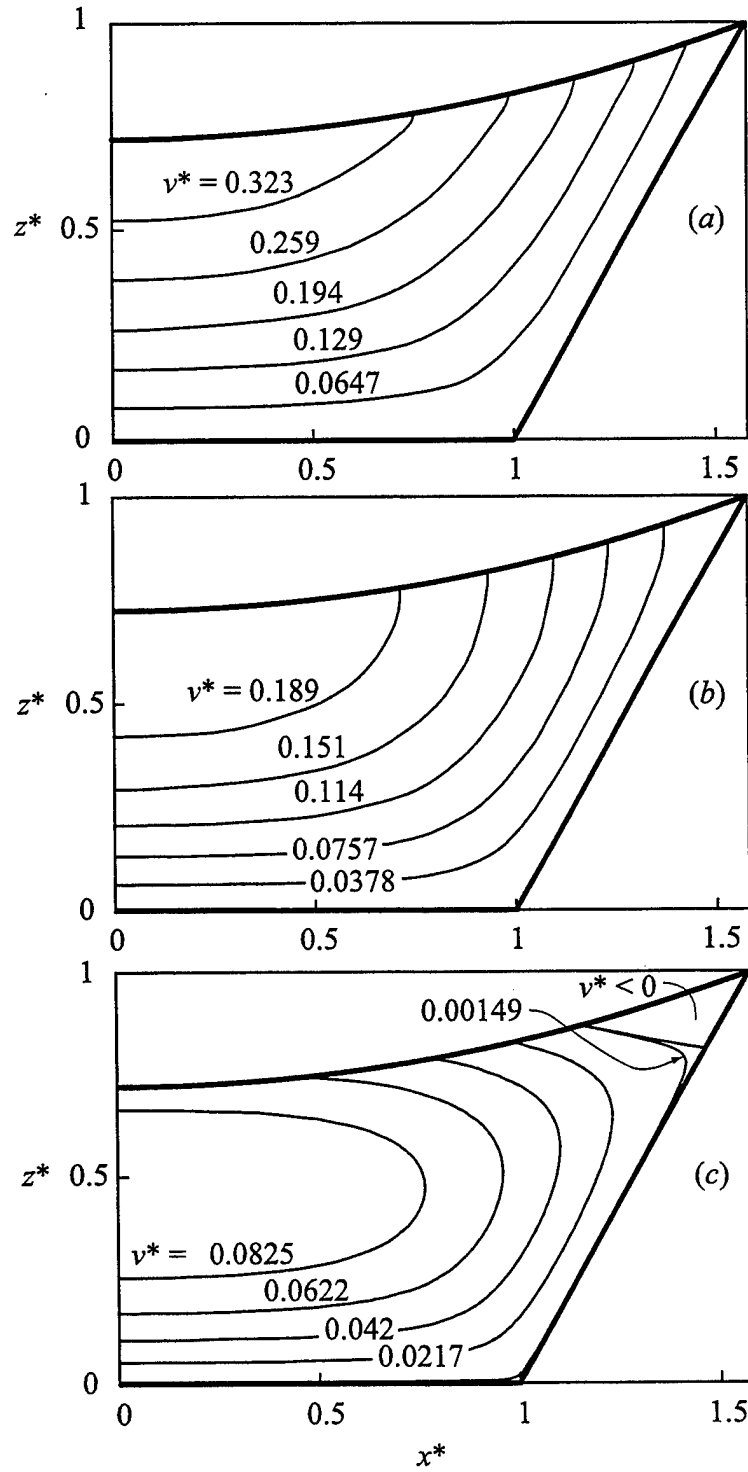
Figure 2: Dimensionless velocity fields for laminar flow in trapezoidal grooves ($\beta = 1.0$, $\phi = 40°$, $\theta = 30°$): (a) $\tau_{lv}^* = 0.25$ (cocurrent flow); (b) $\tau_{lv}^* = 0.0$; (c) $\tau_{lv}^* = -0.25$ (countercurrent flow).

11
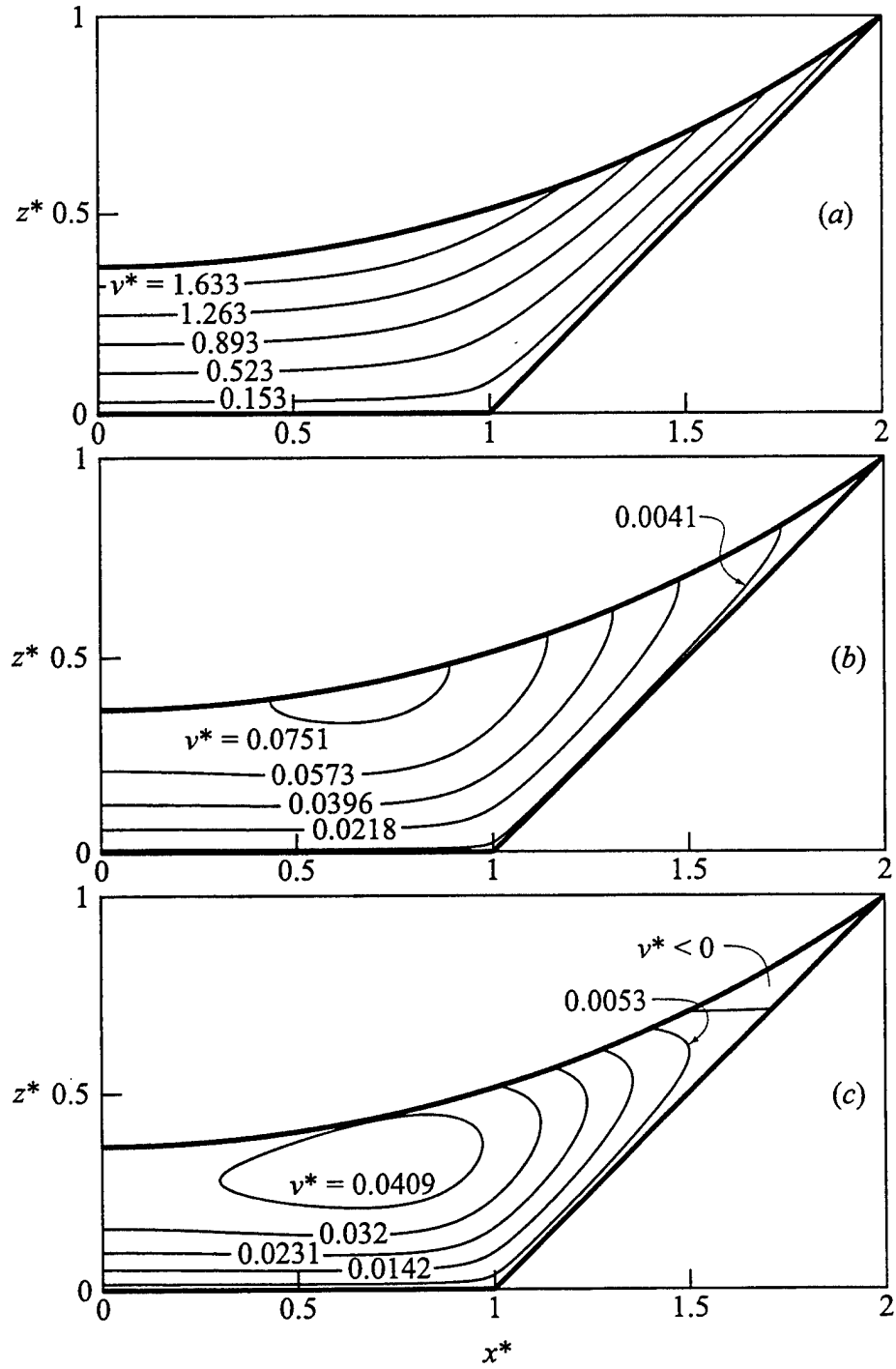
Figure 3: Dimensionless velocity fields for laminar flow in trapezoidal grooves ($\beta = 1.0$, $\phi = 10°$, $\theta = 45°$): (a) $\tau_{lv}^* = 5.0$ (cocurrent flow); (b) $\tau_{lv}^* = 0.0$; (c) $\tau_{lv}^* = -0.1$ (countercurrent flow).

velocity display similar trends. The volumetric flow rate is a linear function of shear stress, and increases with meniscus contact angle and groove half-angle. The flow rate is slightly more sensitive than the mean velocity with respect to the meniscus contact angle.

The mean velocity, Poiseuille number and volumetric flow rate are given as functions of the interfacial shear stress for a constant meniscus contact angle in Figs. 7, 8, and 9 and in Tables 17-25. For $\theta = 0$ and $30°$, the mean velocity increases and then decreases with groove aspect ratio. This point will be further elucidated in following figures. The Poiseuille number (Fig. 8) is a weak function of both θ and β for cocurrent flow, but varies significantly with β for countercurrent flow in rectangular grooves ($\theta = 0°$). The volumetric flow rate (Fig. 9) follows the same trends as the mean velocity, but is more heavily influenced by τ_{lv}^*, β, and θ.

Figure 10 and Table 28 present the mean velocity, Poiseuille number and volumetric flow rate for $\phi = 30°$ and $\tau_{lv}^* = 5.0$. As mentioned previously, the mean velocity increases and then decreases with β for $\theta \leq 30°$. This phenomenon also impacts the volumetric flow rate, where $\dot{V}^*$ attains a maximum value with respect to β for a given groove half-angle $\leq 15°$. Figure 11 and Table 29 show $\overline{v^*}$, Po, and $\dot{V}^*$ versus θ for $\beta = 1.0$ and $\tau_{lv}^* = 5.0$. In general, these functions increase with both meniscus contact angle and groove half-angle, except for the Poiseuille number for $\theta = 0°$ and $\phi \leq 20°$.

1.4.2 Semi-Analytical and Two-Point Numerical Solutions for $\overline{v^*}$

As seen in Figs. 4 and 7, the mean velocity is a linear function of the imposed shear stress at the liquid-vapor interface. Since a direct numerical simulation of the liquid flow field for a number of values of the shear stress is computer resource intensive, it is appropriate to seek a semi-analytical expression for $\overline{v^*}$. Figure 12(a) shows the definition of the parameters involved, where the mean velocity when the shear stress is zero ($\overline{v_0^*}$) is given by the numerical solution. The value for the liquid-vapor shear for which the mean velocity is zero ($\tau_{lv,0}^*$) is given by the following force balance analysis. Figure 12(b) shows a differential element of the liquid in the groove. A force balance between the pressure drop and the shear forces at the liquid-vapor interface and at

13
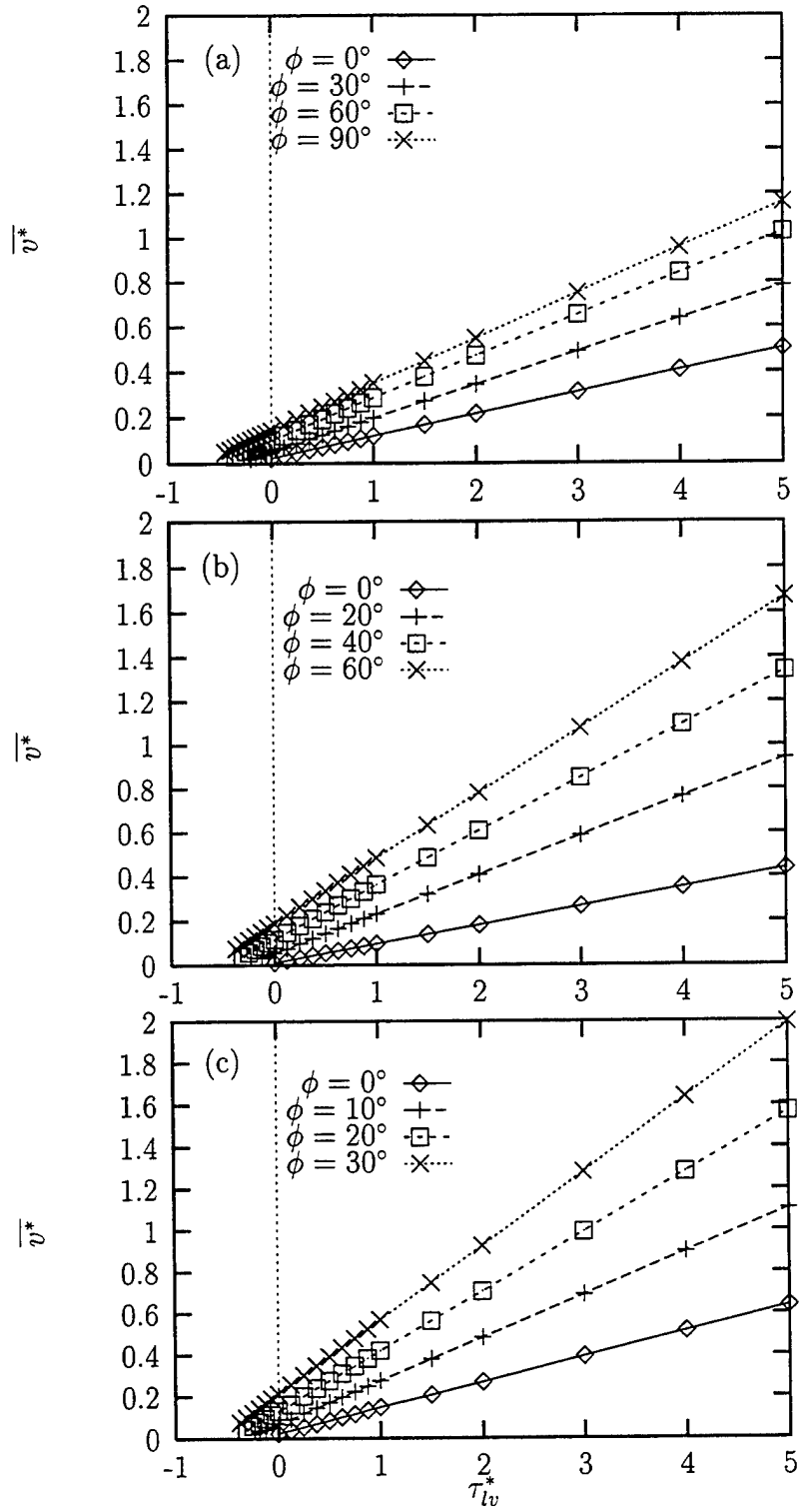
Figure 4: $\overline{v^*}$ versus τ_{lv}^* for laminar flow in trapezoidal grooves ($\beta = 1.0$): (a) $\theta = 0°$; (b) $\theta = 30°$; (c) $\theta = 60°$.
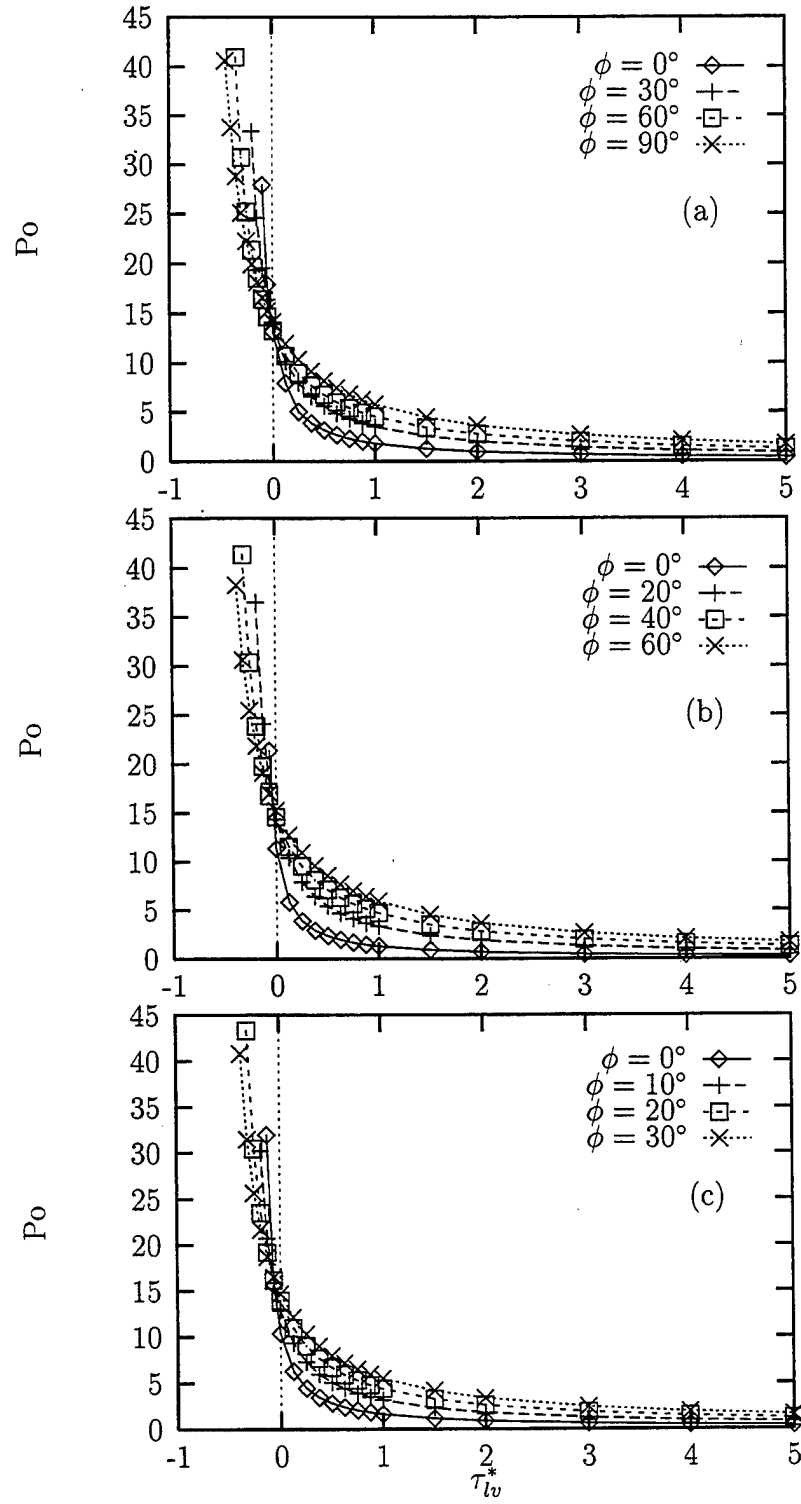
Figure 5: Po versus τ_{lv}^* for laminar flow in trapezoidal grooves ($\beta = 1.0$): (a) $\theta = 0°$; (b) $\theta = 30°$; (c) $\theta = 60°$.
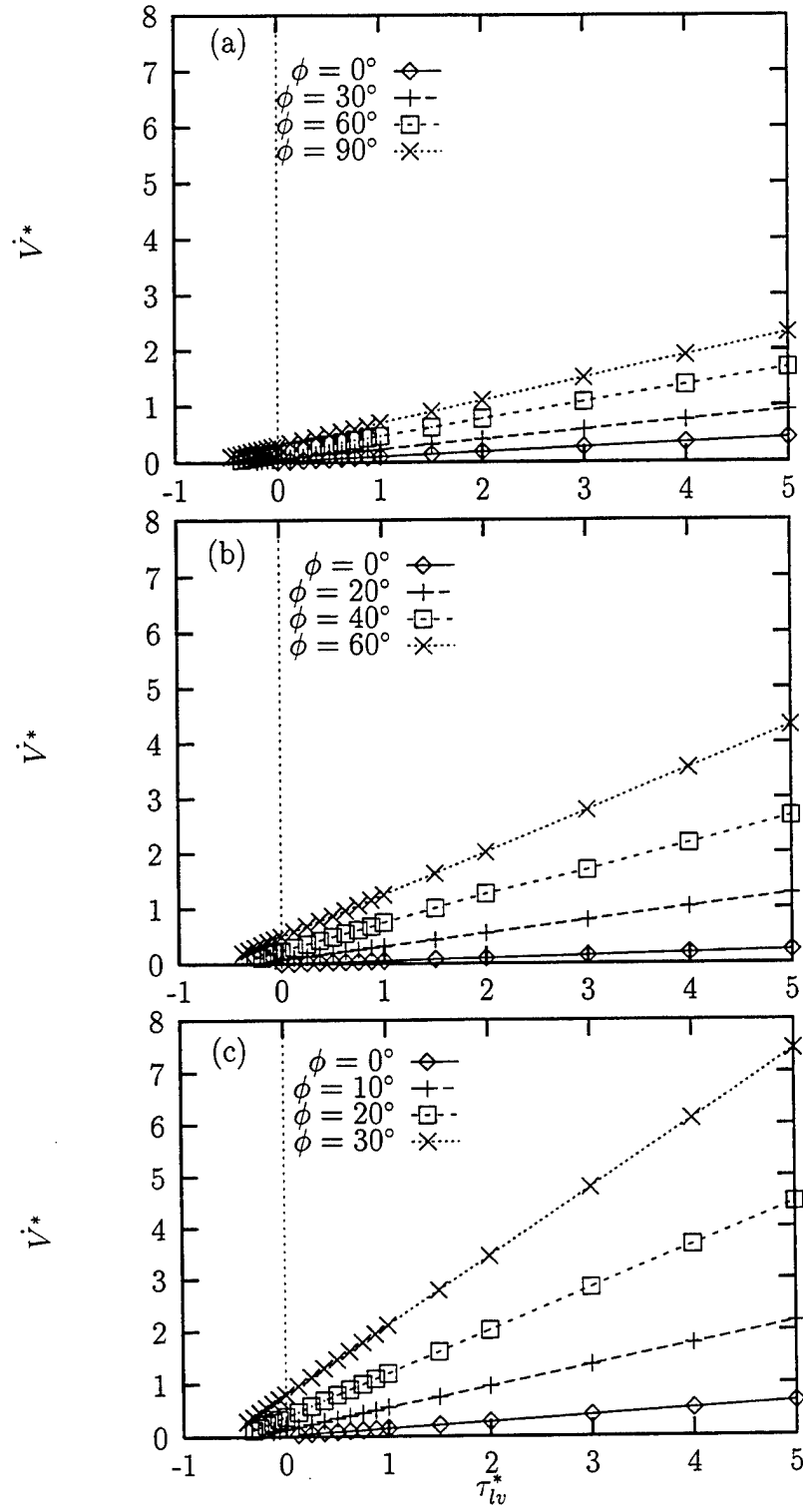
Figure 6: $\dot{V}^*$ versus τ_{lv}^* for laminar flow in trapezoidal grooves ($\beta = 1.0$): (a) $\theta = 0°$; (b) $\theta = 30°$; (c) $\theta = 60°$.
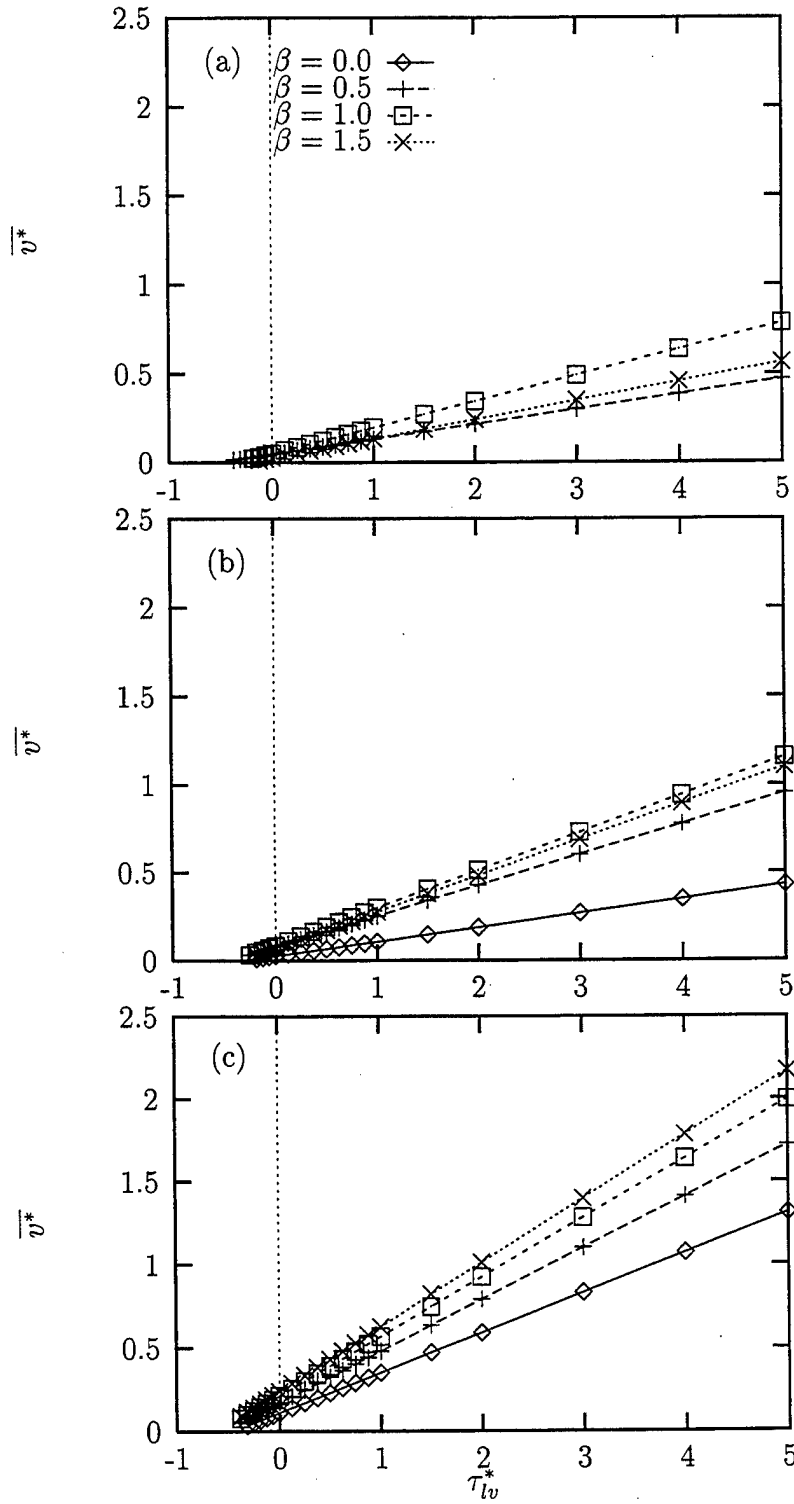
Figure 7: $\overline{v^*}$ versus τ_{lv}^* for laminar flow in trapezoidal grooves ($\phi = 30°$): (a) $\theta = 0°$; (b) $\theta = 30°$; (c) $\theta = 60°$.
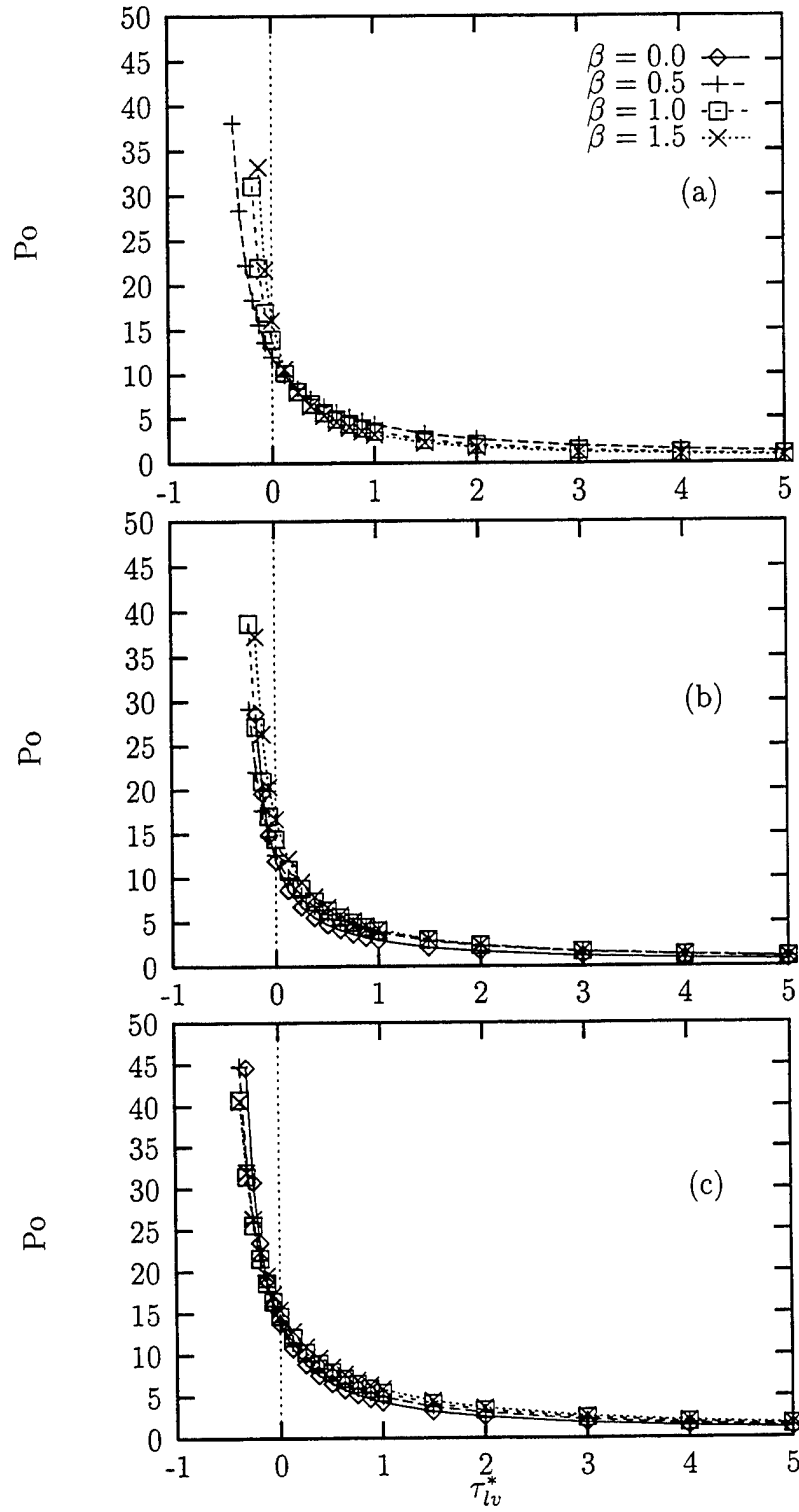
17

Figure 8: Po versus τ_{lv}^* for laminar flow in trapezoidal grooves ($\phi = 30°$): (a) $\theta = 0°$; (b) $\theta = 30°$; (c) $\theta = 60°$.

18

Figure 9: $\dot{V}^*$ versus τ_{lv}^* for laminar flow in trapezoidal grooves ($\phi = 30°$): (a) $\theta = 0°$; (b) $\theta = 30°$; (c) $\theta = 60°$.

19
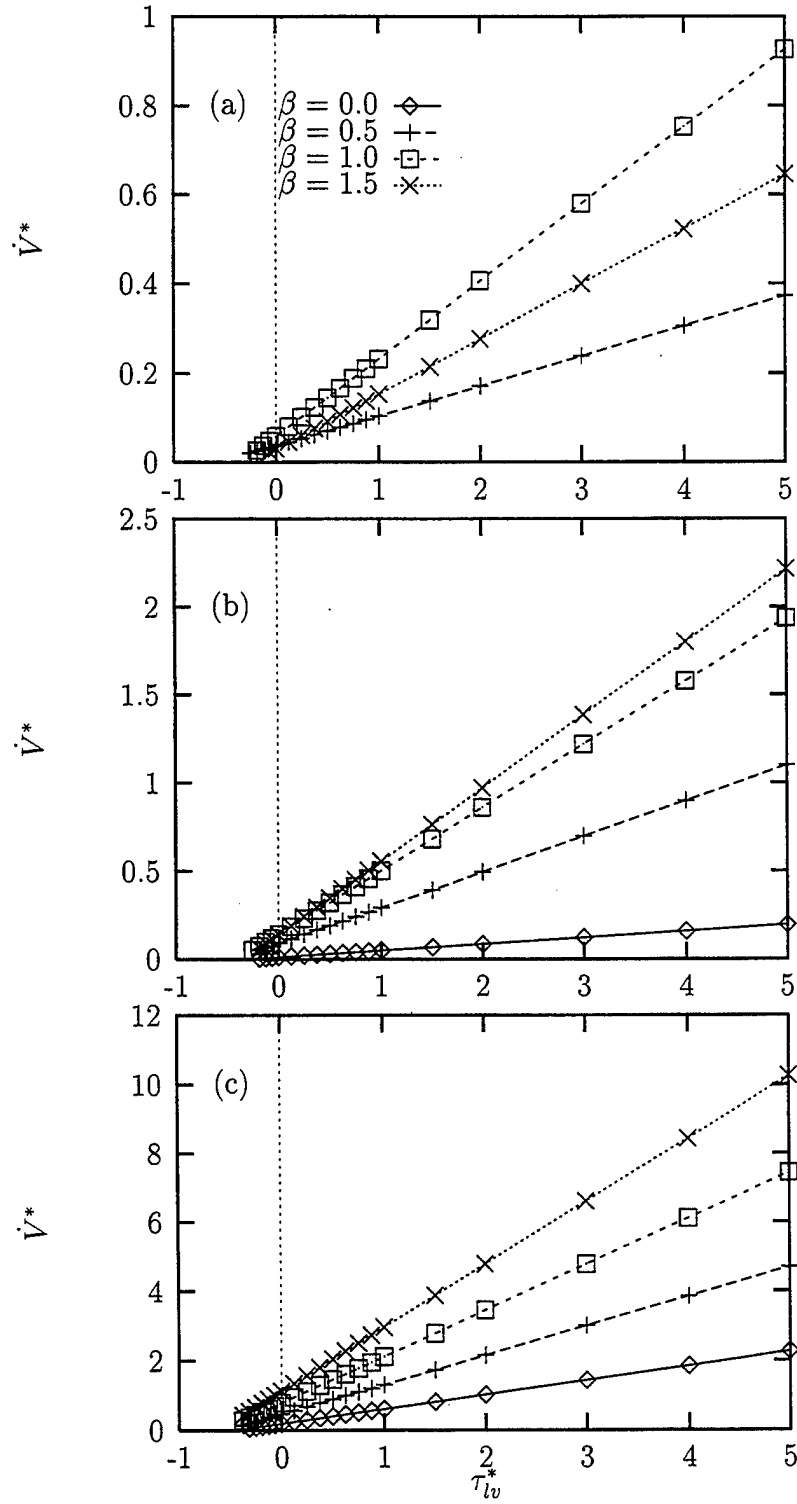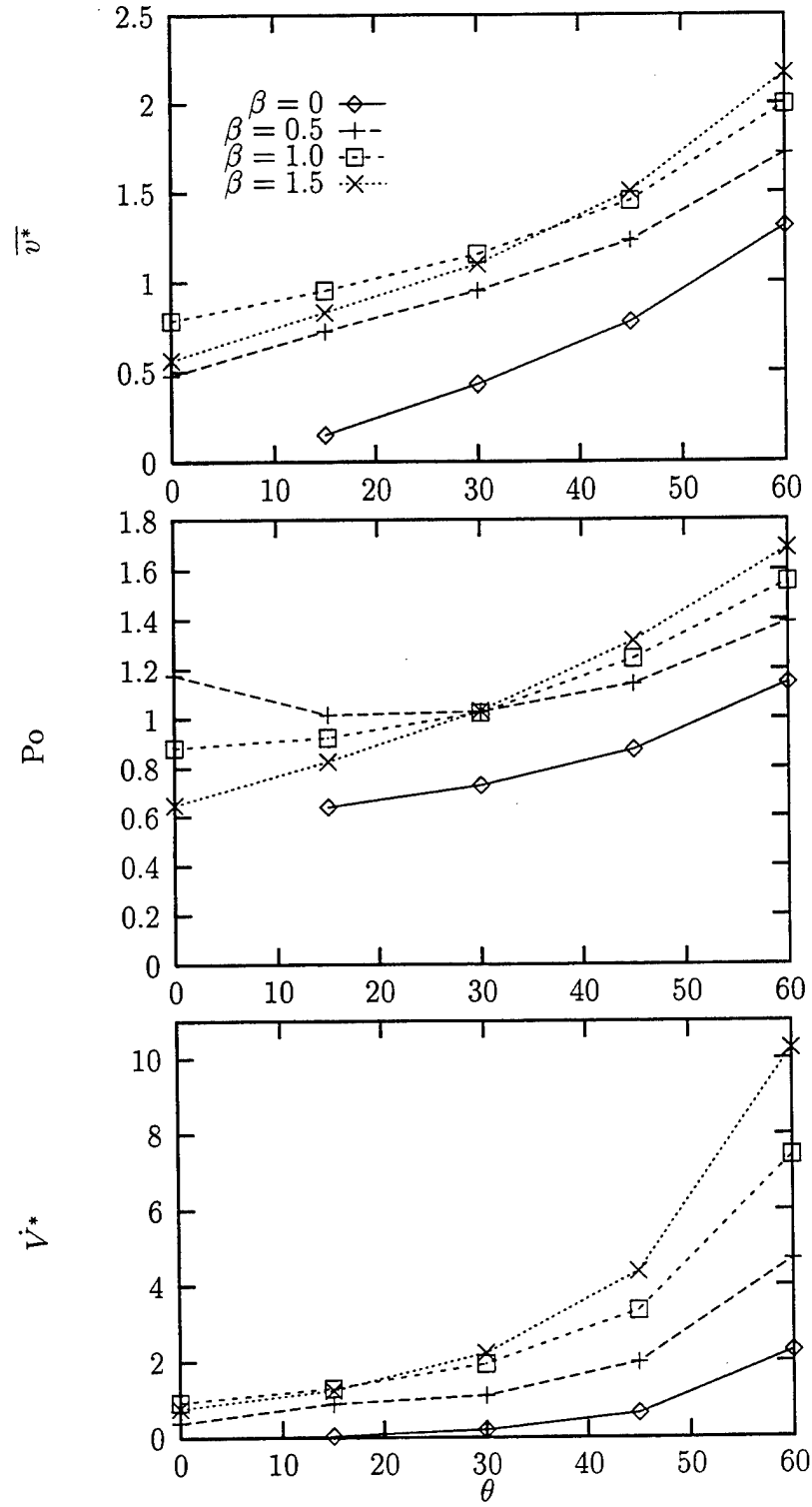
Figure 10: $\overline{v^*}$, Po and $\dot{V}^*$ versus θ for laminar flow in trapezoidal grooves ($\phi = 30°$, $\tau_{lv}^* = 5.0$).
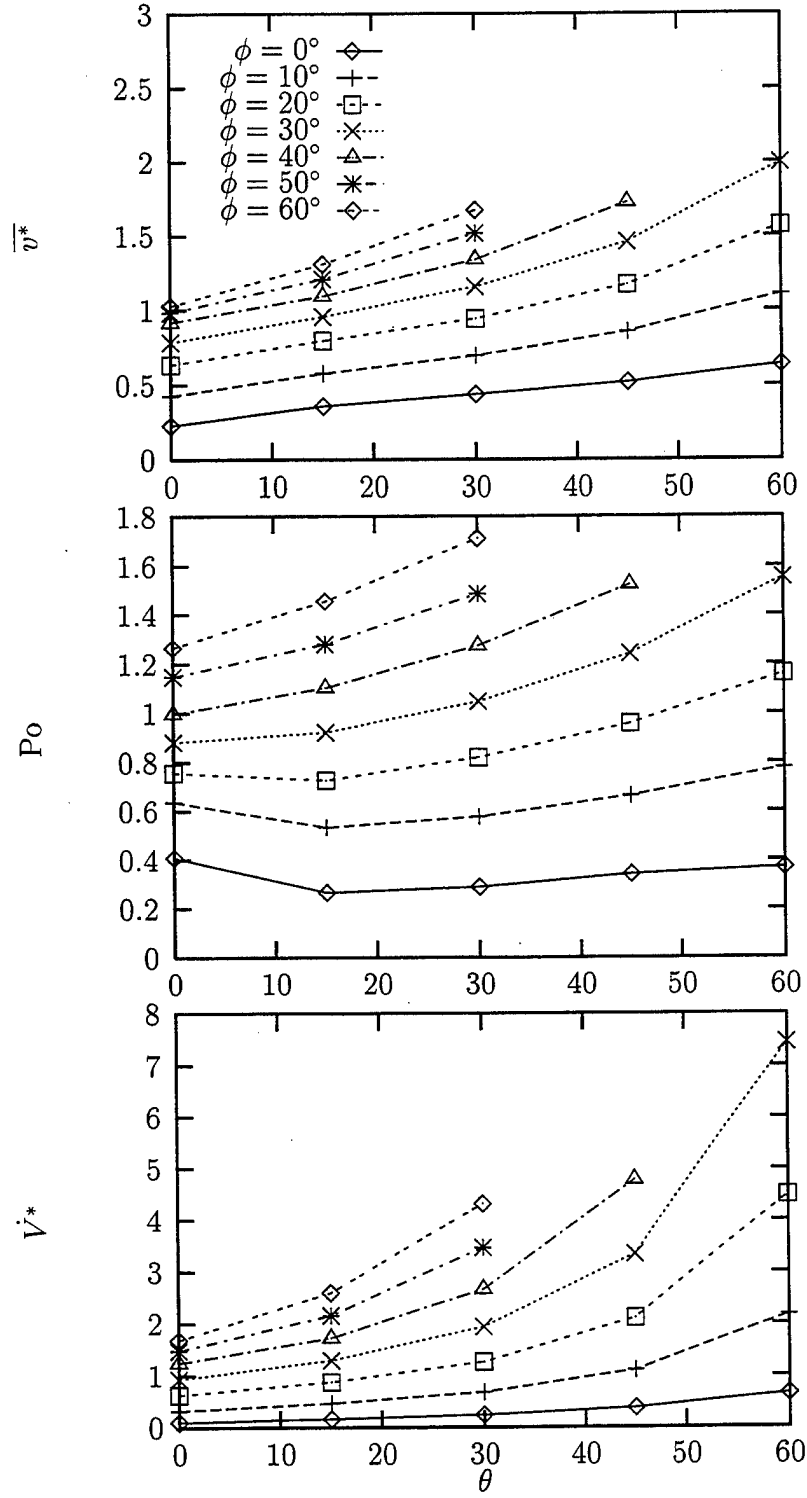
Figure 11: $\overline{v^*}$, Po and $\dot{V}^*$ versus θ for laminar flow in trapezoidal grooves ($\beta = 1.0$, $\tau_{lv}^* = 5.0$).

the wall results in the following relation.

$$p_y A_l - p_{y+dy} A_l + \tau_{lv} A_{lv} - \overline{\tau_w} A_w = 0 \tag{14}$$

The areas over which the shear stresses τ_{lv} and $\overline{\tau_w}$ act are $A_{lv} = P_{lv} dy$ and $A_w = P dy$, respectively. Using these areas and nondimensionalizing gives

$$A_l^* + \tau_{lv}^* P_{lv}^* - \overline{\tau_w^*} P^* = 0 \tag{15}$$

For Poiseuille flow in ducts of arbitrary cross section, and combined Couette-Poiseuille flow between flat plates, the shear stress at the wall is related to the mean velocity of the fluid by a constant (White, 1991). In the present analysis, it is assumed that this also holds for the flow of liquid in a trapezoidal groove with an imposed shear stress at the liquid-vapor interface.

$$\overline{\tau_w^*} = C_1 \overline{v^*} \tag{16}$$

It should be noted that the constant C_1 is probably a function of the groove geometry and meniscus contact angle. However, since the objective of this analysis is to determine the liquid-vapor shear stress when the mean liquid velocity is zero, this functionality is unimportant.

Substituting this relation into the force balance equation results in the following expression for mean velocity

$$\overline{v^*} = \frac{1}{C_1 P^*} \left(A_l^* + \tau_{lv}^* P_{lv}^* \right) \tag{17}$$

where the perimeter of the liquid-vapor interface is

$$P_{lv}^* = \begin{cases} 2R^* \sin^{-1} \left(\dfrac{\beta + \tan\theta}{R^*} \right) & \text{for } \theta + \phi < \pi/2 \\[3mm] 2(\beta + \tan\theta) & \text{for } \theta + \phi = \pi/2 \end{cases} \tag{18}$$

The mean velocity is zero when the shear stress at the liquid-vapor interface is

$$\tau_{lv,0}^* = -\frac{A_l^*}{P_{lv}^*} \tag{19}$$

22
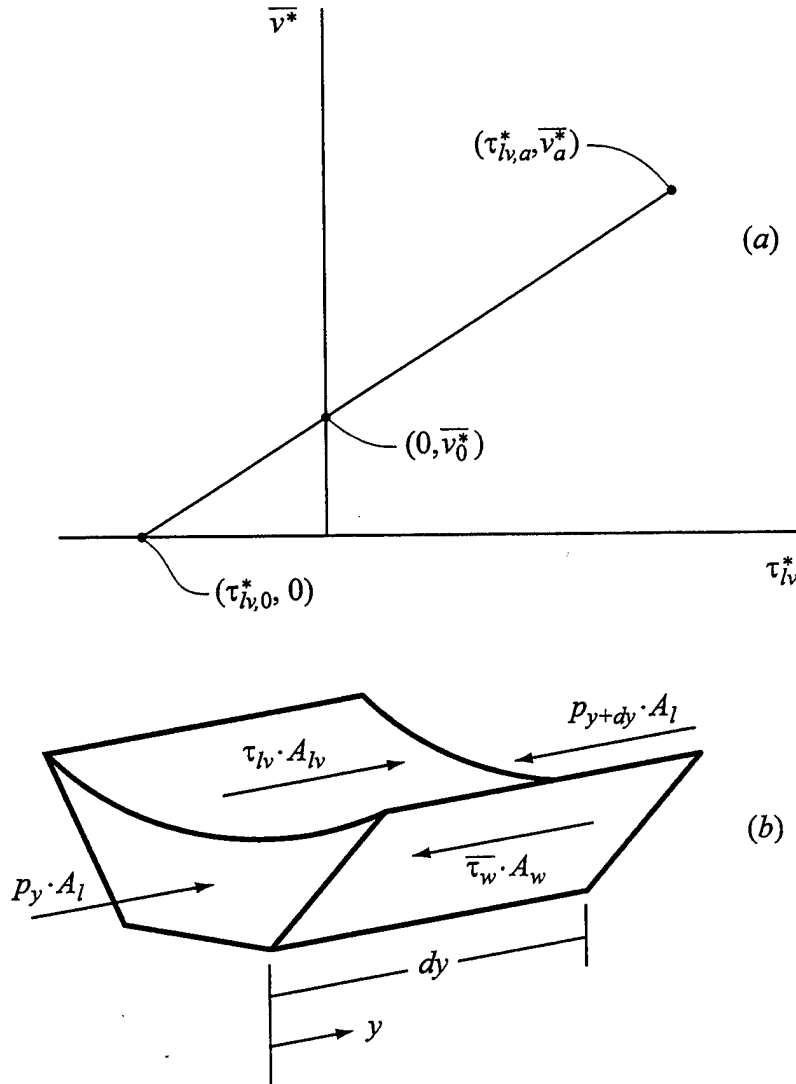
Figure 12: Semi-analytical and two-point numerical solutions for $\overline{v}^*$: (a) Definition of parameters; (b) Force balance on the liquid in a trapezoidal groove.

Figures 13(a) and 13(b) show the results of eqn. (19). The numerical results shown in Figs. 4 and 7 were extrapolated to determine the values for shear stress at the liquid-vapor interface when $\overline{v^*} = 0$. The prediction given by eqn. (19) is quite good given the simplicity of the closed-form solution. The equation for the normalized mean velocity as a function of the shear stress is given by

$$v' = \overline{v^*}/\overline{v_0^*} = 1 - \tau'\tag{20}$$

where $\tau' = \tau_{lv}^*/\tau_{lv,0}^*$. The semi-analytical solution for the normalized mean velocity is shown in Fig. 13(c) with the corresponding numerical data presented in Figs. 4 and 7. Equation (20) predicts 93% of the data to within $\pm 30\%$ over the range of the meniscus contact angle, groove half-angle, groove aspect ratio and liquid-vapor shear stress examined in Figs. 4 and 7.

The two-point numerical solution of $\overline{v^*}$ as a function of τ_{lv}^* is also shown in Fig. 12(a). This involves computing the flow field for two values of liquid-vapor shear stress. The equation for the normalized mean velocity using this solution is given by eqn. (20), but the shear stress when the mean velocity is zero is

$$\tau_{lv,0}^* = \frac{\tau_{lv,a}^*}{\left(1 - \overline{v_a^*}/\overline{v_0^*}\right)}\tag{21}$$

1.4.3 Regression Analysis

A linear regression analysis was performed to determine the mean velocity as a function of the groove geometry, meniscus contact angle, and shear stress at the liquid-vapor interface. Equation (22) and Table 1 show the results of this analysis. The regression was found by determining the relationships between the mean velocity and each of the groove aspect ratio, groove half angle, meniscus contact angle, and interfacial shear stress separately, then summing these relations to arrive at the model
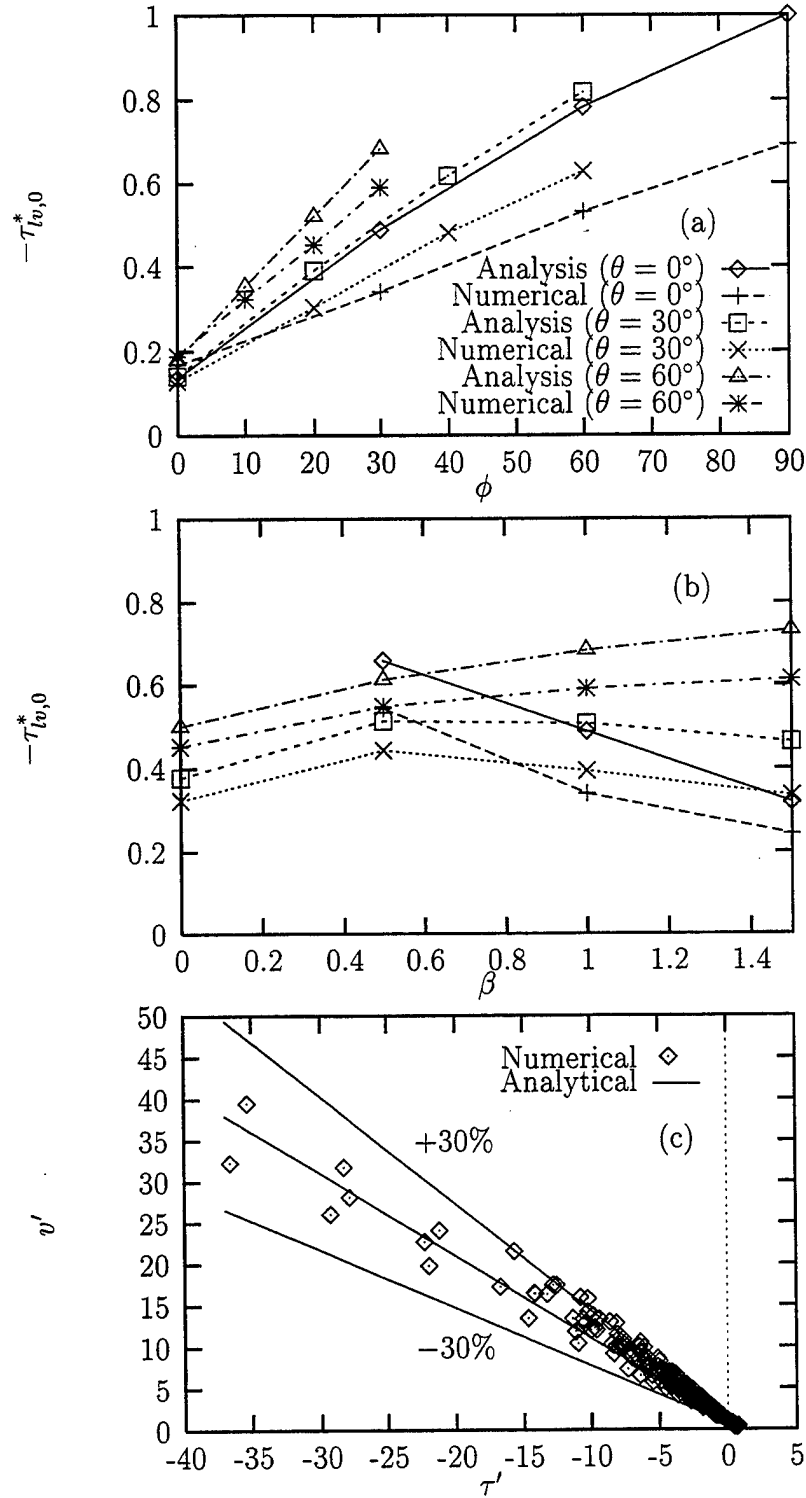
Figure 13: Numerical and semi-analytical solution comparison: (a) $-\tau_{lv,0}^*$ versus ϕ for $\beta = 1.0$ (from Fig. 4); (b) $-\tau_{lv,0}^*$ versus β for $\phi = 30°$ (from Fig. 7); (c) Normalized mean velocity versus normalized shear stress at the liquid-vapor interface (from Figs. 4 and 7).
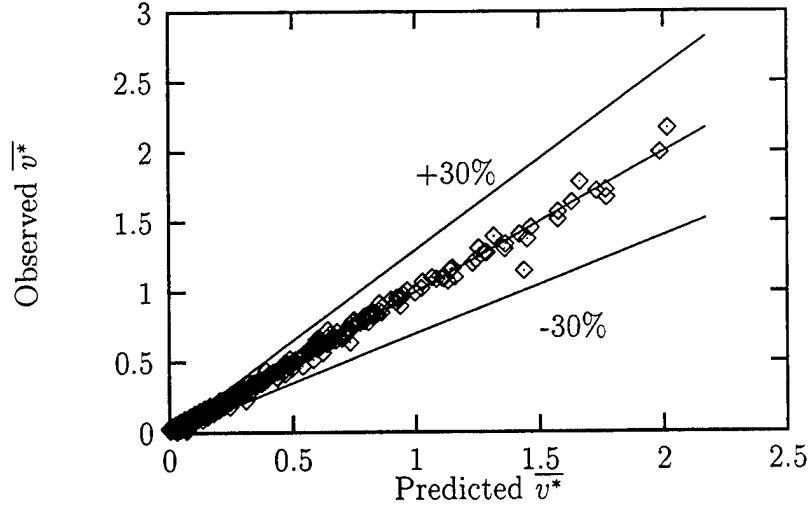
Figure 14: Comparison of data with regression.

shown in eqn. (22).

$$\overline{v^*} = a\theta^3 + b\theta^2 + c\theta^2\beta + d\theta^2\phi + e\theta^2\tau_{lv}^* + f\theta\phi + g\theta + h\phi^3 + i\phi^2\theta + j\phi^2\tau_{lv}^* +$$

$$k\phi\tau_{lv}^* + l\phi\theta\tau_{lv}^* + m\phi + n\beta^2 + o\beta^2\theta + p\beta^2\tau_{lv}^* + q\beta\theta + r\beta\tau_{lv}^* + \qquad (22)$$

$$s\beta\theta\phi + t\beta\theta\tau_{lv}^* + u\beta\phi\tau_{lv}^* + v\beta + w\tau_{lv}^* + x\beta\theta\phi\tau_{lv}^* + y$$

A statistical software package SPSS (Statistical Package for the Social Sciences) was utilized to perform the regression analysis, and the outcome for the coefficients is shown in Table 1. A comparison of the observed mean velocity versus the predicted mean velocity is presented in Fig. 14. The regression predicts 85.0% of the observed data presented in Figs. 4, 7, 10(a), and 11(a) to within $\pm 30\%$.

1.4.4 Effect of Groove Fill Ratio

Figure 15(a) shows the case when liquid evaporates from a trapezoidal groove. Initially, the groove is full with $\phi + \theta = 90°$. The contact angle decreases until the minimum meniscus contact angle ϕ_0 for the particular solid-liquid combination is reached. Past this point, the meniscus detaches from the top of the groove and recedes until the lowest part of the meniscus reaches the bottom of the groove (Hopkins et al., 1999). When the thickness of the liquid film at the bottom of the groove is

26

Table 1: Coefficients for regression analysis.

Coefficient	Value	Coefficient	Value
a	4.045E-6	m	2.492E-3
b	-4.747E-4	n	-0.1780
c	5.656E-5	o	3.186E-3
d	3.540E-6	p	-9.241E-2
e	3.970E-5	q	-1.031E-2
f	-2.299E-4	r	7.430E-2
g	1.767E-2	s	8.072E-5
h	-9.312E-8	t	-9.775E-4
i	7.011E-7	u	4.309E-3
j	-1.495E-5	v	0.3420
k	-1.460E-3	w	8.266E-2
l	3.194E-5	x	4.224E-5
		y	-0.1780

on the order of several hundred Angstroms, forces due to London-van der Waals interactions with the surrounding liquid and solid molecules induce instabilities in the fluid (Ruckenstein and Jain, 1974). These instabilities cause the liquid in the groove to bifurcate into two separate flows in the corners of the groove, which are each equivalent to the flow in a triangular groove. The liquid in the two corners of the groove will continue to recede until it is depleted.

The dimensions of the grooves analyzed by Castle et al. (2000) were used to determine the volumetric flow rate of ethanol in a trapezoidal copper groove as a function of the amount of liquid in the groove. Faghri (1995) gives $\phi_0 = 7°$ for a receding meniscus of ethanol on copper. In terms of the present analysis, as the liquid recedes into the groove, the groove aspect ratio β increases. In addition, after bifurcation occurs $\beta = 0$, and the groove half-angle θ changes to that of the corner of the groove. A relation for the point at which bifurcation occurs is provided where the liquid is assumed to bifurcate when the lowest part of the meniscus actually reaches the bottom of the groove. The radius of curvature at the bifurcation point for the trapezoidal groove is

$$R_b^* = \frac{1}{2}\left[1 + (\beta + \tan\theta)^2\right] \tag{23}$$
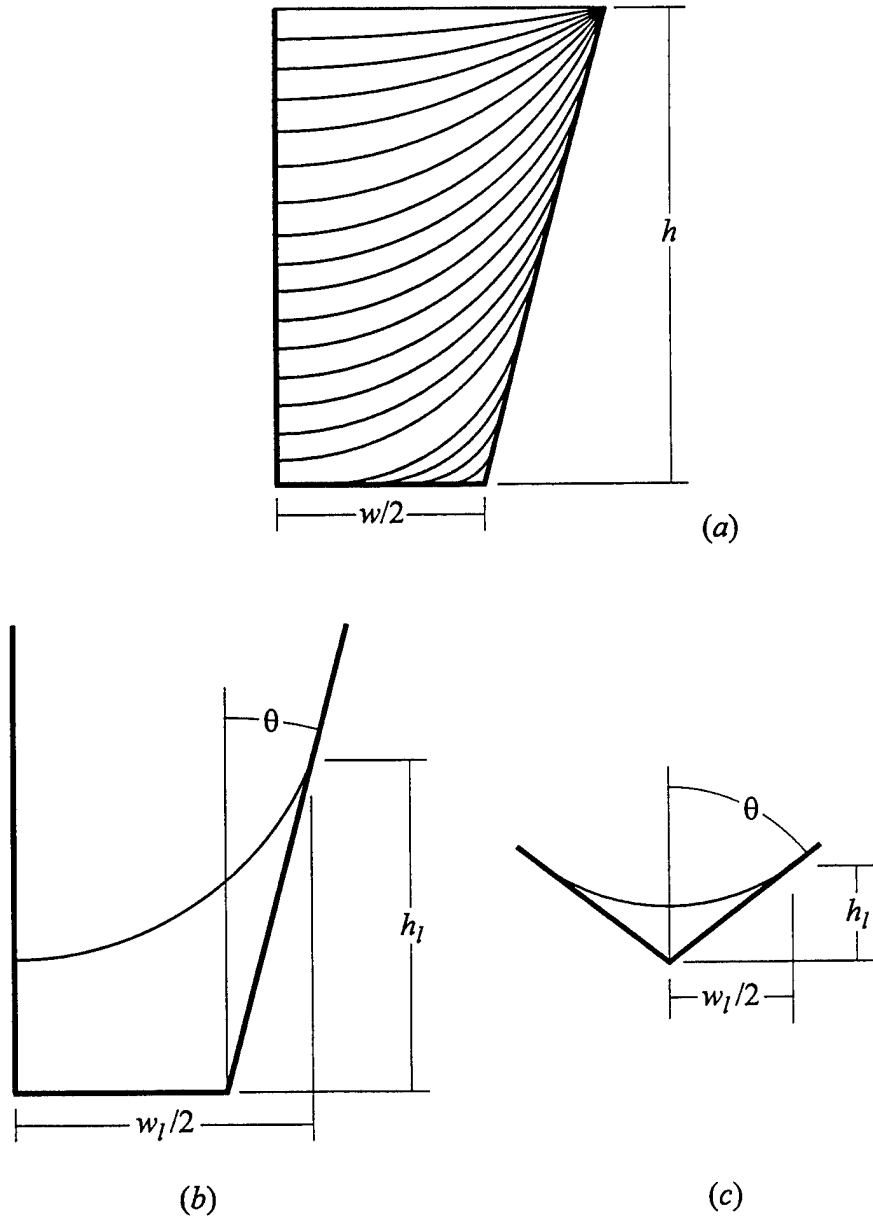
Figure 15: Effect of groove fill ratio on liquid flowing in a trapezoidal groove: (a) Parametric analysis (to scale, $h = 0.03831$ cm, $w = 0.03445$ cm, $\theta = 14.62°$); (b) Definition of variables prior to bifurcation of the liquid; (c) Definition of variables after bifurcation of the liquid.
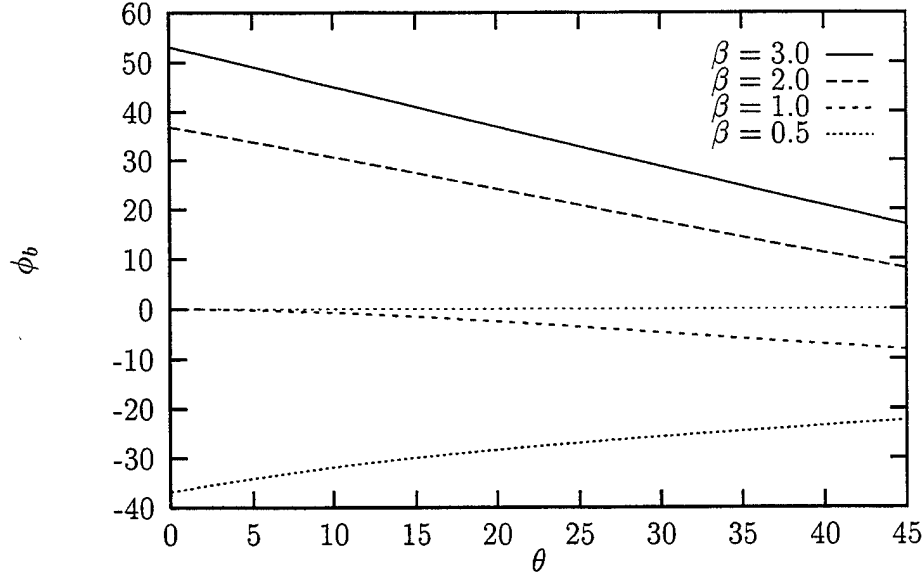
Figure 16: Meniscus contact angle (in arc degrees) at bifurcation versus θ for various values of β.

The meniscus contact angle at bifurcation as a function of the groove geometry is

$$\phi_b = \tan^{-1}\left(\frac{1}{\sin\theta}\left\{\left[\cos\theta + \frac{2\sin\theta\,(\beta+\tan\theta)}{1-(\beta+\tan\theta)^2}\right]^{-1} - \cos\theta\right\}\right)^{-1}$$

$$= \tan^{-1}\left[\frac{(3\beta^2-4)\cos\theta + \beta^2\cos 3\theta}{8\beta\cos\theta + (\beta^2+4)\sin\theta + \beta^2\sin 3\theta}\right] \tag{24}$$

This function is shown in Fig. 16 for various values of β. For $\beta < 1$ (slender grooves), the contact angle is negative for all values of θ, which indicates that the lowest part of the meniscus cannot reach the groove bottom and still maintain a circular shape. For $\beta = 1$, the only value of ϕ_b for which the meniscus will reach the groove bottom is $\theta = 0$. If the groove aspect ratio is $\beta > 1$, the meniscus can reach the groove bottom over a range of θ values.

The dimensional height and width of the liquid before and after bifurcation are defined in Figs. 15(b) and 15(c). For a given liquid height, the width of the liquid is

$$w_l = \begin{cases} w + 2h_l\tan\theta & \text{before bifurcation} \\ 2h_l\tan\theta & \text{after bifurcation} \end{cases} \tag{25}$$

The radius of curvature of the liquid-vapor interface and the cross-sectional area of

the liquid are

$$
R = \begin{cases} \dfrac{w_l}{2} \sqrt{1 + \left\{ \cot\theta - \left[\dfrac{\sin\phi}{\sin\theta\sin(\theta+\phi)} \right] \right\}^{-2}} & \text{before bifurcation} \\[3em] h_l \tan\theta \sqrt{1 + \left\{ \cot\theta - \left[\dfrac{\sin\phi}{\sin\theta\sin(\theta+\phi)} \right] \right\}^{-2}} & \text{after bifurcation} \end{cases} \tag{26}
$$

$$
A_l = \begin{cases} \dfrac{h_l}{2}(w+w_l) - R^2 \cos^{-1} \sqrt{1 - \left(\dfrac{w_l}{2R}\right)^2} + \dfrac{Rw_l}{2}\sqrt{1 - \left(\dfrac{w_l}{2R}\right)^2} \\[1em] \hspace{6cm} \text{before bifurcation} \\[2em] 2\left[h_l^2 \tan\theta - R^2 \cos^{-1}\sqrt{1 - \left(\dfrac{h_l\tan\theta}{R}\right)^2} + h_l R \tan\theta \sqrt{1 - \left(\dfrac{h_l\tan\theta}{R}\right)^2} \right] \\[1em] \hspace{6cm} \text{after bifurcation} \end{cases} \tag{27}
$$

The cross-sectional area of the groove is

$$
A_g = h\left(w + h\tan\theta\right) \tag{28}
$$

Table 30 gives the geometric values of the parametric analysis depicted in Fig. 15(a).

The radius of curvature of the liquid-vapor interface is shown in Fig. 17(a) as a function of the groove fill ratio. When the groove is nearly full, the radius of curvature approaches infinity. As the amount of liquid in the groove decreases, the radius of curvature is relatively constant, and then becomes very small after the liquid bifurcates into the corners of the groove. Figures 17(b) and 17(c) and Table 31 show two flow parameters, which were defined as follows.

$$
F_1 = \frac{\mu\bar{v}}{(-dp/dy)} \tag{29}
$$

$$
F_2 = \frac{\mu\dot{V}}{(-dp/dy)} \tag{30}
$$

These parameters allow the presentation of the mean velocity and volumetric flow rate before and after bifurcation on the same graph. Both flow parameters increase

monotonically with groove fill ratio, as expected. In Fig. 17(c), for a groove fill ratio of $A_l/A_g = 0.158$, the volumetric flow rate was 1% of that for the full groove due to the decrease in flow area. This figure shows that the groove was essentially shut off for $A_l/A_g \leq 0.158$, which was just prior to bifurcation. Using the functional relationship for mean velocity given by eqn. (17), the volumetric flow rate is

$$\dot{V}^* = \frac{A_l^*}{C_1 P^*} \left(A_l^* + \tau_{lv}^* P_{lv}^* \right) \tag{31}$$

When $\tau_{lv}^* = 0$, $\dot{V} \propto A_l^2$, which confirms that the volumetric flow rate should decrease rapidly with decreasing flow area for $A_l < 1$.

1.4.5 Capillary Limit Analysis for a Revolving Helically-Grooved Heat Pipe

Using the results of the numerical analysis, the capillary limit prediction for a revolving helically-grooved heat pipe proposed by Thomas et al. (1998) was improved by accounting for the effects of working fluid fill amount and the shear stress at the liquid-vapor interface. The improved model was compared to the experimental data collected by Castle et al. (2000), who determined the capillary limit of a revolving helically-grooved copper-ethanol heat pipe for radial accelerations of $|\vec{a_r}| = 0.01$, 2.0, 4.0, 6.0, 8.0 and 10.0-g and groove fill ratios of $V_l/V_g = 0.5$, 1.0 and 1.5. The liquid inventory volume and the total groove volume are given by V_l and V_g, respectively. The dimensions of the heat pipe examined by Castle et al. (2000) are given in Table 2. A pressure balance within the heat pipe results in the following expression for the capillary limit (Faghri, 1995; Chi, 1976)

$$\Delta p_{\text{cap,max}} \geq \Delta p_v + \Delta p_l + \Delta p_{\text{bf}} \tag{32}$$

The maximum capillary pressure for an axial groove is

$$\Delta p_{\text{cap,max}} = \frac{\sigma}{R_c} \tag{33}$$

It is assumed that the capillary limit occurs when the liquid bifurcates into the corners of the grooves. This statement is based on the results of the variation of the volumetric

31
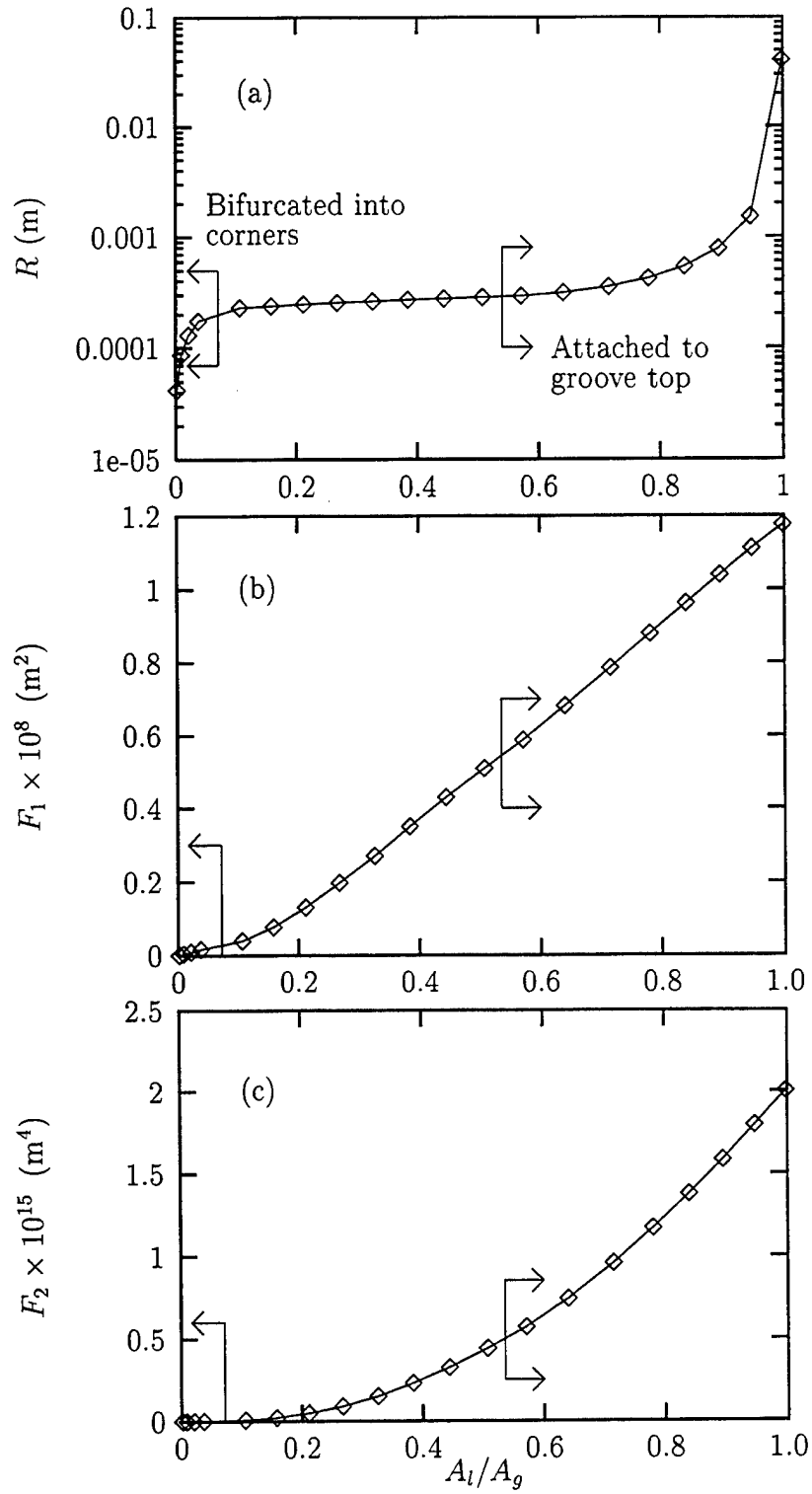
Figure 17: Effect of groove fill ratio: (a) Radius of curvature of the liquid-vapor interface; (b) Mean velocity parameter; (c) Volumetric flow rate parameter.

Table 2: Specifications of the heat pipe test article examined by Castle et al. (2000).

Groove Height, h	0.03831 cm
Groove Base Width, w	0.03445 cm
Groove Half-Angle, θ	14.62°
Evaporator Length, L_e	15.2 cm
Adiabatic Length, L_a	8.2 cm
Condenser Length, L_c	15.2 cm
Vapor Space Radius, R_v	0.6795 cm
Number of Grooves, N_g	50
Helical Pitch Length, L_p	135.8 cm
Helix Radius, R_h	0.6992 cm

flow rate with groove fill ratio in Fig. 17. The capillary radius when the liquid bifurcates is given by eqn. (23).

$$R_c = \frac{h}{2} \left[1 + (\beta + \tan \theta)^2 \right] \tag{34}$$

The meniscus contact angle at bifurcation is a function of the groove geometry, as presented in eqn. (24). These two equations were solved to determine the capillary radius at the point of dryout in the following manner. The groove aspect ratio was calculated using the groove height and width found in Table 2 ($\beta = 0.4496$). This value of β indicates that the meniscus must recede into the groove before the bifurcation point can be reached (Fig. 16). Therefore, eqn. (24) was solved iteratively to determine the aspect ratio for which the meniscus contact angle was equal to the minimum meniscus contact angle for the copper-ethanol system. The resulting aspect ratio was $\beta = 1.2112$. Solving for the height of the meniscus in the groove results in $h = h_l = 0.01422$ cm. Substituting this value into eqn. (34) for the meniscus radius of curvature gives $R_c = 0.02252$ cm.

For a circular cross section heat pipe assuming laminar, incompressible flow with uniform heat input and output along the lengths of the evaporator and condenser, respectively, the pressure drop in the vapor is

$$\Delta p_v = \frac{8 \mu_v L_{\text{eff}} \dot{Q}_t}{\pi \rho_v h_{\text{fg}} R_v^4} \tag{35}$$

33

The pressure drop in the liquid was found by using the normalized mean velocity relation [eqn. (20)] rewritten in dimensional form.

$$dp_l = -\left(\frac{\mu_l \overline{v_l}}{h_l^2 \overline{v_0^*}} + \frac{\tau_{lv}}{h_l \tau_{lv,0}^*} \right) dy \qquad (36)$$

In a heat pipe, the liquid flows opposite to the vapor in all regions. Therefore, the shear stress at the liquid-vapor interface for countercurrent flow was used.

$$\tau_{lv} = -\left[\frac{\rho_v \left(\overline{v_v} \right)^2}{2} \right] f_v \qquad (37)$$

The Poiseuille number of the vapor flow was modeled as laminar flow within a smooth tube with a circular cross section

$$\mathrm{Po}_v = f_v \mathrm{Re}_v = 16 \qquad (38)$$

Substituting these relations into eqn. (36) gives

$$dp_l = -\left(\frac{\mu_l \overline{v_l}}{h_l^2 \overline{v_0^*}} - \frac{4\mu_v \overline{v_v}}{h_l R_v \tau_{lv,0}^*} \right) dy \qquad (39)$$

It is assumed that the cross-sectional area of the liquid is constant along the length of the groove. For a constant heat flux in both the evaporator and condenser sections, eqn. (39) can be integrated to determine the total pressure drop in the helical groove.

$$\Delta p_l = L_{\mathrm{eff}} \left(\frac{\mu_l \overline{v}_{l,\mathrm{max}}}{h_l^2 \overline{v_0^*}} - \frac{4\mu_v \overline{v}_{v,\mathrm{max}}}{h_l R_v \tau_{lv,0}^*} \right) \sqrt{ \left(\frac{2\pi R_h}{L_p} \right)^2 + 1} \qquad (40)$$

The maximum liquid velocity in a groove is

$$\overline{v}_{l,\mathrm{max}} = \frac{\dot{Q}_g}{\rho_l A_l h_{\mathrm{fg}}} \qquad (41)$$

Similarly, the maximum vapor velocity is

$$\overline{v}_{v,\mathrm{max}} = \frac{\dot{Q}_t}{\pi R_v^2 \rho_v h_{\mathrm{fg}}} \qquad (42)$$

where the total heat transported by the heat pipe accounts for the contributions by all of the individual grooves.

$$\dot{Q}_t = \sum_{i=1}^{N_g} \dot{Q}_{g,i} \qquad (43)$$

Using the above relations, the liquid pressure drop in a groove as a function of the transported heat is

$$\Delta p_l = \frac{L_{\text{eff}}}{h_{\text{fg}}} \left(\frac{\mu_l \dot{Q}_g}{h_l^2 \overline{v_0^*} \rho_l A_l} - \frac{4\mu_v \dot{Q}_t}{\pi h_l R_v^3 \rho_v \tau_{lv,0}^*} \right) \sqrt{\left(\frac{2\pi R_h}{L_p} \right)^2 + 1} \qquad (44)$$

The body forces imposed on the fluid within a particular groove may either aid or hinder the return of the fluid to the evaporator, depending on the groove pitch L_p and the circumferential location of the starting point of the helical groove (Thomas et al., 1998; Klasing et al., 1999). However, even if the body force hinders the return of the fluid, each groove contributes to the heat transported $\dot{Q}_t$. Therefore, the capillary limit equation [eqn. (32)] was first solved for the heat transported by each individual groove $\dot{Q}_g$, and the results were summed to determine the total heat transport $\dot{Q}_t$. Since the pressure drop in the vapor space and the pressure drop in each groove were functions of the total heat transport, eqn. (32) was solved iteratively. The body forces due to acceleration and gravity were integrated over the length of the groove to find the average pressure drop (Thomas et al., 1998).

$$\Delta p_{\text{bf}} = -\rho_l \left[\int_0^{L_t} \widehat{e}_{x_3} \cdot \left(-\vec{A} + \{-g\}\widehat{e}_{z_1} \right) \, ds \right] \sqrt{\left(\frac{2\pi R_h}{L_p} \right)^2 + 1} \qquad (45)$$

Combining the above relations, the general expression for the maximum capillary limit for a single helical groove which accounts for shear stress at the liquid-vapor interface and the effect of groove fill ratio is given by

$$\frac{\sigma}{R_c} \geq \frac{L_{\text{eff}}}{h_{\text{fg}}} \left\{ \frac{8\mu_v \dot{Q}_t}{\pi \rho_v R_v^4} + \left(\frac{\mu_l \dot{Q}_g}{h_l^2 \overline{v_0^*} \rho_l A_l} - \frac{4\mu_v \dot{Q}_t}{\pi h_l R_v^3 \rho_v \tau_{lv,0}^*} \right) \sqrt{\left(\frac{2\pi R_h}{L_p} \right)^2 + 1} \right\}$$
$$- \rho_l \left[\int_0^{L_t} \widehat{e}_{x_3} \cdot \left(-\vec{A} + \{-g\}\widehat{e}_{z_1} \right) \, ds \right] \sqrt{\left(\frac{2\pi R_h}{L_p} \right)^2 + 1} \qquad (46)$$

A closed-form solution for the capillary limit of a heat pipe with straight axial grooves and no body forces can be derived from eqn. (46).

$$\dot{Q}_{\text{cap}} = \frac{\sigma h_{\text{fg}}}{R_c L_{\text{eff}}} \left[\frac{\mu_l}{N_g h_l^2 \overline{v_0^*} \rho_l A_l} + \frac{8\mu_v}{\pi \rho_v R_v^4} \left(1 - \frac{R_v}{2h_l \tau_{lv,0}^*} \right) \right]^{-1} \qquad (47)$$

Figure 18(a) shows the results of the closed-form solution [eqn. (47)]. The groove geometry given by Castle et al. (2000) was used, except that straight axial grooves were assumed ($L_p \to \infty$) instead of helical grooves. Table 32 gives the results of the computer model for the geometry analyzed by Castle et al. (2000) for a shear stress of $\tau_{lv,a}^* = 5.0$. This information was used as part of the two-point numerical solution, along with the data presented in Table 31 for $\overline{v_0^*}$. Over the range of groove fill ratio examined, the capillary limit increased with A_l/A_g by more than three orders of magnitude. For this case, the semi-analytical solution and the two-point numerical solution were nearly identical due to the low vapor velocities, and hence the low liquid-vapor shear stress. This point is further demonstrated in Fig. 18(a) by the graph indicated by "No Shear," where the term in eqn. (47) that accounts for the effect of liquid-vapor shear on the liquid was dropped by allowing $\tau_{lv,0}^* \to -\infty$. The maximum difference in the closed form solution compared to the two-point numerical solution was 5%. The capillary limit decreases when shear stress is accounted for, as expected. Figure 18(b) shows the closed-form solution when water is the working fluid. In this case, the difference between the results of the two-point numerical solution and the no-shear solution is much more pronounced (45% maximum difference) due to the significantly higher vapor velocities involved. The agreement between the semi-analytical solution and the two-point numerical solution is quite good. The semi-analytical solution offers very close results with a significantly reduced amount of computer resources required.

The capillary limit prediction for the helically-grooved heat pipe given by eqn. (46) is shown in Fig. 19 using the semi-analytical solution [eqn. (19)] for $|\vec{a}_r| = 0.0$ and 10.0-g. The capillary limit heat transfer increases both with groove fill ratio and working temperature. In addition, $\dot{Q}_{\text{cap}}$ increases significantly with the radial acceleration due to the improved liquid pumping ability of the helical grooves (Thomas et al., 1998).

The experimental data collected by Castle et al. (2000) for the capillary limit of a revolving helically-grooved heat pipe versus radial acceleration rates are shown in Fig. 20, along with the predictions of the present semi-analytical model and that
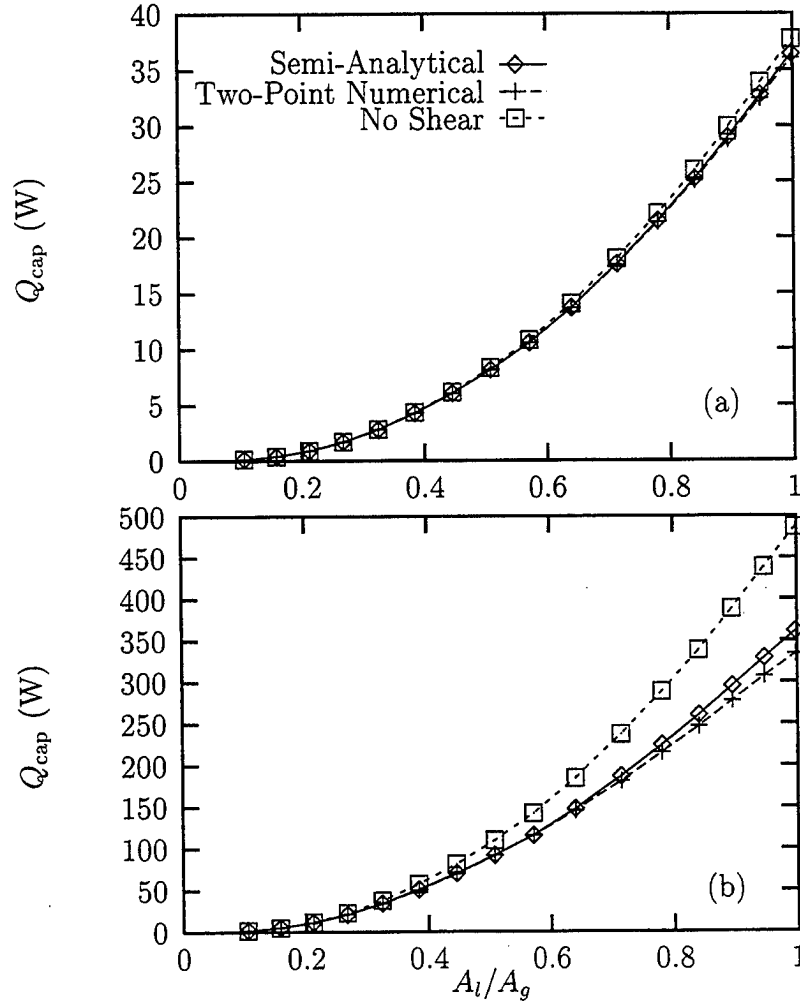
Figure 18: Maximum heat transport predicted by the closed-form solution versus groove fill ratio (Straight axial grooves, no body forces, $T_{sat} = 40°C$): (a) Ethanol; (b) Water.
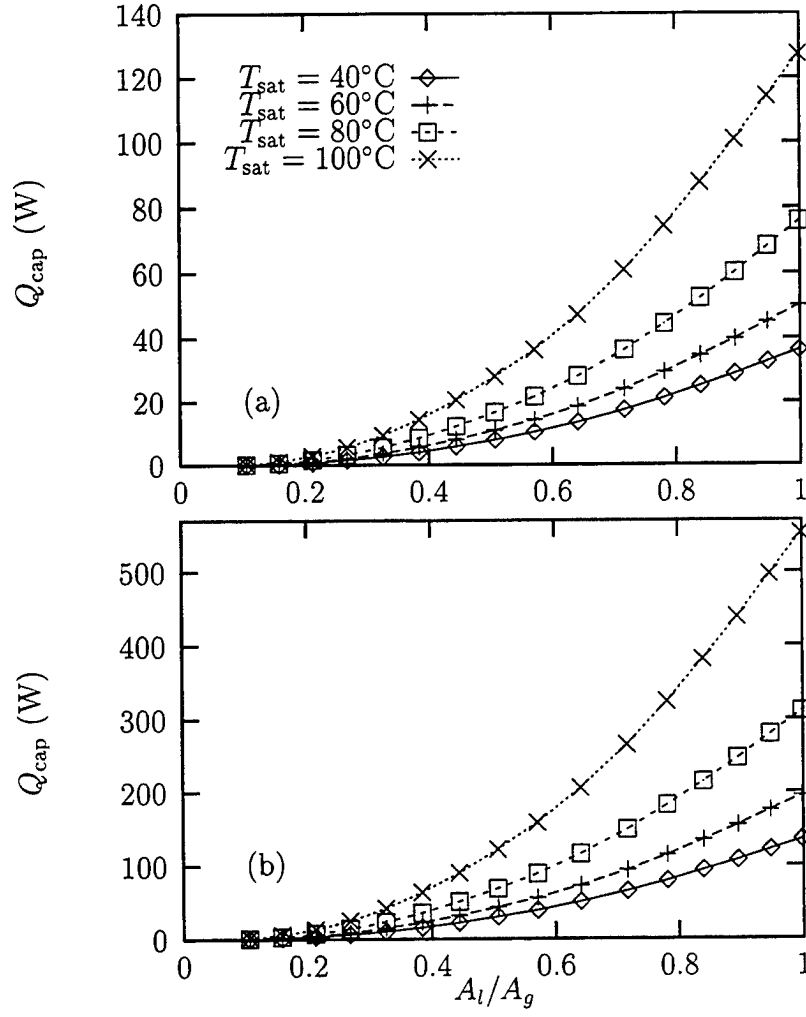
Figure 19: Maximum heat transport versus groove fill ratio for several working temperatures (Ethanol): (a) $|\vec{a}_r| = 0.0$-g; (b) $|\vec{a}_r| = 10.0$-g.

given by Castle et al. (2000). During the experiments, the working temperature was not held constant, so the present model was evaluated at the saturation temperature reported for a given value of radial acceleration. For a groove fill ratio of $A_l/A_g = 0.5$ [Fig. 20(a)], the present model more closely matches the experimental data than the model by Castle et al. (2000), which did not account for the groove fill ratio or liquid-vapor shear stress. The maximum difference in the experimental and analytical results by Castle et al. (2000) was 418%, whereas the maximum difference for the current model was 104%. For $A_l/A_g = 1.0$ [Fig. 20(b)], the present model overpredicts the experimental data by a maximum difference of 158% and the previous model by 87%.

1.5 Conclusions

A numerical study has been concluded where the mean velocity, Poiseuille number, and volumetric flow rate of liquid in a trapezoidal groove have been determined as functions of groove geometry, meniscus contact angle and shear stress at the liquid-vapor interface. The mean velocity and volumetric flow rate have been shown to be linear functions of shear stress, and the Poiseuille number is a strong function of the shear stress for countercurrent flow. A semi-analytical solution and a two-point numerical solution for the mean velocity were presented and used to predict the capillary limit of a revolving helically-grooved heat pipe for various groove fill ratios. Interfacial shear stress due to countercurrent flow in a heat pipe decreases the maximum heat transport. For cases in which the vapor velocities are high, this effect is more pronounced. The groove fill ratio was shown to have a significant impact on heat pipe performance. Underfilling the heat pipe examined by 10% resulted in a decrease in the predicted capillary limit by approximately 17 to 20% for water and ethanol, respectively.
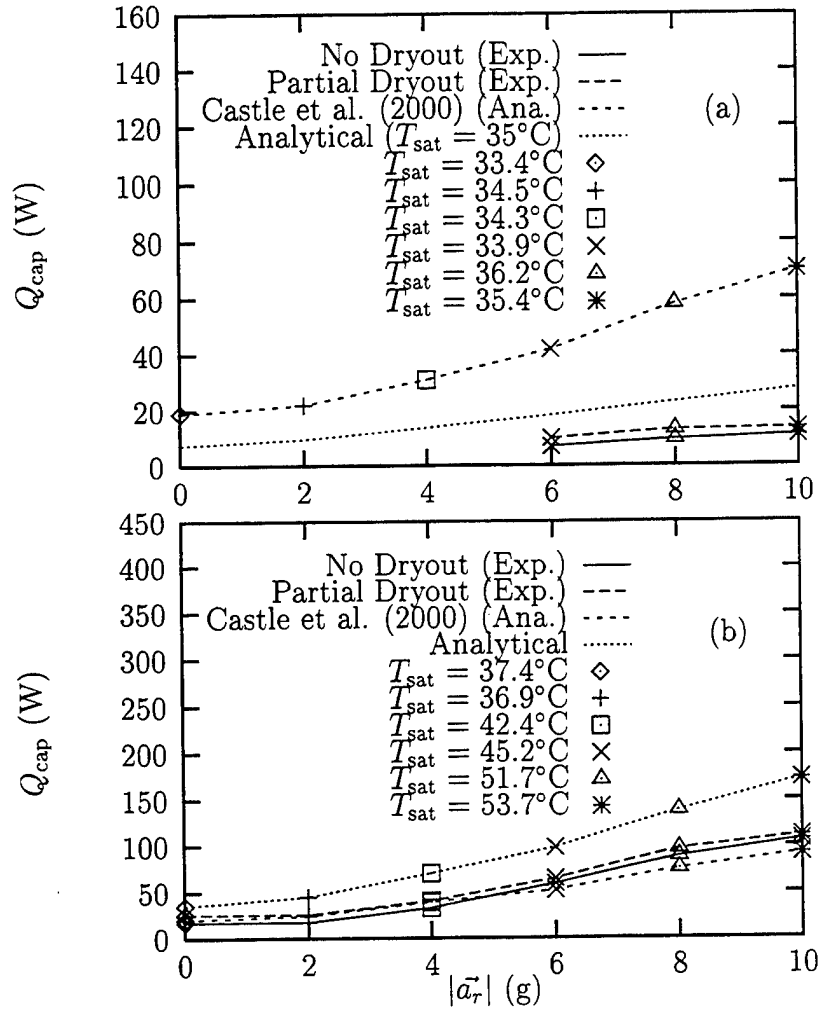
Figure 20: Maximum heat transport versus radial acceleration: (a) $A_l/A_g = 0.5$; (b) $A_l/A_g = 1.0$.

2 Fully Developed Laminar Flow in Sinusoidal Grooves

2.1 Introduction

Isotropic materials such as quartz glass or borosilicate glass can be chemically etched to form micro-grooves for the enhancement of evaporative heat transfer in chip-level devices (Kirshberg et al., 1999). A typical etched profile in glass is shown in Fig. 21, where the profile is smooth instead of having sharp corners seen in the etching of crystalline materials such as silicon (Maluf, 2000). While many studies have been performed on sharp-cornered geometries [triangular grooves (Ayyaswamy et al., 1974; Ma et al., 1994; Romero and Yost, 1996; Lin and Faghri, 1997; Kolodziej et al., 1999), rectangular grooves (DiCola, 1968; Schneider and DeVos, 1980; Khrustalev and Faghri, 1999), and trapezoidal grooves (Hopkins et al., 1999)], very little information is available in the open literature on the flow of liquid in rounded-corner geometries. Stroes and Catton (1997) compared the capillary performance of triangular and sinusoidal grooves by means of an experimental study. Two sets of grooves were machined into stainless steel test plates such that the cross-sectional areas of the grooves were equal. Strip heaters were placed under the plates to provide heat input. The test plates were placed at inclination angles of 4 and 6° and ethanol was added to the grooves until the liquid reached the lands of the grooves. The average wetted length of each set of grooves was recorded as the heat input was varied from 0 to 25 W. The study showed that the triangular grooves had a greater capillary pumping ability compared to the sinusoidal grooves with the same cross-sectional area, inclination angle, and heat input. Stroes and Catton postulated that this was due to the axial rate of change of the radius of curvature of the meniscus. Sinusoidal grooves, however, could dissipate a given heat input with a smaller wetted area than triangular grooves due to the larger wetted perimeter found with sinusoidal grooves. The objective of the present study was to examine the fully-developed laminar flow

41
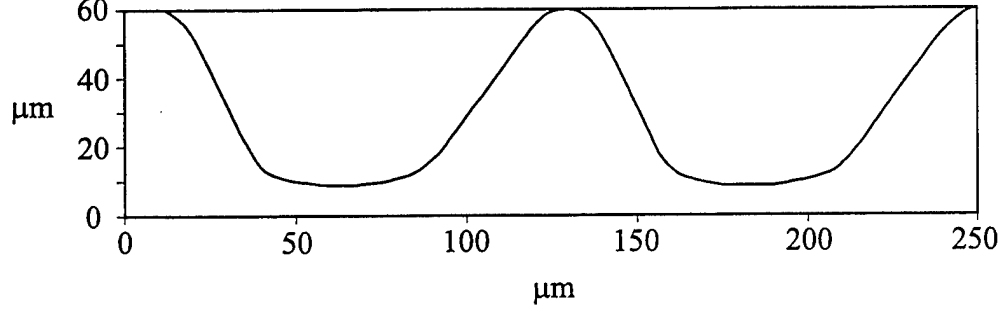
Figure 21: Grooves chemically etched in glass (Courtesy of D. Liepmann, University of California at Berkeley).

of liquid in sinusoidal grooves. The effects of countercurrent and cocurrent vapor flow over the liquid-vapor interface were investigated by relating the liquid velocity gradient to the friction factor of the vapor. The variation of the shear stress on the liquid-vapor interface (Khrustalev and Faghri, 1999) was neglected, and the liquid-vapor interface was assumed to be circular (Bo $\ll$ 1). The mean velocity, volumetric flow rate and Poiseuille number were determined as functions of the interfacial shear stress, the meniscus contact angle, the groove aspect ratio and the amount that the groove was filled.

2.2 Mathematical Model

A constant property liquid flows steadily in a sinusoidal groove as shown in Fig. 22. A meniscus, which is assumed to be circular, comprises the liquid-vapor interface. For fully developed laminar flow, the conservation of mass and momentum equations reduce to the classic Poisson equation in dimensionless form (White, 1991)

$$\frac{\partial^2 v^*}{\partial x^{*2}} + \frac{\partial^2 v^*}{\partial z^{*2}} = -1 \tag{48}$$

On the groove wall, the no-slip condition is in effect.

$$v^* = 0 : \quad 0 \le x^* \le w_l^*/2, \quad z^* = \frac{1}{2}\left\{1 + \cos\left[-\pi\left(\frac{x^*}{\beta} + 1\right)\right]\right\} \tag{49}$$

At the line of symmetry, the velocity gradient is zero in the x^* direction

$$\frac{\partial v^*}{\partial x^*} = 0 : \quad x^* = 0, \quad 0 \le z^* \le h_l^* + R^*\sqrt{1 - \left(\frac{w_l^*}{2R^*}\right)^2} - R^* \tag{50}$$

42
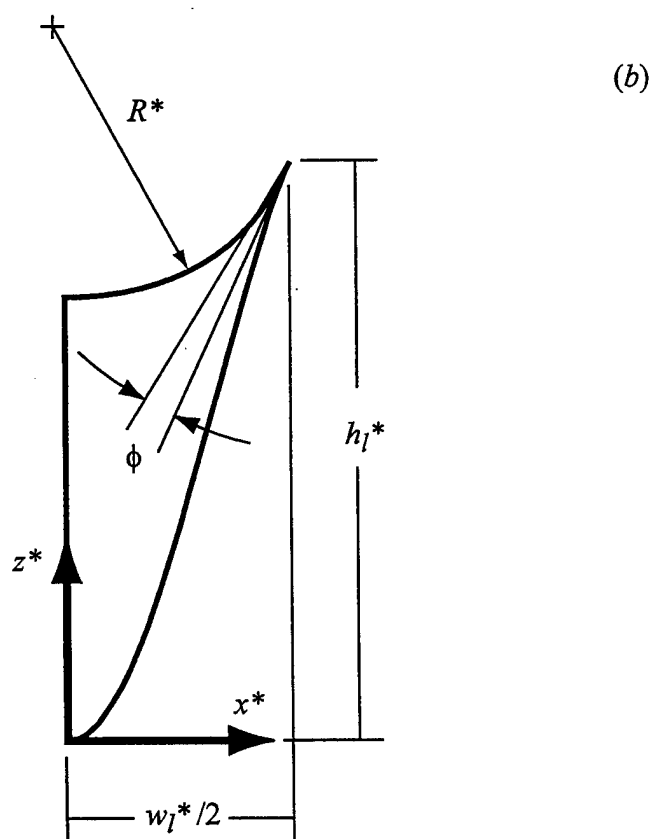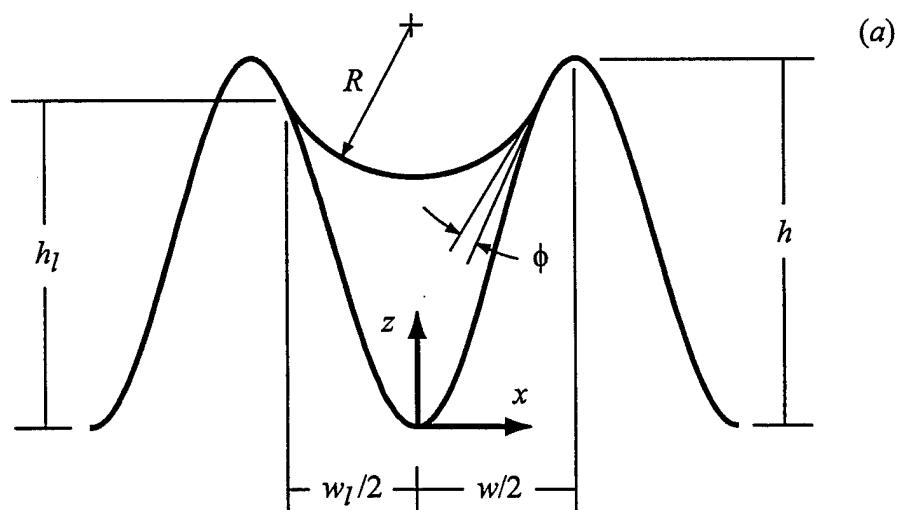
Figure 22: Flow of liquid in a sinusoidal groove: (*a*) Definition of geometric parameters; (*b*) Dimensionless solution domain.

The dimensionless radius of curvature is given by

$$R^* = \left(\frac{w_l^*}{2}\right)\left[1 + \frac{(1 + d^* \tan\phi)^2}{(d^* - \tan\phi)^2}\right]^{\frac{1}{2}} \tag{51}$$

where

$$d^* = \frac{\pi}{2\beta}\sin\left[-\pi\left(\frac{w_l^*}{2\beta} + 1\right)\right] \tag{52}$$

The maximum value for the meniscus contact angle ϕ for a wetting fluid can be determined for a given geometry by allowing the radius of curvature to approach $R^* \to \infty$.

$$\phi_{\max} = \tan^{-1}\left\{\frac{\pi}{2\beta}\sin\left[-\pi\left(\frac{w_l^*}{2\beta} + 1\right)\right]\right\} \tag{53}$$

At the liquid-vapor interface, a uniform shear stress is imposed in the y direction.

$$\frac{\partial v^*}{\partial n^*} = \tau_{lv}^* : \ 0 \le x^* \le w_l^*/2, \ z^* = h_l^* + R^*\sqrt{1 - \left(\frac{w_l^*}{2R^*}\right)^2} - \sqrt{R^{*2} - x^{*2}} \tag{54}$$

The dimensional shear stress at the liquid-vapor interface can be cast in terms of the friction factor of the vapor.

$$\tau_{lv} = \begin{cases} \left[\dfrac{\rho_v\,(\overline{v}_v)^2}{2}\right]f_v & \text{for cocurrent flow} \\[4mm] -\left[\dfrac{\rho_v\,(\overline{v}_v)^2}{2}\right]f_v & \text{for countercurrent flow} \end{cases} \tag{55}$$

The Poiseuille number of the liquid in the groove is given by

$$\text{Po} = f\text{Re} = \frac{D_h^{*2}}{2\overline{v^*}} \tag{56}$$

The dimensionless hydraulic diameter for the flow of liquid in a sinusoidal groove with a circular meniscus is $D_h^* = 4A_l^*/P^*$, where the dimensionless cross-sectional area of the liquid is given by

$$A_l^* = \frac{w_l^*}{2}(2h_l^* - 1) - R^*\left[R^*\cos^{-1}\sqrt{1 - \left(\frac{w_l^*}{2R^*}\right)^2} - \left(\frac{w_l^*}{2}\right)\sqrt{1 - \left(\frac{w_l^*}{2R^*}\right)^2}\right]$$
$$+ \left(\frac{\beta}{\pi}\right)\sin\left[-\pi\left(\frac{w_l^*}{2\beta} + 1\right)\right] \quad \text{for } \phi < \phi_{\max} \tag{57}$$

44

$$A_l^* = \frac{w_l^*}{2}(2h_l^* - 1) + \left(\frac{\beta}{\pi}\right)\sin\left[-\pi\left(\frac{w_l^*}{2\beta} + 1\right)\right] \quad \text{for } \phi = \phi_{\max} \tag{58}$$

The dimensionless wetted perimeter is given by the following integral equation.

$$P^* = 2\int_0^{w_l^*/2}\sqrt{1 + \left(\frac{\pi}{2\beta}\right)^2 \sin^2\left[-\pi\left(\frac{x^*}{\beta} + 1\right)\right]}\, dx^* \tag{59}$$

The mean velocity is defined as

$$\overline{v^*} = \frac{2}{A_l^*}\int_0^{w_l^*/2}\int_0^{z^*} v^*\, dz^*\, dx^* \tag{60}$$

See Appendix B for derivations of the dimensionless Poisson equation, dimensionless boundary conditions, and dimensionless liquid cross-sectional area and perimeter.

2.3 Numerical Model

The elliptic Poisson equation given by eqn. (48) with mixed boundary conditions [eqns. (49), (50) and (54)] was solved using Gauss-Seidel iteration with a central differencing scheme and successive over-relaxation (Anderson et al., 1984). The convergence criteria for the iterative solution was set to $\epsilon = 10^{-10}$ for each case. A grid independence check was made in which the number of grids in each direction was doubled. When the value for the Poiseuille number did not change by more than 1%, grid independence was considered to be reached. The convergence criteria was then reduced by an order of magnitude while maintaining the highest number of grids. If the Poiseuille number did not change by more than 1%, the solution was considered to be independent of both grid size and ϵ. Otherwise, a grid independence check was made at the smaller value of ϵ until a converged solution was reached. The integral equation for the wetted perimeter [eqn. (59)] was integrated numerically since no closed-form solution exists.

The numerical model was tested against an existing solution in the archival literature. Shah (1975) determined the friction factors for the laminar flow within ducts of various cross sections using a least-squares-matching technique. Table 3 shows the comparison of the Poiseuille number between the present solution and that given by Shah (1975) for laminar flow in a family of sinusoidal ducts. The agreement is excellent, with a maximum difference of 1.1%.

Table 3: Poiseuille number versus sinusoidal duct aspect ratio: Comparison of the present solution with that given by Shah (1975).

β	Poiseuille Number, Po	
	Shah (1975)	Present
1/4	14.553	14.479
1/3	14.022	13.931
1/2	13.023	12.935
$1/\sqrt{3}$	12.630	12.543
2/3	12.234	12.148
1	11.207	11.115
2	10.123	10.061
4	9.743	9.6373

2.4 Results and Discussion

A numerical study has been completed in which the flow of liquid in a sinusoidal groove has been solved. Figure 23 presents contour plots of the dimensionless liquid velocity. The maximum liquid velocity increases with cocurrent shear, and decreases with countercurrent shear, as expected. For countercurrent vapor flow, a portion of the liquid flows in the $-y$ direction, which is opposite to the direction of the pressure gradient. This flow reversal shows the potential of the vapor shear to drive the mean velocity of the liquid to zero, or to completely reverse the flow, depending on the magnitude of the pressure gradient.

Figure 24 and Table 39 show the mean velocity, volumetric flow rate and Poiseuille number versus shear stress at the liquid-vapor interface for several values of the meniscus contact angle. The mean velocity increases with both τ_{lv}^* and ϕ, but is a relatively weak function of ϕ. For a given value of meniscus contact angle, the mean velocity is linear with τ_{lv}^* due to an overall force balance on the liquid. The volumetric flow rate also increases with τ_{lv}^* and ϕ, but is a much stronger function of ϕ due to the increase in the cross-sectional area of the liquid. The Poiseuille number decreases as τ_{lv}^* increases. For cocurrent vapor flow ($\tau_{lv}^* > 0$), Po decreases steadily with τ_{lv}^*. For countercurrent flow, Po increases dramatically with $-\tau_{lv}^*$ due to the mean velocity approaching zero. In general, Po increases with ϕ due to the increase in the hydraulic

46
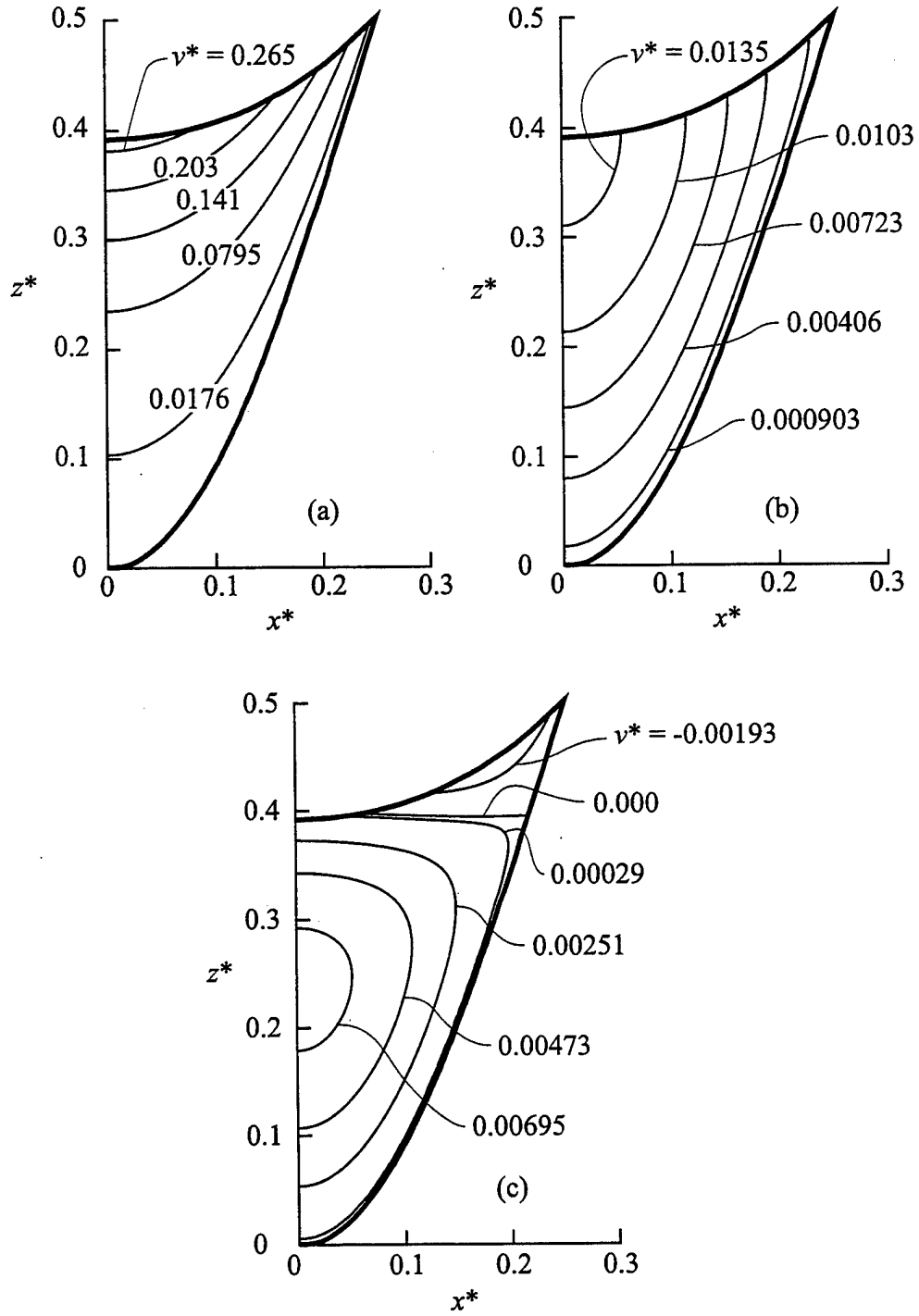
Figure 23: Dimensionless velocity fields for laminar flow in a sinusoidal groove ($\beta = 0.5$, $w_l^*/2 = 0.25$, $\phi = 25°$): (a) $\tau_{lv}^* = 2.0$ (cocurrent flow); (b) $\tau_{lv}^* = 0.0$; (c) $\tau_{lv}^* = -0.1$ (countercurrent flow).

diameter of the liquid.

Figure 25 and Table 40 present the mean velocity, volumetric flow rate and Poiseuille number versus the groove fill ratio for several values of the groove aspect ratio. The mean velocity increases monotonically with area ratio and groove aspect ratio. The volumetric flow rate also increases with w_l^*/w^* and β, but drops off rapidly for $w_l^*/w^* < 0.5$ due to the decrease in flow area. The Poiseuille number is relatively constant for this case. For $\beta \geq 0.5$, Po decreases and then increases with area ratio. For $\beta = 0.25$, Po increases over the range of w_l^*/w^* examined.

2.5 Semi-Analytical Solution for $\overline{v^*}$

As seen in Fig. 24(a), the mean velocity is a linear function of the imposed shear stress at the liquid-vapor interface. Since a direct numerical simulation of the liquid flow field for a number of values of the shear stress is computer resource intensive, it is appropriate to seek a semi-analytical expression for $\overline{v^*}$. Figure 26(a) shows the definition of the parameters involved, where the mean velocity when the shear stress is zero ($\overline{v_0^*}$) is given by the numerical solution. The value for the liquid-vapor shear for which the mean velocity is zero ($\tau_{lv,0}^*$) is given by the following force balance analysis. Figure 26(b) shows a differential element of the liquid in the groove. A force balance between the pressure drop and the shear forces at the liquid-vapor interface and at the wall results in the following relation.

$$p_y A_l - p_{y+dy} A_l + \tau_{lv} A_{lv} - \overline{\tau_w} A_w = 0 \qquad (61)$$

The areas over which the shear stresses τ_{lv} and $\overline{\tau_w}$ act are $A_{lv} = P_{lv} dy$ and $A_w = P dy$, respectively. Using these areas and nondimensionalizing gives

$$A_l^* + \tau_{lv}^* P_{lv}^* - \overline{\tau_w^*} P^* = 0 \qquad (62)$$

For Poiseuille flow in ducts of arbitrary cross section, and combined Couette-Poiseuille flow between flat plates, the shear stress at the wall is related to the mean velocity of the fluid by a constant (White, 1991). Therefore, in the present analysis, it is assumed that this also holds for the flow of liquid in a sinusoidal groove with an imposed shear
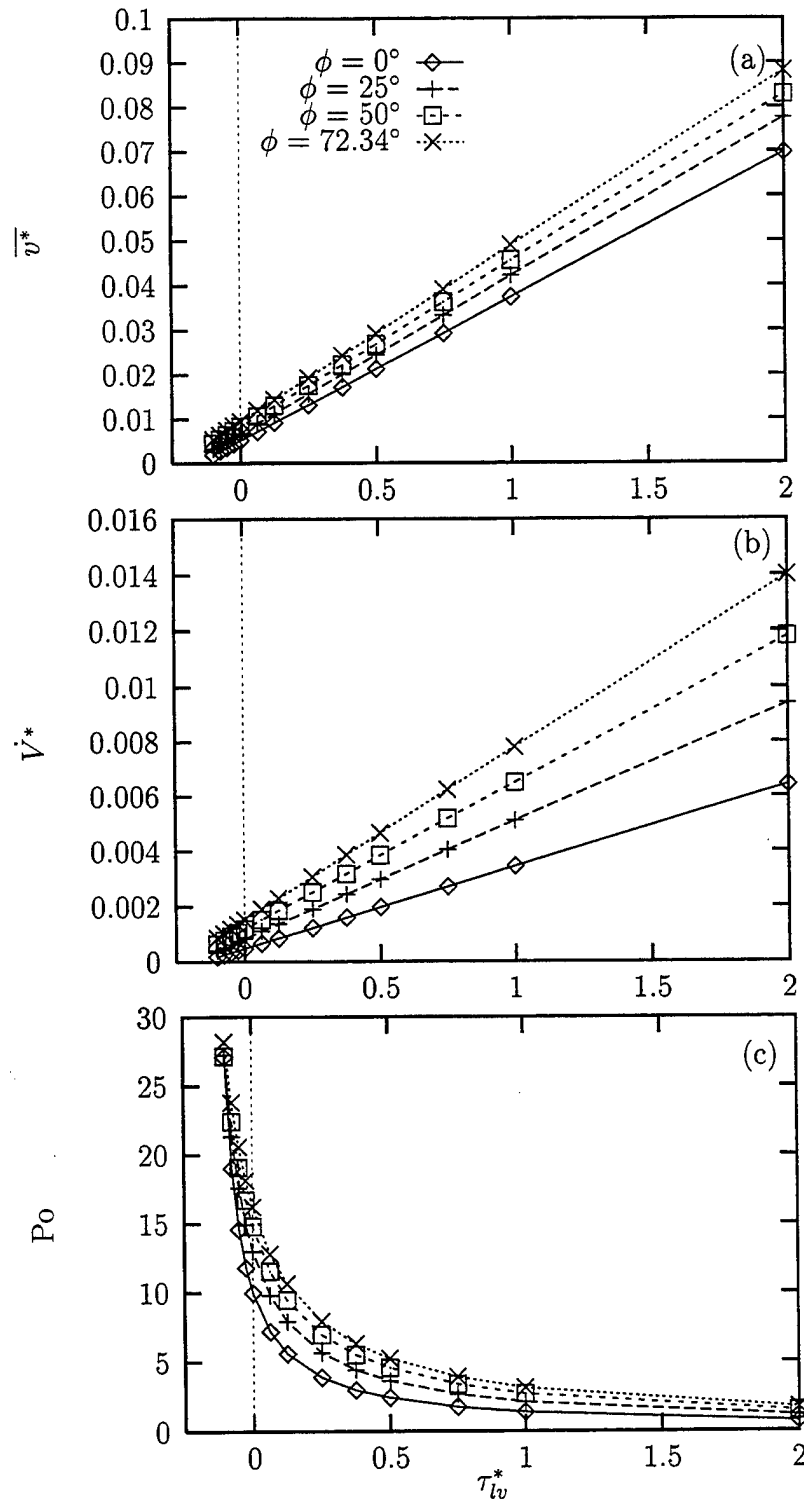
Figure 24: Variation of the flow variables with shear stress at the liquid-vapor interface for various values of meniscus contact angle ($\beta = 0.5$, $w_l^*/2 = 0.25$, $P^* = 1.15245$): (a) Mean velocity; (b) Volumetric flow rate; (c) Poiseuille number.

49
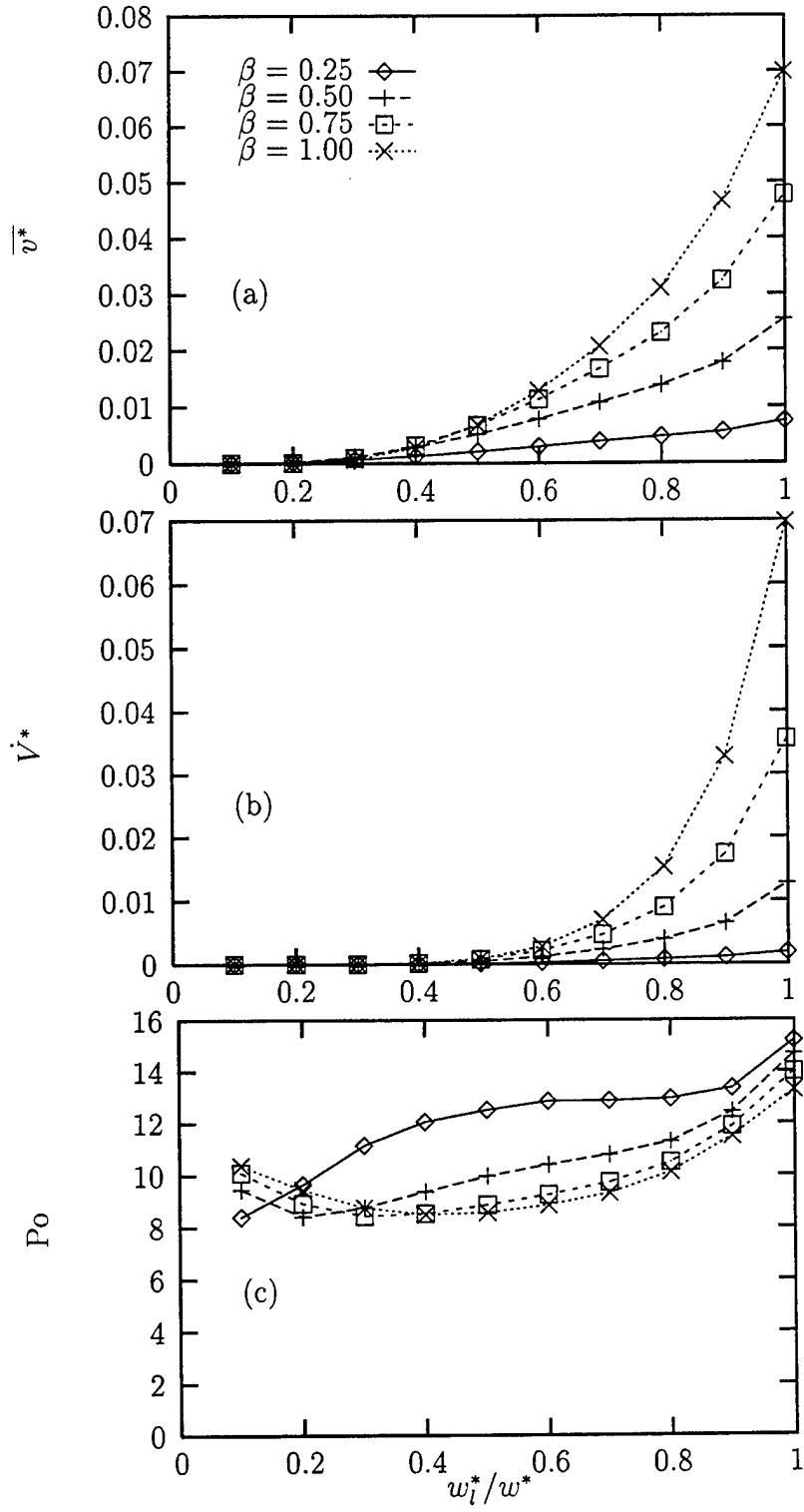
Figure 25: Variation of the flow variables with groove fill ratio for various values of groove aspect ratio ($\tau_{lv}^* = 0.0$, $\phi = 0°$): (a) Mean velocity; (b) Volumetric flow rate; (c) Poiseuille number.

50
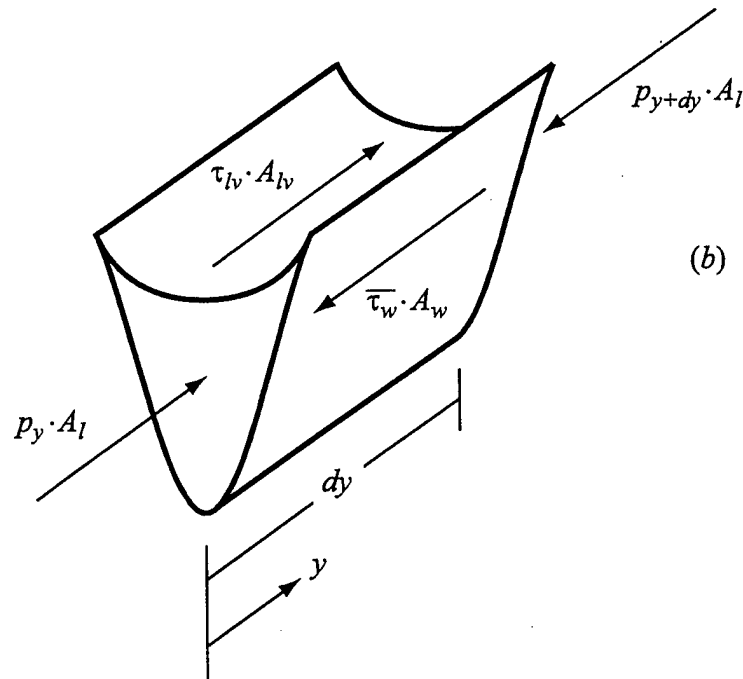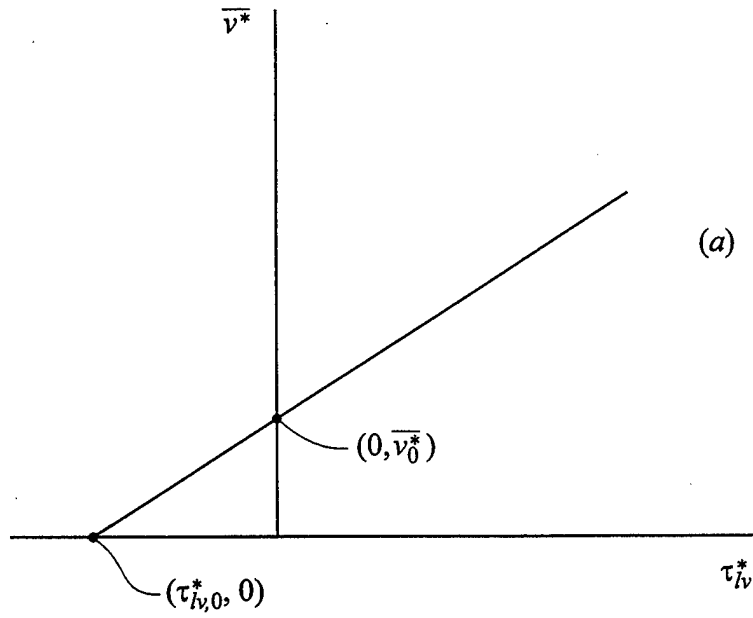
Figure 26: Semi-analytical solution for $\overline{v^*}$: (a) Definition of parameters; (b) Force balance on the liquid in a sinusoidal groove.

51

stress at the liquid-vapor interface.

$$\overline{\tau_w^*} = C_1 \overline{v^*} \tag{63}$$

It should be noted that the constant C_1 is probably a function of the groove geometry and meniscus contact angle. However, since the objective of this analysis is to determine the liquid-vapor shear stress when the mean liquid velocity is zero, this functionality is unimportant. The perimeter of the liquid-vapor interface is

$$P_{lv}^* = 2R^* \sin^{-1}\left(\frac{w_l^*}{2R^*}\right) \tag{64}$$

Substituting these relations into the force balance equation results in the following expression for mean velocity.

$$\overline{v^*} = \frac{1}{C_1 P^*}\left[A_l^* + 2\tau_{lv}^* R^* \sin^{-1}\left(\frac{w_l^*}{2R^*}\right)\right] \tag{65}$$

The mean velocity is zero when

$$\tau_{lv,0}^* = -\frac{A_l^*}{2R^* \sin^{-1}\left(\dfrac{w_l^*}{2R^*}\right)} \tag{66}$$

Figure 27(a) shows the results of eqn. (66). The numerical results shown in Fig. 24(a) were extrapolated to determine the values for shear stress at the liquid-vapor interface when $\overline{v^*} = 0$. Both curves indicate that $\tau_{lv,0}^*$ increases with ϕ due to the increasing depth of liquid in the groove. The maximum difference between the numerical and analytical data is 34%. The equation for the mean velocity as a function of the shear stress is given by

$$v' = \overline{v^*}/\overline{v_0^*} = 1 - \tau' \tag{67}$$

where $\tau' = \tau_{lv}^*/\tau_{lv,0}^*$. The semi-analytical solution for the normalized mean velocity is shown in Fig. 27(b) with the corresponding numerical data presented in Fig. 24. Equation (67) predicts 94% of the data to within $\pm$20% over the range of meniscus contact angle examined.
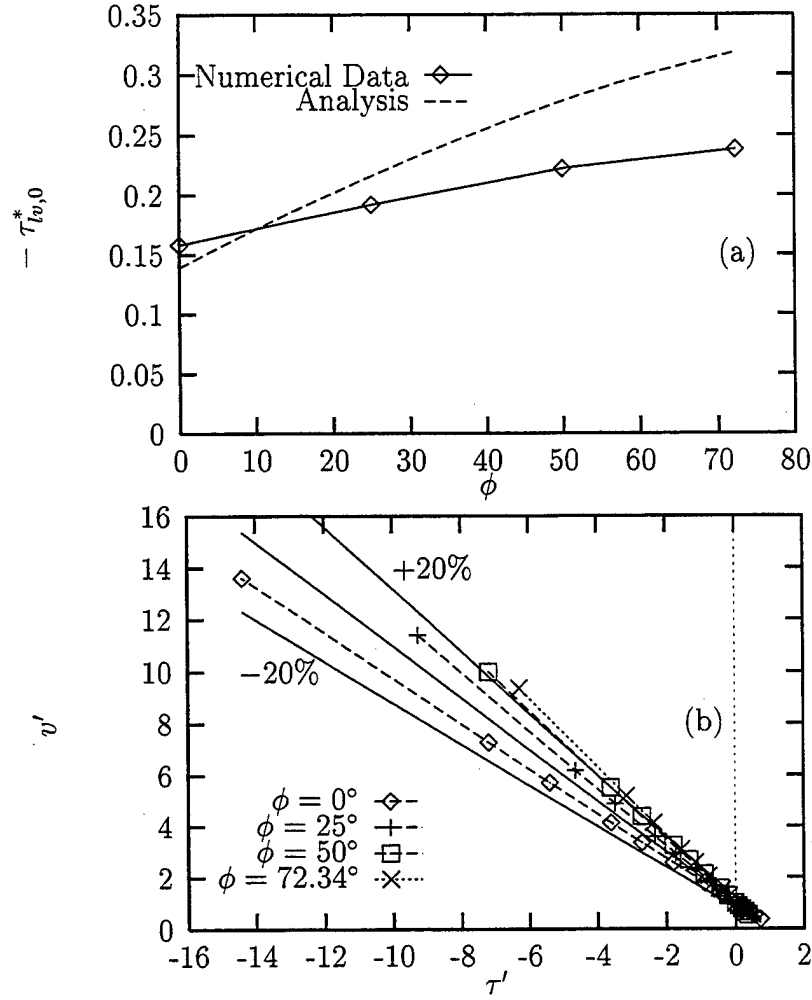
Figure 27: Comparison of the semi-analytical solution with numerical data ($\beta = 0.5$, $w_l^*/2 = 0.25$): (a) Countercurrent vapor shear stress required for $\overline{v^*} = 0$; (b) Normalized mean velocity versus normalized shear stress at the liquid-vapor interface.

2.6 Conclusions

Based on the results of the numerical model of the flow of liquid in a sinusoidal groove, the following conclusions have been made: For a given meniscus contact angle, the mean velocity was linear with imposed shear stress at the liquid-vapor interface. The volumetric flow rate in the groove was negligible for groove fill ratios of less than $w_l^*/w^* < 0.5$. The Poiseuille number was a strong function of the countercurrent shear stress. A semi-analytical expression was provided to approximate the mean velocity as a function of the shear stress at the liquid-vapor interface.

3 References

Anderson, D., Tannehill, J., and Pletcher, R., 1984, *Computational Fluid Mechanics and Heat Transfer*, Hemisphere, New York.

Ayyaswamy, P., Catton, I., and Edwards, D., 1974, "Capillary flow in triangular grooves," *ASME J. Appl. Mech.*, Vol. 41, pp. 332-336.

Burden, R., and Faires, J., 1985, *Numerical Analysis*, 3rd edn., PWS Publishers, Boston.

Castle, R., Thomas, S., and Yerkes, K., 2000, "The effect of working fluid inventory on the performance of revolving helically-grooved heat pipes," accepted to the Proceedings of the 2000 National Heat Transfer Conference.

Chi, S., 1976, *Heat Pipe Theory and Practice: A Sourcebook*, Hemisphere Publ. Corp., New York.

DiCola, G., 1968, "Soluzionne analitica, amezzo della transformata di Fourier, di un problema di fusso in un canale rettangolare," Euratom C.C.R. Ispra (Italy), C.E.T.I.S.

Faghri, A., 1995, *Heat Pipe Science and Technology*, Taylor and Francis, Washington, D.C.

Hopkins, R., Faghri, A., and Khrustalev, D., 1999, "Flat miniature heat pipes with micro capillary grooves," *ASME Journal of Heat Transfer*, Vol. 121, pp. 102-109.

Khrustalev, D., and Faghri, A., 1999, "Coupled liquid and vapor flow in miniature passages with micro grooves," *ASME J. Heat Transfer*, Vol. 121, pp. 729-733.

Kirshberg, J., Liepmann, D., and Yerkes, K., 1999, "Micro-cooler for chip-level temperature control," *Proc. SAE Aerospace Power Systems Conf.*, Paper No. 1999-01-1407.

Klasing, K., Thomas, S., and Yerkes, K., 1999, "Prediction of the operating limits of revolving helically-grooved heat pipes," *ASME Journal of Heat Transfer*, Vol. 121,

pp. 213-217.

Kolodziej, J., Musielak, G., Kaczmarek, M., and Strek, T., 1999, "Determination of free surface and gravitational flow of liquid in triangular groove," *Computational Mechanics*, Vol. 24, pp. 110-117.

Lin, L., and Faghri, A., 1997, "Steady-state performance of a rotating miniature heat pipe," *AIAA J. Thermophysics Heat Transfer*, Vol. 11, pp. 513-518.

Ma, H., Peterson, G., and Lu, X., 1994, "The influence of vapor-liquid interactions on the liquid pressure drop in triangular microgrooves," *Int. J. Heat Mass Transfer*, Vol. 37, pp. 2211-2219.

Maluf, N., 2000, *An Introduction to Microelectromechanical Systems Engineering*, Artech House, Boston.

Romero, L., and Yost, F., 1996, "Flow in an open channel," *J. Fluid Mech.*, Vol. 322, pp. 109-129.

Ruckenstein, E., and Jain, R., 1974, "Spontaneous rupture of thin liquid films," *J. Chem. S.*, Vol. 70, pp. 132-147.

Schneider, G., and DeVos, R., 1980, "Non-dimensional analysis for the heat transport capability of axially grooved heat pipes including liquid/vapor interaction," AIAA Paper No. 80-0214.

Shah, R., 1975, "Laminar flow friction and forced convection heat transfer in ducts of arbitrary geometry," *Int. J. Heat Mass Transfer*, Vol. 18, pp. 849-862.

Shah, R., and London, A., 1978, *Laminar Flow Forced Convection in Ducts*, Academic, New York.

Stroes, G., and Catton, I., 1997, "An experimental investigation of the capillary performance of triangular versus sinusoidal channels," *ASME J. Heat Transfer*, Vol. 119, pp. 851-853.

Thomas, S., Klasing, K., and Yerkes, K., 1998, "The effects of transverse acceleration-induced body forces on the capillary limit of helically grooved heat pipes," *ASME Journal of Heat Transfer*, Vol. 120, pp. 441-451.

White, F., 1991, *Viscous Fluid Flow*, 2nd edn., McGraw-Hill, New York.

Nomenclature

A_g	cross-sectional area of the groove, m^2
A_l	cross-sectional area of the liquid, m^2
A_{lv}	area of the liquid-vapor interface, m^2
A_w	area of the groove wall, m^2
A_l^*	A_l/h^2
$\vec{a}_r$	radial acceleration vector, m/s^2
$\vec{A}$	acceleration vector at any point in the helical groove, m/s^2
b	distance from the liquid-vapor interface to the bottom of the groove, m
Bo	Bond number, $\rho g b^2/\sigma$
d^*	parameter defined in eqn. (6)
D	diffusion coefficient
D_h	hydraulic diameter, $4A_l/P$, m
D_h^*	D_h/h
F_1	mean velocity parameter, $h_l^2\overline{v^*}$, m^2
F_2	volumetric flow rate parameter, $h_l^4\dot{V}^*$, m^4
f	friction coefficient, $2\overline{\tau_w}/\rho\overline{v}^2$
g	acceleration due to gravity, m/s^2
h	groove height, m
h_{fg}	heat of vaporization, J/kg
h_l	height of the liquid in the groove at the wall, m
h_l^*	h_l/h
$\hat{i}$	unit vector in the x direction
$\hat{k}$	unit vector in the z direction
$\vec{k}$	curvature vector
L_a	adiabatic length, m
L_c	condenser length, m
L_e	evaporator length, m
L_{eff}	effective heat pipe length, $L_e/2 + L_a + L_c/2$, m
L_p	pitch length, m

L_t	total heat pipe length, m
$\dot{m}$	mass flow rate, kg/s
n	coordinate normal to the liquid-vapor interface
n^*	n/h
$\hat{n}$	unit vector normal to the liquid-vapor interface
N_g	number of grooves
p	pressure, N/m^2
P	wetted perimeter, m
P_{lv}	perimeter of the liquid-vapor interface, m
P^*	P/h
P_{lv}^*	P_{lv}/h
Po	Poiseuille number, $f\mathrm{Re}$, $D_h^{*2}/2\overline{v^*}$
$\dot{Q}_{\mathrm{cap}}$	capillary limit heat transfer, W
$\dot{Q}_g$	heat transfer due to a single groove, W
$\dot{Q}_t$	total heat transported, W
R	radius of curvature of the liquid-vapor interface, m
R_c	capillary radius, m
R_h	radius of the helix, m
R_v	radius of the heat pipe vapor space, m
R^*	R/h
R_b^*	dimensionless radius of curvature at bifurcation
Re	Reynolds number, $\rho\overline{v}D_h/\mu$
t	time, s
T_{sat}	saturation temperature, K
u	x-direction velocity, m/s
v	y-direction velocity, m/s
$\overline{v}$	mean y-direction velocity, m/s
$\overline{v}_{l,\max}$	maximum mean liquid velocity, m/s
$\overline{v}_{v,\max}$	maximum mean vapor velocity, m/s
v^*	$\mu v/h^2(-dp/dy)$

$\overline{v^*}$	dimensionless mean y-direction velocity
$\overline{v_0^*}$	dimensionless mean y-direction velocity when $\tau_{lv}^* = 0$
v'	$\overline{v^*}/\overline{v_0^*}$
$\dot{V}$	volumetric flow rate, $\overline{v}A_l$, m^3/s
$\dot{V}^*$	$\mu\dot{V}/[h^4(-dp/dy)]$
w	width of the bottom of the groove, m; z-direction velocity, m/s
w^*	w/h
w_l	width of the liquid in the groove, m
w_l^*	w_l/h
x, y, z	coordinate directions
x^*	x/h
z_1	distance from the liquid-vapor interface to the groove bottom, m
z^*	z/h
β	groove aspect ratio, $w/2h$
ϵ	convergence criteria
θ	groove half-angle, rad
μ	absolute viscosity, Pa-s
ρ	density, kg/m^3
σ	surface tension, N/m
τ_{lv}	shear stress at the liquid-vapor interface, N/m^2
τ_{lv}^*	$\tau_{lv}/h(-dp/dy)$
$\tau_{lv,0}^*$	shear stress at the liquid-vapor interface when $\overline{v^*} = 0$
$\overline{\tau_w}$	average shear stress at the wall, N/m^2
$\overline{\tau_w^*}$	$\overline{\tau_w}/h(-dp/dy)$
τ'	$\tau_{lv}^*/\tau_{lv,0}^*$
ϕ	meniscus contact angle, rad
ϕ_0	minimum meniscus contact angle, rad
ϕ_b	meniscus contact angle at bifurcation, rad
ω	over-relaxation parameter

A Derivation of Selected Expressions for Trapezoidal Grooves

A.1 Determination of dimensionless Poisson equation

The governing equations for fluid flow are the conservation of mass and conservation of momentum equations. The conservation of mass equation is given by White (1991).

$$\frac{\partial \rho}{\partial t} + \mathrm{div}\rho\vec{V} = 0 \tag{68}$$

The conservation of momentum equations (in scalar form) are also given by White (1991)

$$\rho\frac{Du}{Dt} = \rho g_x - \frac{\partial p}{\partial x} + \frac{\partial}{\partial x}\left(2\mu\frac{\partial u}{\partial x} + \lambda\,\mathrm{div}\vec{V}\right) + \frac{\partial}{\partial y}\left[\mu\left(\frac{\partial u}{\partial y} + \frac{\partial v}{\partial x}\right)\right]$$
$$+ \frac{\partial}{\partial z}\left[\mu\left(\frac{\partial w}{\partial x} + \frac{\partial u}{\partial z}\right)\right]$$

$$\rho\frac{Dv}{Dt} = \rho g_y - \frac{\partial p}{\partial y} + \frac{\partial}{\partial x}\left[\mu\left(\frac{\partial v}{\partial x} + \frac{\partial u}{\partial y}\right)\right] + \frac{\partial}{\partial y}\left(2\mu\frac{\partial v}{\partial y} + \lambda\,\mathrm{div}\vec{V}\right) \tag{69}$$
$$+ \frac{\partial}{\partial z}\left[\mu\left(\frac{\partial v}{\partial z} + \frac{\partial w}{\partial y}\right)\right]$$

$$\rho\frac{Dw}{Dt} = \rho g_z - \frac{\partial p}{\partial z} + \frac{\partial}{\partial x}\left[\mu\left(\frac{\partial w}{\partial x} + \frac{\partial u}{\partial z}\right)\right] + \frac{\partial}{\partial y}\left[\mu\left(\frac{\partial v}{\partial z} + \frac{\partial w}{\partial y}\right)\right]$$
$$+ \frac{\partial}{\partial z}\left(2\mu\frac{\partial w}{\partial z} + \lambda\,\mathrm{div}\vec{V}\right)$$

where

$$\lambda + \frac{2}{3}\mu = 0 \tag{70}$$

Expanding eqn. (68) and assuming incompressible flow ($\rho = $ constant) gives

$$\rho\left(\frac{\partial u}{\partial x} + \frac{\partial v}{\partial y} + \frac{\partial w}{\partial z}\right) = 0 \tag{71}$$

and upon simplification

$$\frac{\partial u}{\partial x} + \frac{\partial v}{\partial y} + \frac{\partial w}{\partial z} = 0 \tag{72}$$

Solving for λ in eqn. (70), substituting it into eqn. (69), and expanding $\mathrm{div}\vec{V}$ results in

$$\rho\frac{Du}{Dt} = \rho g_x - \frac{\partial p}{\partial x} + \frac{\partial}{\partial x}\left(2\mu\frac{\partial u}{\partial x} - \frac{2}{3}\mu\left[\frac{\partial u}{\partial x} + \frac{\partial v}{\partial y} + \frac{\partial w}{\partial z}\right]\right)$$

$$+ \frac{\partial}{\partial y}\left[\mu\left(\frac{\partial u}{\partial y} + \frac{\partial v}{\partial x}\right)\right] + \frac{\partial}{\partial z}\left[\mu\left(\frac{\partial w}{\partial x} + \frac{\partial u}{\partial z}\right)\right]$$

$$\rho\frac{Dv}{Dt} = \rho g_y - \frac{\partial p}{\partial y} + \frac{\partial}{\partial x}\left[\mu\left(\frac{\partial v}{\partial x} + \frac{\partial u}{\partial y}\right)\right]$$

$$+ \frac{\partial}{\partial y}\left(2\mu\frac{\partial v}{\partial y} - \frac{2}{3}\mu\left[\frac{\partial u}{\partial x} + \frac{\partial v}{\partial y} + \frac{\partial w}{\partial z}\right]\right) + \frac{\partial}{\partial z}\left[\mu\left(\frac{\partial v}{\partial z} + \frac{\partial w}{\partial y}\right)\right]$$

$$\rho\frac{Dw}{Dt} = \rho g_z - \frac{\partial p}{\partial z} + \frac{\partial}{\partial x}\left[\mu\left(\frac{\partial w}{\partial x} + \frac{\partial u}{\partial z}\right)\right] + \frac{\partial}{\partial y}\left[\mu\left(\frac{\partial v}{\partial z} + \frac{\partial w}{\partial y}\right)\right]$$

$$+ \frac{\partial}{\partial z}\left(2\mu\frac{\partial w}{\partial z} - \frac{2}{3}\mu\left[\frac{\partial u}{\partial x} + \frac{\partial v}{\partial y} + \frac{\partial w}{\partial z}\right]\right)$$

$$(73)$$

Assuming constant viscosity, substituting eqn. (72) into eqn. (73), and expanding the total derivatives, the conservation of momentum equations can be written as

$$\rho\left(\frac{\partial u}{\partial t} + u\frac{\partial u}{\partial x} + v\frac{\partial u}{\partial y} + w\frac{\partial u}{\partial z}\right) = \rho g_x - \frac{\partial p}{\partial x} + \mu\left(\frac{\partial^2 u}{\partial x^2} + \frac{\partial^2 u}{\partial y^2} + \frac{\partial^2 u}{\partial z^2}\right)$$

$$\rho\left(\frac{\partial v}{\partial t} + u\frac{\partial v}{\partial x} + v\frac{\partial v}{\partial y} + w\frac{\partial v}{\partial z}\right) = \rho g_y - \frac{\partial p}{\partial y} + \mu\left(\frac{\partial^2 v}{\partial x^2} + \frac{\partial^2 v}{\partial y^2} + \frac{\partial^2 v}{\partial z^2}\right) \qquad (74)$$

$$\rho\left(\frac{\partial w}{\partial t} + u\frac{\partial w}{\partial x} + v\frac{\partial w}{\partial y} + w\frac{\partial w}{\partial z}\right) = \rho g_z - \frac{\partial p}{\partial z} + \mu\left(\frac{\partial^2 w}{\partial x^2} + \frac{\partial^2 w}{\partial y^2} + \frac{\partial^2 w}{\partial z^2}\right)$$

Equation (74) can be simplified further by assuming steady flow ($\partial/\partial t = 0$) and that no body forces are acting on the fluid ($g_x = g_y = g_z = 0$). This simplification results in

$$\rho\left(u\frac{\partial u}{\partial x} + v\frac{\partial u}{\partial y} + w\frac{\partial u}{\partial z}\right) = -\frac{\partial p}{\partial x} + \mu\left(\frac{\partial^2 u}{\partial x^2} + \frac{\partial^2 u}{\partial y^2} + \frac{\partial^2 u}{\partial z^2}\right)$$

$$\rho\left(u\frac{\partial v}{\partial x} + v\frac{\partial v}{\partial y} + w\frac{\partial v}{\partial z}\right) = -\frac{\partial p}{\partial y} + \mu\left(\frac{\partial^2 v}{\partial x^2} + \frac{\partial^2 v}{\partial y^2} + \frac{\partial^2 v}{\partial z^2}\right) \qquad (75)$$

$$\rho\left(u\frac{\partial w}{\partial x} + v\frac{\partial w}{\partial y} + w\frac{\partial w}{\partial z}\right) = -\frac{\partial p}{\partial z} + \mu\left(\frac{\partial^2 w}{\partial x^2} + \frac{\partial^2 w}{\partial y^2} + \frac{\partial^2 w}{\partial z^2}\right)$$

Finally, by assuming fully developed flow ($u = w = 0$, $\partial v/\partial y = 0$) eqns. (72) and (75) reduce to

$$\text{Continuity}: \quad \frac{\partial v}{\partial y} = 0$$

$$\text{Momentum}: \quad \frac{\partial^2 v}{\partial x^2} + \frac{\partial^2 v}{\partial z^2} = \frac{1}{\mu}\frac{\partial p}{\partial y} \tag{76}$$

$$\frac{\partial p}{\partial x} = \frac{\partial p}{\partial z} = 0$$

Because v does not change with y, $\partial p/\partial y$ is constant, and the momentum equation reduces to the Poisson equation.

$$\frac{\partial^2 v}{\partial x^2} + \frac{\partial^2 v}{\partial z^2} = \frac{1}{\mu}\frac{dp}{dy} \tag{77}$$

The following definitions of dimensionless variables can be used to write the Poisson equation in dimensionless form

$$v^* = \frac{\mu v}{h^2(-dp/dy)} \quad x^* = \frac{x}{h} \quad z^* = \frac{z}{h} \tag{78}$$

Solving for v, x, and z gives

$$v = -\frac{1}{\mu}\frac{dp}{dy}v^* h^2 \quad x = x^* h \quad z = z^* h \tag{79}$$

Substituting these relationships into eqn. (77) gives

$$\frac{\partial^2 \left(-\frac{1}{\mu}\frac{dp}{dy}v^* h^2\right)}{\partial (x^* h)} + \frac{\partial^2 \left(-\frac{1}{\mu}\frac{dp}{dy}v^* h^2\right)}{\partial (z^* h)} = \frac{1}{\mu}\frac{dp}{dy} \tag{80}$$

Equation (80) can then be simplified to the Poisson equation in dimensionless form.

$$\frac{\partial^2 v^*}{\partial x^{*2}} + \frac{\partial^2 v^*}{\partial z^{*2}} = -1 \tag{81}$$

A.2 Determination of dimensionless boundary conditions

Figure 1 (a) and (b) shows liquid flow in a trapezoidal groove with the definitions of the dimensions used in the analysis. The no-slip boundary condition is applied to

the groove walls as shown below.

$$v = 0 : \begin{cases} 0 \leq x \leq w/2, \quad z = 0 \\[2mm] w/2 \leq x \leq w/2 + h\tan\theta, \quad z = (x - w/2)\cot\theta \quad \text{for} \quad \theta > 0 \\[2mm] x = w/2, \quad 0 \leq z \leq h \quad \text{for} \quad \theta = 0 \end{cases} \quad (82)$$

Using the definitions of the following dimensionless parameters,

$$v^* = \frac{\mu v}{h^2(-dp/dy)} \quad x^* = \frac{x}{h} \quad z^* = \frac{z}{h} \quad \beta = \frac{w}{2h} \quad (83)$$

the dimensional no-slip boundary condition can be written in dimensionless form as

$$v^* = 0 : \begin{cases} 0 \leq x^* \leq \beta, \quad z^* = 0 \\[2mm] \beta \leq x^* \leq \beta + \tan\theta, \quad z^* = (x^* - \beta)\cot\theta \quad \text{for} \quad \theta > 0 \\[2mm] x^* = \beta, \quad 0 \leq z^* \leq 1 \quad \text{for} \quad \theta = 0 \end{cases} \quad (84)$$

Along the centerline of the groove, the symmetry condition is used

$$\frac{\partial v}{\partial x} = 0 : \quad x = 0, \quad 0 \leq z \leq (h + d) - R \quad (85)$$

Using the dimensionless parameters from eqn. (83) and noting that

$$R^* = \frac{R}{h} \quad d^* = \frac{d}{h} \quad (86)$$

the symmetry condition is cast in the form of

$$\frac{\partial v^*}{\partial x^*} = 0 : \quad x^* = 0, \quad 0 \leq z^* \leq (1 + d^*) - R^* \quad (87)$$

The shear stress boundary condition is applied to the liquid vapor interface.

$$\mu\frac{\partial v}{\partial n} = \tau_{lv} : \quad 0 \leq x \leq w/2 + h\tan\theta, \quad z = (h + d) - \sqrt{R^2 - x^2} \quad (88)$$

Using the dimensionless variable definitions in eqns. (83) and (86) along with

$$n^* = \frac{n}{h} \quad (89)$$

the shear stress boundary condition is shown below in dimensionless form.

$$\frac{\partial v^*}{\partial n^*} = \tau_{lv}^* : \quad 0 \leq x^* \leq \beta + \tan\theta, \quad z^* = (1 + d^*) - \sqrt{R^{*2} - x^{*2}} \quad (90)$$

63

A.3 Equation of the meniscus for $\theta > 0$

As shown in Fig. 28(a), the equation of the circle which is symmetric about the z axis is given by

$$x^2 + (z - z_0)^2 = R^2 \tag{91}$$

where z_0 is the location of the center of the circle in the z direction.

$$z_0 = h + d$$

$$d = \sqrt{R^2 - \left(\frac{c}{2}\right)^2}$$

$$\frac{c}{2} = \frac{w}{2} + h \tan \theta \tag{92}$$

$$z_0 = h + \sqrt{R^2 - \left(\frac{w}{2} + h \tan \theta\right)^2}$$

Therefore, the equation of the liquid-vapor interface is

$$x^2 + \left\{ z - \left[h + \sqrt{R^2 - \left(\frac{w}{2} + h \tan \theta\right)^2} \right] \right\}^2 = R^2 \tag{93}$$

A relation must be found between the radius of curvature and the meniscus contact angle. At Point 2 shown in Fig. 28(b), the slope of the liquid-vapor interface is given by

$$\frac{dz}{dx} = \frac{(h - e)}{h \tan \theta} \tag{94}$$

The length of the line from Point 2 to Point 3 is

$$g = \sqrt{h^2 + h^2 \tan^2 \theta} = h\sqrt{1 + \tan^2 \theta} \tag{95}$$

Therefore, using the law of sines,

$$\frac{h\sqrt{1 + \tan^2 \theta}}{\sin \gamma} = \frac{e}{\sin \phi} \tag{96}$$

where

$$\theta + \gamma + \phi = \pi \tag{97}$$

64
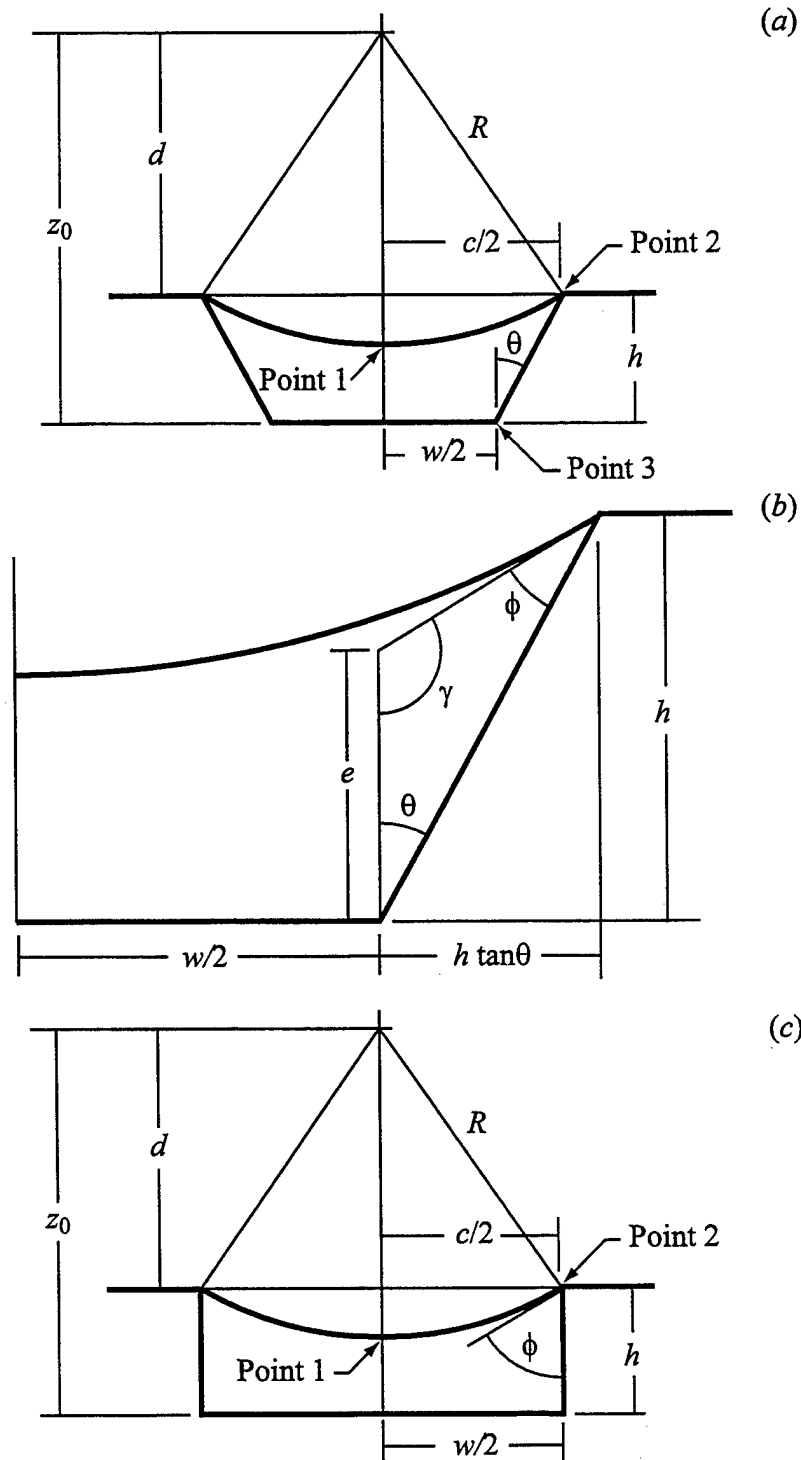
Figure 28: Determination of the equation of the circular liquid-vapor interface.

Combining the above two equations gives

$$e = h\sqrt{1 + \tan^2\theta}\left[\frac{\sin\phi}{\sin(\pi - \theta - \phi)}\right] \tag{98}$$

The slope of the liquid-vapor interface at Point 2 is

$$\left.\frac{dz}{dx}\right|_2 = \cot\theta - \sqrt{1 + \cot^2\theta}\left[\frac{\sin\phi}{\sin(\pi - \theta - \phi)}\right] \tag{99}$$

Taking the derivative of the liquid-vapor interface equation [eqn. (93)] with respect to x gives the slope at Point 2 in terms of the radius of curvature of the liquid-vapor interface

$$\left.\frac{dz}{dx}\right|_2 = \frac{\left(\dfrac{w}{2} + h\tan\theta\right)}{\sqrt{R^2 - \left(\dfrac{w}{2} + h\tan\theta\right)^2}} \tag{100}$$

Equating eqns. (99) and (100) gives the radius of curvature in terms of the meniscus contact angle.

$$R = \left(\frac{w}{2} + h\tan\theta\right)\sqrt{1 + \left\{\cot\theta - \sqrt{1 + \cot^2\theta}\left[\frac{\sin\phi}{\sin(\pi - \theta - \phi)}\right]\right\}^{-2}} \quad \text{for} \quad \theta > 0 \tag{101}$$

A.4 Equation of the meniscus for $\theta = 0$

For the case when the groove half-angle is zero [Fig. 28(c)], the equation of the circular arc simplifies to

$$x^2 + \left\{z - \left[h + \sqrt{R^2 - \left(\frac{w}{2}\right)^2}\right]\right\}^2 = R^2 \tag{102}$$

The slope of the curve at Point 2 is given in terms of the meniscus contact angle.

$$\left.\frac{dz}{dx}\right|_2 = \cot\phi \tag{103}$$

Differentiating eqn. (102) with respect to x gives and evaluating at Point 2 ($x = w/2$, $z = h$) gives

$$\left.\frac{dz}{dx}\right|_2 = \frac{\left(\dfrac{w}{2}\right)}{\sqrt{R^2 - \left(\dfrac{w}{2}\right)^2}} \tag{104}$$

66

Equating eqns. (103) and (104) gives the meniscus radius in terms of the contact angle.

$$R = \left(\frac{w}{2}\right)\sqrt{1 + \tan^2\phi} \tag{105}$$

A.5 Point of meniscus bifurcation for $\theta > 0$

The radius of curvature at bifurcation is given in terms of the geometry of the groove as

$$R_b = \frac{1}{2}\left[h + \frac{1}{h}\left(\frac{w}{2} + h\tan\theta\right)^2\right] \tag{106}$$

The equation of the circular arc for this case is given by

$$x^2 + (z - R_b)^2 = R_b^2 \tag{107}$$

The slope at Point 2 is given by eqn. (99). Differentiating eqn. (107) with respect to x gives

$$\left.\frac{dz}{dx}\right|_2 = \frac{\dfrac{w}{2} + h\tan\theta}{R_b - h} \tag{108}$$

Equating eqns. (99) and (108) gives

$$R_b = h + \left(\frac{w}{2} + h\tan\theta\right)\left\{\cot\theta - \sqrt{1 + \cot^2\theta}\left[\frac{\sin\phi_b}{\sin(\pi - \theta - \phi_b)}\right]\right\}^{-1} \tag{109}$$

The meniscus contact angle at bifurcation can be found as a function of the groove geometry by equating eqns. (106) and (109)

$$\phi_b = \tan^{-1}\left(\frac{1}{\sin\theta}\left\{\left[\cos\theta + \frac{2\sin\theta\,(\beta + \tan\theta)}{1 - (\beta + \tan\theta)^2}\right]^{-1} - \cos\theta\right\}\right)^{-1} \tag{110}$$

A.6 Point of meniscus bifurcation for $\theta = 0$

For the case when the half-angle is zero, the lower limit of recession is provided as follows. The equation of the circular arc is given by eqn. (107). The slope at Point 2 is shown in eqn. (103). The slope at Point 2 can also be found by differentiating eqn. (107) with respect to x and evaluating the result at Point 2.

$$\left.\frac{dz}{dx}\right|_2 = \frac{\dfrac{w}{2}}{R - h} \tag{111}$$

Equating eqns. (99) and (111) gives

$$R = h + \frac{w}{2}\tan\phi \tag{112}$$

A.7 Determination of the hydraulic diameter

In order to present the results of the computations in terms of the Reynolds number, the hydraulic diameter of the flow field must be found

$$D_h = \frac{4A_l}{P} \tag{113}$$

where A_l is the cross-sectional area, and P is the wetted perimeter.

$$P = w + 2h\sqrt{1 + \tan^2\theta} \tag{114}$$

The area of the liquid is found by subtracting the area of the segment of the circular arc from the trapezoidal groove area. The area of the trapezoid is

$$A_t = h\left(w + h\tan\theta\right) \tag{115}$$

The area of the circular segment is given by

$$A_s = R^2\cos^{-1}\left(\frac{d}{R}\right) - d\sqrt{R^2 - d^2} \tag{116}$$

where

$$d = \sqrt{R^2 - \left(\frac{c}{2}\right)^2} \tag{117}$$

$$\frac{c}{2} = \frac{w}{2} + h\tan\theta \tag{118}$$

$$d = \sqrt{R^2 - \left(\frac{w}{2} + h\tan\theta\right)^2} \tag{119}$$

$$d^2 = R^2 - \left(\frac{w}{2} + h\tan\theta\right)^2 \tag{120}$$

$$A_s = R^2\cos^{-1}\sqrt{1 - \frac{1}{R^2}\left(\frac{w}{2} + h\tan\theta\right)^2} - \left(\frac{w}{2} + h\tan\theta\right)\sqrt{R^2 - \left(\frac{w}{2} + h\tan\theta\right)^2} \tag{121}$$

The cross-sectional area of the fluid is given by

$$A_l = h \left(w + h \tan \theta \right) - R^2 \cos^{-1} \sqrt{1 - \frac{1}{R^2} \left(\frac{w}{2} + h \tan \theta \right)^2}$$
$$+ \left(\frac{w}{2} + h \tan \theta \right) \sqrt{R^2 - \left(\frac{w}{2} + h \tan \theta \right)^2} \tag{122}$$

The hydraulic diameter for the flow of liquid in a trapezoidal groove with a circular meniscus is

$$D_h = 4 \left\{ h \left(w + h \tan \theta \right) - R^2 \cos^{-1} \sqrt{1 - \left[\frac{1}{R} \left(\frac{w}{2} + h \tan \theta \right) \right]^2} \right.$$
$$\left. + R \left(\frac{w}{2} + h \tan \theta \right) \sqrt{1 - \left[\frac{1}{R} \left(\frac{w}{2} + h \tan \theta \right) \right]^2} \right\} \left(w + 2h \sqrt{1 + \tan^2 \theta} \right)^{-1} \tag{123}$$

A.8   Determination of the unit normal vector to the liquid-vapor interface

The unit normal vector to the liquid-vapor interface is related to the curvature vector by

$$\hat{n} = \frac{\vec{k}}{|\vec{k}|} \tag{124}$$

For $z = f(x)$, the curvature vector is

$$\vec{k} = \frac{z''}{\left[1 + (z')^2 \right]^2} \left(-z', 1 \right) \tag{125}$$

The magnitude of the curvature vector is given by

$$|\vec{k}| = \frac{|z''|}{\left[1 + (z')^2 \right]^{3/2}} \tag{126}$$

The functional form of the circular arc in terms of $z = f(x)$ is

$$z = z_0 \pm \sqrt{R^2 - x^2} \tag{127}$$

For the present analysis, the lower part of the circular arc is of interest. Therefore,

$$z = z_0 - \sqrt{R^2 - x^2} = z_0 - u^{1/2} \tag{128}$$

69

The first derivative of z with respect to x is

$$z' = xu^{-1/2} \qquad (129)$$

The second derivative of z is

$$z'' = x^2 u^{-3/2} + u^{-1/2} \qquad (130)$$

Substituting the above relations into eqn. (125) gives the curvature vector.

$$\vec{k} = u^{-1/2}\left(1 + x^2 u^{-1}\right)^{-1}\left(-xu^{-1/2}, 1\right) \qquad (131)$$

The magnitude of the curvature vector is

$$|\vec{k}| = \frac{|u^{-1/2}\left(x^2 u^{-1} + 1\right)|}{\left(1 + x^2 u^{-1}\right)^{3/2}} \qquad (132)$$

Since $u = R^2 - x^2 > 0$, the above equation reduces to

$$|\vec{k}| = u^{-1/2}\left(x^2 u^{-1} + 1\right)^{-1/2} \qquad (133)$$

The unit normal vector to the liquid-vapor interface is

$$\hat{n} = -\left(\frac{x}{R}\right)\hat{i} + \sqrt{1 - \left(\frac{x}{R}\right)^2}\,\hat{k} \qquad (134)$$

A.9   Derivation of the closed form solution for the capillary limit

The equation for the maximum capillary limit which includes the effects of interfacial shear stress and groove fill ratio is shown below for one helical groove.

$$\frac{\sigma}{R_c} \geq \frac{L_{\text{eff}}}{h_{\text{fg}}}\left\{ \frac{8\mu_v \dot{Q}_t}{\pi \rho_v R_v^4} + \left(\frac{\mu_l \dot{Q}_g}{h_l^2 v_0^* \rho_l A_l} - \frac{4\mu_v \dot{Q}_t}{\pi h_l R_v^3 \rho_v \tau_{lv,0}^*}\right)\sqrt{\left(\frac{2\pi R_h}{L_p}\right)^2 + 1}\right\}$$
$$- \rho_l\left[\int_0^{L_t}\hat{e}_{x_3}\cdot\left(-\vec{A} + \{-g\}\hat{e}_{z_1}\right)ds\right]\sqrt{\left(\frac{2\pi R_h}{L_p}\right)^2 + 1} \qquad (135)$$

Assuming no body forces, the previous equation reduces to

$$\frac{\sigma}{R_c} \geq \frac{L_{\text{eff}}}{h_{\text{fg}}}\left\{ \frac{8\mu_v \dot{Q}_t}{\pi \rho_v R_v^4} + \left(\frac{\mu_l \dot{Q}_g}{h_l^2 \overline{v_0^*}\rho_l A_l} - \frac{4\mu_v \dot{Q}_t}{\pi h_l R_v^3 \rho_v \tau_{lv,0}^*}\right)\sqrt{\left(\frac{2\pi R_h}{L_p}\right)^2 + 1}\right\} \qquad (136)$$

By allowing $L_p \to \infty$, which assumes the grooves are straight axial grooves rather than helical, eqn. (136) can be written as

$$\frac{\sigma}{R_c} \geq \frac{L_{\text{eff}}}{h_{\text{fg}}} \left(\frac{8\mu_v \dot{Q}_t}{\pi \rho_v R_v^4} + \frac{\mu_l \dot{Q}_g}{h_l^2 \overline{v_0^*} \rho_l A_l} - \frac{4\mu_v \dot{Q}_t}{\pi h_l R_v^3 \rho_v \tau_{lv,0}^*} \right) \tag{137}$$

Factoring terms on the right hand side of the equation gives

$$\frac{\sigma}{R_c} \geq \frac{L_{\text{eff}}}{h_{\text{fg}}} \left[\frac{\mu_l \dot{Q}_g}{h_l^2 \overline{v_0^*} \rho_l A_l} + \frac{8\mu_v \dot{Q}_t}{\pi \rho_v R_v^4} \left(1 - \frac{R_v}{2h_l \tau_{lv,0}^*} \right) \right] \tag{138}$$

The total heat transfered by the heat pipe is

$$\dot{Q}_t = \sum_{i=1}^{N_g} \dot{Q}_g \tag{139}$$

Assuming each groove transports the same amount of heat, eqn. (139) can be simplified to

$$\dot{Q}_g = \frac{\dot{Q}_t}{N_g} \tag{140}$$

Substituting this relationship into eqn. (138) gives

$$\frac{\sigma}{R_c} \geq \frac{L_{\text{eff}}}{h_{\text{fg}}} \left[\frac{\mu_l \dot{Q}_t}{N_g h_l^2 \overline{v_0^*} \rho_l A_l} + \frac{8\mu_v \dot{Q}_t}{\pi \rho_v R_v^4} \left(1 - \frac{R_v}{2h_l \tau_{lv,0}^*} \right) \right] \tag{141}$$

Solving for $\dot{Q}_t$, the resulting equation is the maximum capillary limit in a heat pipe acting with no body forces and straight axial grooves with the effects of interfacial shear stress and groove fill ratio.

$$\dot{Q}_{\text{cap}} = \frac{\sigma h_{\text{fg}}}{R_c L_{\text{eff}}} \left[\frac{\mu_l}{N_g h_l^2 \overline{v_0^*} \rho_l A_l} + \frac{8\mu_v}{\pi \rho_v R_v^4} \left(1 - \frac{R_v}{2h_l \tau_{lv,0}^*} \right) \right]^{-1} \tag{142}$$

B   Derivations of Selected Expressions for Sinusoidal Grooves

B.1   Determination of dimensionless Poisson equation

The governing equations of fully developed laminar flow reduce to the Poisson equation, as shown by White 1991.

$$\frac{\partial^2 v}{\partial x^2} + \frac{\partial^2 v}{\partial z^2} = \frac{1}{\mu}\frac{dp}{dy} \tag{143}$$

By substituting the following definitions for the dimensionless variables used in the analysis

$$v^* = \frac{\mu v}{h^2(-dp/dy)} \quad x^* = \frac{x}{h} \quad z^* = \frac{z}{h} \tag{144}$$

eqn. (143) can be rewritten as

$$\frac{\partial^2 v^*}{\partial x^{*2}} + \frac{\partial^2 v^*}{\partial z^{*2}} = -1 \tag{145}$$

B.2   Determination of dimensionless boundary conditions

Figure 22 shows liquid flow in a sinusoidal groove with the definitions of the dimensions used in the analysis. The no slip boundary condition is applied to the groove walls as shown below.

$$v = 0: \quad 0 \leq x \leq w_l/2, \quad z = \frac{h}{2}\left\{1 + \cos\left[-\pi\left(\frac{2x}{w_l h} + 1\right)\right]\right\} \tag{146}$$

Using the definitions of the following dimensionless parameters,

$$v^* = \frac{\mu v}{h^2(-dp/dy)} \quad x^* = \frac{x}{h} \quad z^* = \frac{z}{h} \quad \beta = \frac{w}{2h} \tag{147}$$

the dimensional no slip boundary condition can be written in dimensionless form as

$$v^* = 0: \quad 0 \leq x^* \leq w_l^*/2, \quad z^* = \frac{1}{2}\left\{1 + \cos\left[-\pi\left(\frac{x^*}{\beta} + 1\right)\right]\right\} \tag{148}$$

Along the centerline of the groove, the symmetry condition is used

$$\frac{\partial v}{\partial x} = 0: \quad x = 0, \quad 0 \leq z \leq h_l + R\sqrt{1 - \left(\frac{w_l}{2R}\right)^2} - R \tag{149}$$

Using the dimensionless parameters from eqn. (147) and noting that

$$R^* = \frac{R}{h} \quad d^* = \frac{d}{h} \tag{150}$$

the symmetry condition is cast in the form of

$$\frac{\partial v^*}{\partial x^*} = 0 : \quad x^* = 0, \quad 0 \leq z^* \leq h_l^* + R^* \sqrt{1 - \left(\frac{w_l^*}{2R^*}\right)^2} - R^* \tag{151}$$

The shear stress boundary condition is applied to the liquid vapor interface.

$$\frac{\partial v}{\partial n} = \tau_{lv} : \quad 0 \leq x \leq w_l/2, \quad z = h_l + R \sqrt{1 - \left(\frac{w_l}{2R}\right)^2} - \sqrt{R^2 - x^2} \tag{152}$$

Using the dimensionless variable definitions in eqns. (147) and (150) along with

$$n^* = \frac{n}{h} \tag{153}$$

the shear stress boundary condition is shown below in dimensionless form.

$$\frac{\partial v^*}{\partial n^*} = \tau_{lv}^* : \quad 0 \leq x^* \leq w_l^*/2, \quad z^* = h_l^* + R^* \sqrt{1 - \left(\frac{w_l^*}{2R^*}\right)^2} - \sqrt{R^{*2} - x^{*2}} \tag{154}$$

B.3 Equation of the meniscus

To determine the equation of the circular meniscus, a relationship must be made based on the slope of the tangent line at the sinusoidal groove wall, which is given by

$$\tan \psi = \left. \frac{dz^*}{dx^*} \right|_{\text{sine}} \tag{155}$$

The equation of the sinusoid for the groove wall is given by

$$z^* = \frac{1}{2} \left\{ 1 + \cos\left[-\pi \left(\frac{x^*}{\beta} + 1\right)\right] \right\} \tag{156}$$

Differentiating eqn. (156) with respect to x^* gives

$$\frac{dz^*}{dx^*} = \frac{\pi}{2\beta} \sin\left[-\pi \left(\frac{x^*}{\beta} + 1\right)\right] \tag{157}$$

Therefore, substituting eqn. (157) into eqn. (155) and evaluating $x^* = w_l^*/2$ results in the equation of the slope of the tangent line at the wall of the sinusoidal groove.

$$\tan \psi = \left. \frac{dz^*}{dx^*} \right|_{\text{sine}} = \frac{\pi}{2\beta} \sin\left[-\pi \left(\frac{w_l^*}{2\beta} + 1\right)\right] \tag{158}$$
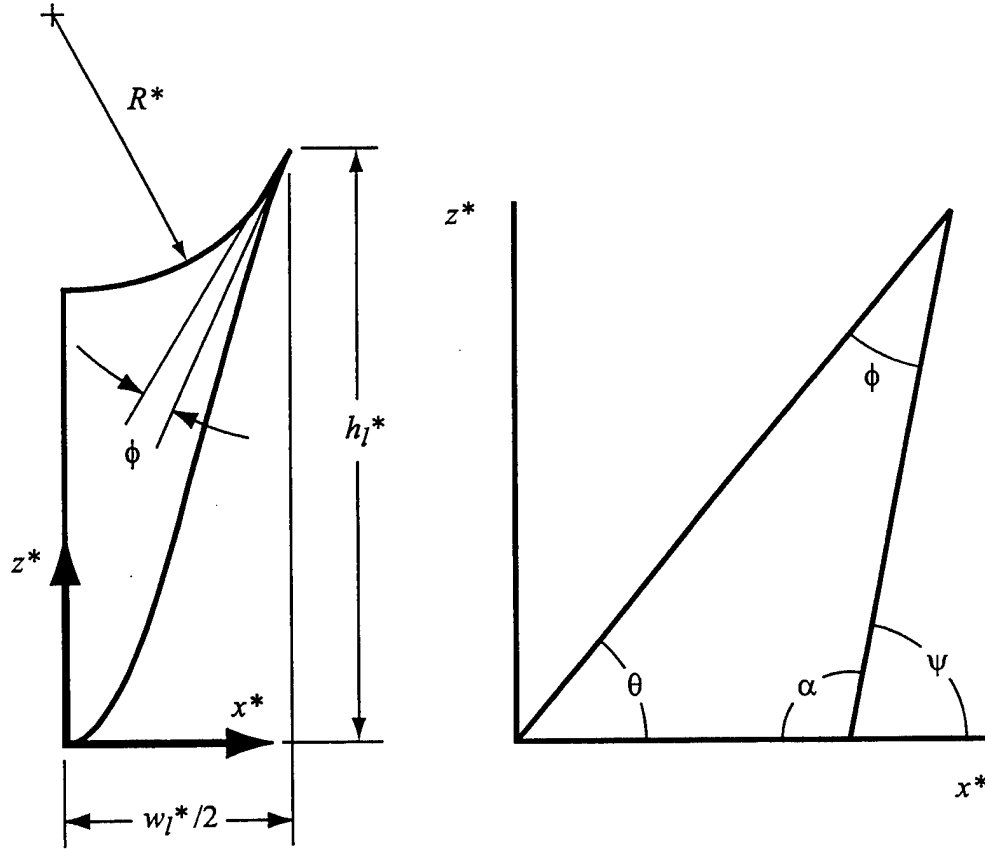
Figure 29: Definition of geometric parameters.

The slope of the tangent line on the circular meniscus is given by

$$\tan\theta = \left.\frac{dz^*}{dx^*}\right|_{circle} \tag{159}$$

From Fig. 29, the angle θ can be found as a function of angles α, ϕ, and ψ

$$\alpha = \pi - \psi \tag{160}$$

$$\theta + \phi + \alpha = \pi \tag{161}$$

$$\theta = \psi - \phi \tag{162}$$

Taking the tangent of both sides of eqn. (162) and using the trigonometric addition formula for tangent gives

$$\tan\theta = \tan(\psi - \phi) \tag{163}$$

$$\tan(\alpha \pm \beta) = \frac{\tan\alpha \pm \tan\beta}{1 \mp \tan\alpha\tan\beta} \tag{164}$$

$$\tan\theta = \frac{\tan\psi - \tan\phi}{1 + \tan\psi\tan\phi} \tag{165}$$

The general equation for a circle with the z^* axis as a line of symmetry is

$$x^{*2} + (z^* - z_o^*)^2 = R^{*2} \tag{166}$$

Taking the derivative of eqn. (166) with respect to x^* gives

$$2x^* + 2(z^* - z_o^*)\frac{dz^*}{dx^*} = 0 \tag{167}$$

Rearranging eqn. (167) to solve for dz^*/dx^* gives

$$\frac{dz^*}{dx^*} = -\frac{x^*}{(z^* - z_o^*)} \tag{168}$$

By substituting $x^* = w_l^*/2$ and $z^* = h_l^*$ into eqn. (168) and then substituting the result into eqn. (159) gives the slope of the tangent line on the circular meniscus

$$\left.\frac{dz^*}{dx^*}\right|_{circle} = -\frac{w_l^*/2}{(h_l^* - z_o^*)} = \tan\theta \tag{169}$$

Combining eqns. (165) and (169) gives

$$-\frac{w_l^*/2}{(h_l^* - z_o^*)} = \frac{\tan\psi - \tan\phi}{1 + \tan\psi\tan\phi} \tag{170}$$

Rearranging eqn. (170) to solve for z_o^* gives

$$z_o^* = h_l^* + \frac{\left(\dfrac{w_l^*}{2}\right)(1 + \tan\psi\tan\phi)}{\tan\psi - \tan\phi} \tag{171}$$

where z_o^* is the height of the center of the circle on the z^* axis. By letting d be the distance between the center of the circular liquid-vapor interface and the height of the liquid, it can be shown that

$$z_o^* = h_l^* + d \tag{172}$$

$$d = \sqrt{R^{*2} - \left(\frac{c}{2}\right)^2} \tag{173}$$

$$\frac{c}{2} = \frac{w_l^*}{2} \tag{174}$$

$$z_o^* = h_l^* + \sqrt{R^{*2} - \left(\frac{w_l^*}{2}\right)^2} \tag{175}$$

Combining eqns. (171) and (175) gives

$$\sqrt{R^{*2} - \left(\frac{w_l^*}{2}\right)^2} = \frac{\left(\frac{w_l^*}{2}\right)(1 + \tan\psi \tan\phi)}{\tan\psi - \tan\phi} \tag{176}$$

$$R^{*2} - \left(\frac{w_l^*}{2}\right)^2 = \left[\frac{\left(\frac{w_l^*}{2}\right)(1 + \tan\psi \tan\phi)}{\tan\psi - \tan\phi}\right]^2 \tag{177}$$

$$\frac{\left(\frac{w_l^*}{2}\right)}{\sqrt{R^{*2} - \left(\frac{w_l^*}{2}\right)^2}} = \frac{d^* - \tan\phi}{1 + d^* \tan\phi} \tag{178}$$

where

$$d^* = \tan\psi = \frac{\pi}{2\beta} \sin\left[-\pi\left(\frac{w_l^*}{2\beta} + 1\right)\right] \tag{179}$$

$$\sqrt{R^{*2} - \left(\frac{w_l^*}{2}\right)^2} = \frac{\left(\frac{w_l^*}{2}\right)(1 + d^* \tan\phi)}{d^* - \tan\phi} \tag{180}$$

$$R^{*2} - \left(\frac{w_l^*}{2}\right)^2 = \frac{\left(\frac{w_l^*}{2}\right)^2 (1 + d^* \tan\phi)^2}{(d^* - \tan\phi)^2} \tag{181}$$

$$R^{*2} = \left(\frac{w_l^*}{2}\right)^2 \left[1 + \frac{(1 + d^* \tan\phi)^2}{(d^* - \tan\phi)^2)}\right] \tag{182}$$

The equation of the radius of curvature of the meniscus in terms of meniscus contact angle is

$$R^* = \left(\frac{w_l^*}{2}\right)\left[1 + \frac{(1 + d^* \tan\phi)^2}{(d^* - \tan\phi)^2)}\right]^{\frac{1}{2}} \tag{183}$$

76
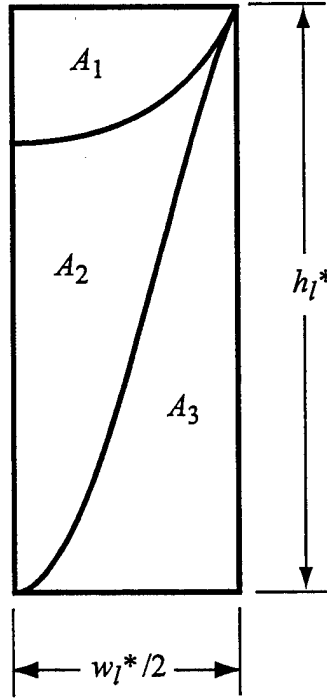
Figure 30: Determination of the cross-sectional area of the liquid.

B.4 Determination of the maximum meniscus contact angle

The maximum meniscus contact angle can be found when $R^* \to \infty$ in eqn. (183). It can be seen that $R^* \to \infty$ as $(d^* - \tan \phi) \to 0$. Therefore

$$d^* - \tan \phi_{\max} = 0 \tag{184}$$

Substituting eqn. (184) into eqn. (179) for d^* results in

$$\frac{\pi}{2\beta} \sin \left[-\pi \left(\frac{w_l^*}{2\beta} + 1 \right) \right] - \tan \phi_{\max} = 0 \tag{185}$$

Solving for $\phi_{\max}$ gives the equation for the maximum meniscus contact angle.

$$\phi_{\max} = \tan^{-1} \left\{ \frac{\pi}{2\beta} \sin \left[-\pi \left(\frac{w_l^*}{2\beta} + 1 \right) \right] \right\} \tag{186}$$

B.5 Determination of the hydraulic diameter

The hydraulic diameter of the flow field must be determined so that the Poiseuille number can be calculated. To find $D_h^* = 4A_l^*/P^*$, it can be shown from Fig. 30 that

$$A_1 + A_2 + A_3 = \frac{1}{2} w_l^* h_l^* \tag{187}$$

77

$$A_2 = \frac{A_l^*}{2} = \frac{1}{2} w_l^* h_l^* - A_1 - A_3 \tag{188}$$

The area A_3 can be found by integrating the equation for the sinusoidal groove wall, eqn. (156) over $0 \leq x^* \leq w_l^*/2$.

$$A_3 = \int_0^{w_l^*/2} \frac{1}{2} \left\{ 1 + \cos \left[-\pi \left(\frac{x^*}{\beta} + 1 \right) \right] \right\} dx^* \tag{189}$$

$$A_3 = \frac{w_l^*}{4} - \frac{\beta}{2\pi} \sin \left[-\pi \left(\frac{w_l^*}{2\beta} + 1 \right) \right] \tag{190}$$

From Fig. 30, A_1 is the area above the meniscus. It can be shown that A_1 is one-half of the area of the segment

$$A_1 = \frac{R^{*2}}{2} \cos^{-1} \left(\frac{d}{R^*} \right) - d\sqrt{R^{*2} - d^2} \tag{191}$$

where

$$d = \sqrt{R^{*2} - \left(\frac{w_l^*}{2} \right)^2} \tag{192}$$

Thus, the area A_1 is

$$A_1 = \frac{R^*}{2} \left[R^* \cos^{-1} \sqrt{1 - \left(\frac{w_l^*}{2R^*} \right)^2} - \left(\frac{w_l^*}{2} \right) \sqrt{1 - \left(\frac{w_l^*}{2R^*} \right)^2} \right] \tag{193}$$

Substituting eqns. (190) and (193) into eqn. (188) gives the cross-sectional area of the flow field

$$A_l^* = \frac{w_l^*}{2} (2h_l^* - 1) - R^* \left[R^* \cos^{-1} \sqrt{1 - \left(\frac{w_l^*}{2R^*} \right)^2} - \left(\frac{w_l^*}{2} \right) \sqrt{1 - \left(\frac{w_l^*}{2R^*} \right)^2} \right]$$
$$+ \frac{\beta}{\pi} \sin \left[-\pi \left(\frac{w_l^*}{2\beta} + 1 \right) \right] \quad \text{for} \quad \phi < \phi_{\max} \tag{194}$$

When the meniscus contact angle approaches the maximum value $\phi \to \phi_{\max}$, the area $A_1 \to 0$. Therefore, the cross-sectional area of the flow field for this case is

$$A_l^* = w_l^* h_l^* - 2A_3 \tag{195}$$

$$A_l^* = w_l^* h_l^* - \frac{w_l^*}{2} + \frac{\beta}{\pi} \sin \left[-\pi \left(\frac{w_l^*}{2\beta} + 1 \right) \right] \tag{196}$$

78

$$A_l^* = \frac{w_l^*}{2} \left(2h_l^* - 1 \right) + \frac{\beta}{\pi} \sin \left[-\pi \left(\frac{w_l^*}{2\beta} + 1 \right) \right] \quad \text{for} \quad \phi = \phi_{\text{max}} \qquad (197)$$

In order to determine the wetted perimeter, the following formula will be used to find the arc length of the groove wall

$$P^* = \int_{x_1}^{x_2} \sqrt{1 + (y')^2} \, dx \quad \text{for} \quad y = f(x)$$

$$P^* = 2 \int_0^{w_l^*/2} \sqrt{1 + \left(\left. \frac{dz^*}{dx^*} \right|_{\text{sine}} \right)^2} \, dx^* \qquad (198)$$

where

$$\left. \frac{dz^*}{dx^*} \right|_{\text{sine}} = \frac{\pi}{2\beta} \sin \left[-\pi \left(\frac{x^*}{\beta} + 1 \right) \right] \qquad (199)$$

Thus, the arc length can be found by substituting eqn. (199) into eqn. (198)

$$P^* = 2 \int_0^{w_l^*/2} \sqrt{1 + \left(\frac{\pi}{2\beta} \right)^2 \sin^2 \left[-\pi \left(\frac{x^*}{\beta} + 1 \right) \right]} \, dx^* \qquad (200)$$

The equation for the wetted perimeter has no closed-form solution, and consequently the equation for the hydraulic diameter has no closed-form solution. The reason is that the integral in eqn. (200) is elliptic, and must be solved numerically.
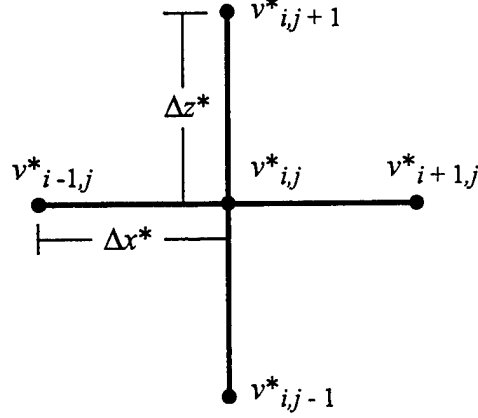
Figure 31: Computational molecule using a central differencing scheme.

C Numerical Code Validation (Trapezoidal Grooves)

The elliptic Poisson equation given in eqn. (3) with mixed boundary conditions [eqns. (4), (5) and (8)] was solved using Gauss-Seidel iteration with successive over-relaxation and a central differencing scheme (Burden and Faires, 1985). The computational molecule is shown in Fig. 31. The second-order central differences in the x^* and z^* directions are

$$\frac{\partial^2 v^*}{\partial x^{*2}} \simeq \frac{v^*_{i+1,j} - 2v^*_{i,j} + v^*_{i-1,j}}{(\Delta x^*)^2} \tag{201}$$

$$\frac{\partial^2 v^*}{\partial z^{*2}} \simeq \frac{v^*_{i,j+1} - 2v^*_{i,j} + v^*_{i,j-1}}{(\Delta z^*)^2} \tag{202}$$

Substituting eqns. (201) and (202) into eqn. (3) gives the following finite difference equation

$$v^{*(k)}_{i,j} = \left[\frac{2}{(\Delta x^*)^2} + \frac{2}{(\Delta z^*)^2} \right]^{-1} \left\{ 1 + \frac{1}{(\Delta x^*)^2} \left(v^{*(k-1)}_{i+1,j} + v^{*(k-1)}_{i-1,j} \right) \right. \tag{203}$$
$$\left. + \frac{1}{(\Delta z^*)^2} \left(v^{*(k-1)}_{i,j+1} + v^{*(k)}_{i,j-1} \right) \right\}$$

where $(k-1)$ signifies the solution field from the previous iteration. Successive over-relaxation was implemented using the following relation

$$v^{*(k)}_{i,j} = v^{*(k-1)}_{i,j} + \omega \left(v^{*(k)}_{i,j} - v^{*(k-1)}_{i,j} \right) \tag{204}$$

80

where $1 \leq \omega \leq 2$. For the present problem, a value of $\omega = 1.3$ optimized the convergence of the solution. Due to the nature of the rectangular grid used to solve eqn. (203), the shear stress boundary condition at the liquid-vapor interface given by eqn. (8) was approximated as follows.

$$\frac{\partial v^*}{\partial n^*} \simeq \frac{\partial v^*}{\partial z^*} = \tau_{lv}^* \tag{205}$$

Discretizing this equation gives the dimensionless velocity at the liquid-vapor interface.

$$v_{i,j}^{*(k)} = v_{i,j-1}^{*(k)} + \tau_{lv}^* \, \Delta z^* \tag{206}$$

The solution procedure was as follows:

1. Set all parameters.

2. Compute the radius of curvature, area and hydraulic diameter of the flow field.

3. Calculate the grid sizes and locate the grid points.

4. Locate the circular liquid-vapor interface and the side wall of the groove.

5. Set the initial velocity field to zero.

6. Begin iterating.

7. Calculate the updated velocity field away from the boundaries using eqns. (203) and (204).

8. Apply the symmetry boundary condition at $x^* = 0$.

9. Apply the shear stress condition at the liquid-vapor interface using eqn. (206).

10. Set the velocity to zero above the meniscus.

11. Calculate the difference between the previous solution and the most recent solution at every grid point.

(a) If the maximum difference is greater than the convergence criterion ϵ, then place the most recent values into the previous solution and continue to iterate.

(b) If the maximum difference is less than the convergence criterion, then calculate the average velocity, Poiseuille number, and volumetric flow rate and print the results.

The convergence criteria for the iterative solution was set to $\epsilon = 10^{-8}$ for each case. A grid independence check was made in which the number of grids in each direction was doubled. When the value for the Poiseuille number did not change by more than 3%, grid independence was considered to be reached. The convergence criteria was then reduced by an order of magnitude while maintaining the highest number of grids. If the Poiseuille number did not change by more than 2%, the solution was considered to be independent of both grid size and ϵ. Otherwise, a grid independence check was made at the smaller value of ϵ until a converged solution was reached. In all of the results reported, grid independence and the convergence criteria were less than 1% unless otherwise noted.

The numerical model was tested against several existing solutions, such as rectangular ducts, triangular grooves without interfacial shear stress, and rectangular and triangular grooves with shear stress at the liquid-vapor interface.

Shah (1974) determined the friction factors for the laminar flow within ducts of various cross sections using a least-squares-matching technique. For trapezoidal ducts, the area and hydraulic diameter are given by

$$A^* = 2\beta + \tan\theta \tag{207}$$

$$D_h^* = \frac{2(2\beta + \tan\theta)}{2\beta + \tan\theta + \sec\theta} \tag{208}$$

Figure 32 and Table 4 show the comparison of the Poiseuille number between the present solution and those given by Shah (1975) and Shah and London (1978) for laminar flow in a family of trapezoidal ducts. The agreement is excellent, with a

82
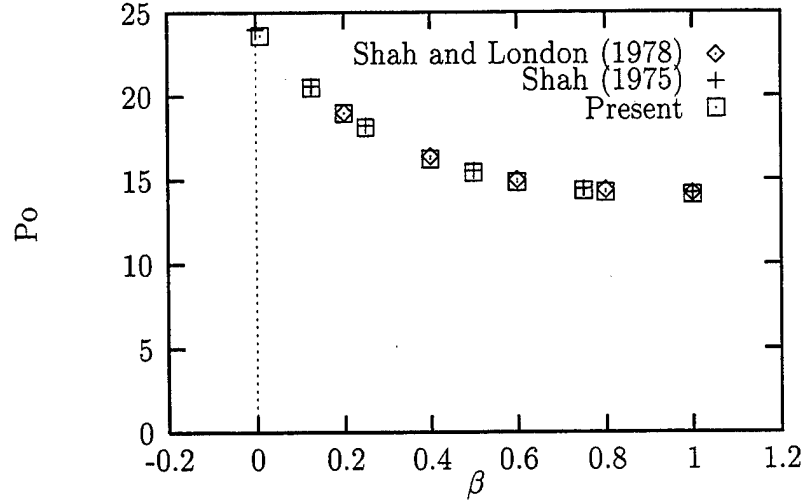
Figure 32: Po versus β for laminar flow in a rectangular duct.

maximum difference of 0.9%. While Shah provided a Poiseuille number at $\beta = 0$, this could not be obtained with the present numerical solution technique because the area of the computational domain approached zero as $\beta \to 0$. As a result, a data point is shown at $\beta = 0.01$.

Ayyaswamy et al. (1974) presented the friction factors obtained for laminar flow in triangular grooves using the Galerkin method of solution. Romero and Yost (1996) presented the following equation for the dimensionless volumetric flow rate in a triangular groove

$$\Gamma(\phi, \alpha) \approx \Gamma(\alpha, \alpha) \left(h_c^*(\phi, \alpha) \right)^3 \left(\frac{A^*(\phi, \alpha)}{\cot \alpha} \right)^{1/2} \qquad (209)$$

where $\alpha = \pi/2 - \theta$ is the angle from the side of the groove to horizontal, and $\Gamma(\alpha, \alpha)$ was approximated using asymptotic methods and a regression analysis.

$$\Gamma(\alpha, \alpha) \approx \frac{1}{6} \left(\frac{\cot^3 \alpha + 3.4 \cot^4 \alpha + \cot^5 \alpha}{1 + 3.4 \cot \alpha + 4 \cot^2 \alpha + 3.4 \cot^3 \alpha + \cot^4 \alpha} \right) \qquad (210)$$

The dimensionless height of the liquid at the line of symmetry of the groove is

$$h_c^* = 1 + \frac{\cot \alpha \cos(\alpha - \phi) - 1}{\sin(\alpha - \phi)} \qquad (211)$$

The dimensionless cross-sectional area of the liquid in the groove is

$$A^*(\phi, \alpha) = \frac{2 \left[\sin^2(\alpha - \phi) \tan \alpha - (\alpha - \phi) + \sin(\alpha - \phi) \cos(\alpha - \phi) \right]}{\tan^2 \alpha \sin^2(\alpha - \phi)} \qquad (212)$$

83

Table 4: Poiseuille number versus rectangular duct aspect ratio: Comparison of the present solution with that given by Shah (1975) and Shah and London (1978).

	Poiseuille Number, Po		
β	Shah (1975)	Shah and London (1978)	Present
0.0	24.000		
0.01			23.619
0.125	20.585		20.486
0.2		19.07050	18.958
0.25	18.233		18.116
0.4		16.36810	16.246
0.5	15.548		15.424
0.6		14.97996	14.856
0.75	14.476		14.352
0.8		14.37780	14.255
1.0	14.227	14.22708	14.104

For comparison with the present results, the Poiseuille number in terms of the dimensionless volumetric flow rate is

$$\text{Po} = \frac{D_h^{*2} A^*}{2\Gamma(\phi, \alpha)} \qquad (213)$$

Kolodziej et al. (1999) used the boundary collocation method to solve the same problem, except that the liquid-vapor interface was not assumed to be circular. For comparison, the case where Bo = 0.001 was examined. Figure 33 and Table 5 present the solutions obtained by Ayyaswamy et al. for $\theta = 5°$ and $60°$ for the full range of meniscus contact angle ($0.1° \leq \phi \leq \theta + \phi = 90°$). While the agreement is excellent for $\theta = 60°$, it is less so for $\theta = 5°$. This is due to the extreme narrowness of the flow field for this case. The maximum percent differences for $\theta = 5°$ and $60°$ are 3.7% and 0.9%, respectively. Figure 33 and Table 5 also show a comparison of the present results with those of Romero and Yost (1996). The maximum percent differences are 2.2% for $\theta = 5°$ and 2.3% for $\theta = 60°$. Also shown in Fig. 33 and Table 5 are the results of Kolodziej et al. for the lowest value of Bond number presented (Bo = 0.001), which should correspond to the present case. The agreement with the Kolodziej et al. data is less satisfactory, with a maximum percent difference of 4.5% for $\theta = 5°$, and 19.9% for $\theta = 60°$. This may be due to the approximate nature of the solution
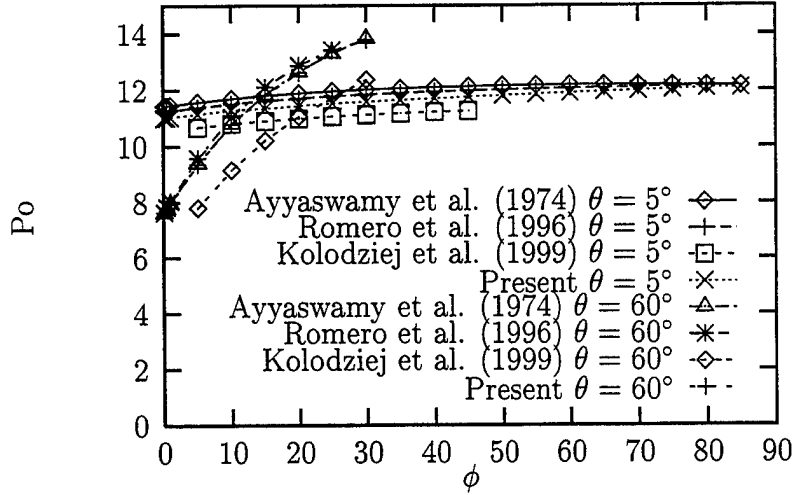
Figure 33: Po versus ϕ for laminar flow in a triangular groove without shear at the meniscus ($\beta = 0$, $\tau_{lv}^* = 0$).

by Kolodziej et al., which was in terms of a truncated infinite summation.

DiCola (1968) presented the solution for the Poiseuille number for the laminar flow of a constant property fluid within a rectangular groove. While interfacial shear stress at the liquid-vapor interface was accounted for, the groove was assumed to be completely full, with a meniscus contact angle of $\phi = 90°$. The analytical solution was obtained using separation of variables. Schneider and DeVos (1980) presented the following equation which was attributed to DiCola (1968):

$$(f\text{Re})_l = \frac{24\left\{1 + \dfrac{\tau^* w^2}{12\delta^2}\left[1 - \dfrac{96}{\pi^4}\sum_{n=0}^{\infty}\dfrac{1}{(2n+1)^4}\operatorname{sech}\dfrac{(2n+1)\pi\delta}{w}\right]\right\}}{\left(1 + \dfrac{w}{2\delta}\right)^2\left[1 - \dfrac{96w}{\pi^5\delta}\sum_{n=0}^{\infty}\dfrac{1}{(2n+1)^5}\tanh\dfrac{(2n+1)\pi\delta}{w}\right]} \tag{214}$$

where the dimensionless shear stress at the liquid-vapor interface is given by

$$\tau^* = \frac{\delta\tau_v}{\mu_l\overline{v_l}} \tag{215}$$

The groove width and depth are w and δ, respectively, τ_v is the shear stress on the vapor at the liquid-vapor interface, μ_l is the absolute viscosity of the liquid, and $\overline{v_l}$ is

Table 5: Poiseuille number versus meniscus contact angle for triangular grooves with no shear at the liquid-vapor interface ($\beta = 0$, $\tau_{lv}^* = 0$): Comparison of the present solution with those given by Ayyaswamy et al. (1974), Romero and Yost (1996) and Kolodziej et al. (1999).

	Poiseuille Number, Po							
	Ayyaswamy et al.		Romero and Yost		Kolodziej et al.		Present	
ϕ	$\theta = 5°$	$\theta = 60°$	$\theta = 5°$	$\theta = 60°$	$\theta = 5°$	$\theta = 60°$	$\theta = 5°$	$\theta = 60°$
0.1°	11.422	7.612	11.234	7.645			11.008	7.545
0.5	11.436	7.767	11.248	7.826			11.015	7.728
1	11.452	7.963	11.265	8.046			11.033	7.966
5	11.573	9.403	11.386	9.586	10.682	7.808	11.149	9.365
10	11.699	10.803	11.513	11.040	10.803	9.158	11.291	10.789
15	11.801	11.841	11.618	12.093	10.904	10.215	11.366	11.812
20	11.884	12.642	11.704	12.857	10.988	11.061	11.446	12.606
25	11.952	13.288	11.777	13.413	11.059	N/A	11.519	13.397
30	12.007	13.828	11.837		11.120	12.352	11.581	13.770
35	12.052		11.888		11.171		11.641	
40	12.089		11.931		11.214		11.697	
45	12.117		11.968		11.252		11.750	
50	12.139		11.999				11.799	
55	12.155		12.026				11.843	
60	12.166		12.050				11.887	
65	12.171		12.071				11.929	
70	12.171		12.090				11.969	
75	12.166		12.108				12.009	
80	12.156		12.124				12.053	
85	12.140						12.063	
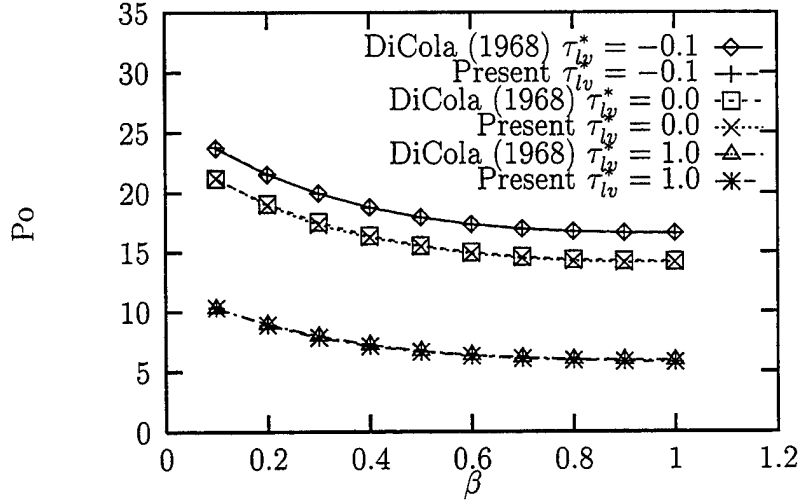
Figure 34: Po versus β for laminar flow in a full rectangular groove with shear at the meniscus ($\phi = 90°$, $\theta = 0°$).

the mean liquid velocity. The DiCola equation can be rewritten as

$$
\text{Po} = \frac{24 \left\{ 1 - \frac{\tau_{lv}^* \beta^2}{3\overline{v^*}} \left[1 - \frac{96}{\pi^4} \sum_{n=0}^{\infty} \frac{1}{(2n+1)^4} \operatorname{sech} \frac{(2n+1)\pi}{2\beta} \right] \right\}}{(1+\beta)^2 \left[1 - \frac{192\beta}{\pi^5} \sum_{n=0}^{\infty} \frac{1}{(2n+1)^5} \tanh \frac{(2n+1)\pi}{2\beta} \right]}
\tag{216}
$$

A negative sign has been introduced to account for the fact that the shear stress on the vapor is in the opposite direction compared to that on the liquid. The comparison between the above equation and the results of the present analysis are shown in Fig. 34 and Table 6 for laminar flow in a family of rectangular grooves at the full groove condition ($\phi = 90°$, $0.1 \leq \beta \leq 1.0$, $\tau_{lv}^* = -0.1$, 0.0, and 1.0). The comparison is excellent with a maximum percent difference of 2.3%.

The results of the present model were compared to the correlation presented by Lin and Faghri (1997), where the friction factor for the flow of liquid in triangular grooves was presented as follows:

$$
f_l = \frac{13.163}{\text{Re}_l} + 0.6211\tau_v^*
\tag{217}
$$

where $\tau_v^* = \tau_v / \rho_l \overline{v_l}^2$ is the dimensionless interfacial shear stress. The prediction errors for this equation were between -2.8% and 1.3%. Casting this equation in terms of

87

Table 6: Poiseuille number versus rectangular groove aspect ratio for several values of dimensionless shear stress at the liquid-vapor interface ($\phi = 90°$, $\theta = 0°$): Comparison of the present solution with that given by DiCola (1968).

	Poiseuille Number, Po					
	DiCola (1968)			Present		
β	$\tau_{lv}^* = 0.0$	$\tau_{lv}^* = 1.0$	$\tau_{lv}^* = -0.1$	$\tau_{lv}^* = 0.0$	$\tau_{lv}^* = 1.0$	$\tau_{lv}^* = -0.1$
0.1	21.168	10.300	23.708	21.199	10.183	23.788
0.2	19.070	8.9579	21.535	18.952	8.8446	21.557
0.3	17.512	7.9693	19.945	17.309	7.8205	19.940
0.4	16.368	7.2283	18.776	16.219	7.1135	18.740
0.5	15.548	6.7168	17.934	15.460	6.6213	17.891
0.6	14.979	6.3590	17.349	14.874	6.2958	17.303
0.7	14.605	6.1419	16.966	14.485	6.0661	16.920
0.8	14.377	5.9964	16.738	14.245	5.9265	16.693
0.9	14.260	5.9513	16.630	14.117	5.8172	16.586
1.0	14.227	5.9070	16.612	14.158	5.7804	16.570

the dimensionless quantities used in the present analysis gives

$$\text{Po} = 13.163 + 0.6211 \left(\frac{D_h^* \tau_{lv}^*}{\overline{v}^*} \right) \tag{218}$$

Figure 35 and Table 7 show the comparison of the regression equation and the results of the present analysis for countercurrent flow. Unfortunately, not enough information was provided by Lin and Faghri (1997) to precisely determine the limits of applicability for eqn. (217). Therefore, the equation was evaluated over a fairly large range for comparison with the present solution. The agreement is quite good between $0.075 \le -\tau_{lv}^* \le 0.1$, where the maximum percent difference in this range is 2.2%.
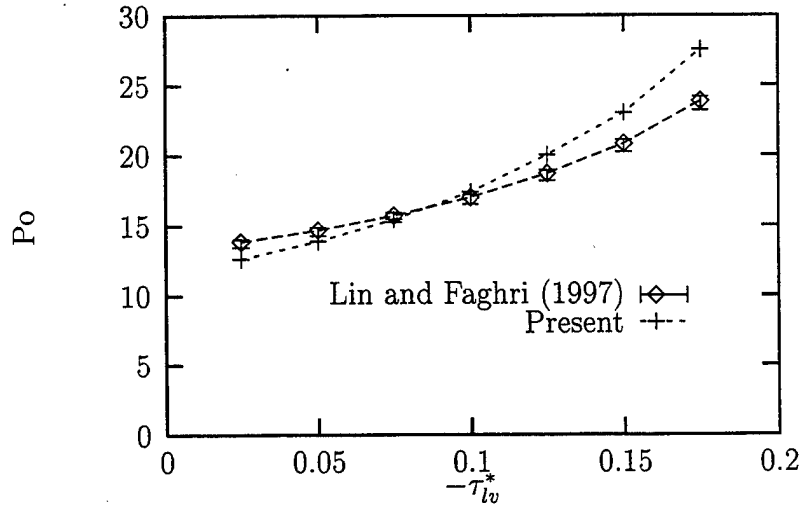
Figure 35: Po versus $-\tau_{lv}^*$ for laminar countercurrent flow in a triangular groove ($\beta = 0$, $\phi = 30°$, $\theta = 20°$).

Table 7: Poiseuille number versus dimensionless shear stress at the liquid-vapor interface for countercurrent flow ($\beta = 0$, $\phi = 30°$, $\theta = 20°$): Comparison of the present solution with that given by Lin and Faghri (1997).

	Poiseuille Number, Po	
$-\tau_{lv}^*$	Lin and Faghri (1997)	Present
0.025	13.862	12.607
0.050	14.703	13.885
0.075	15.733	15.451
0.100	17.026	17.415
0.125	18.716	20.030
0.150	20.818	23.008
0.175	23.850	27.533

D Tables of Results

In all of the results reported, grid independence and the convergence criteria were less than 1% unless otherwise noted.

Table 8: Mean velocity versus shear stress at the liquid-vapor interface for various values of meniscus contact angle ($\beta = 1.0$, $\theta = 0°$).

τ_{lv}^*	$\overline{v^*}$			
	$\phi = 0°$	$\phi = 30°$	$\phi = 60°$	$\phi = 90°$
-0.45	—	—	—	0.49199E-1
-0.40	—	—	—	0.59164E-1
-0.35	—	—	0.32345E-1	0.69436E-1
-0.30	—	—	0.42262E-1	0.79708E-1
-0.25	—	—	0.55480E-1	0.89940E-1
-0.20	—	0.20770E-1	0.60834E-1	0.10024
-0.15	—	0.28109E-1	0.70127E-1	0.11052
-0.10	0.32991E-2*	0.35399E-1	0.78213E-1	0.12070
-0.05	0.51296E-2	0.42230E-1	0.88438E-1	0.13106
0.0	0.69877E-2	0.49638E-1	0.97783E-1	0.14126
0.125	0.11598E-1†	0.68289E-1	0.12099	0.16701
0.25	0.18327E-1	0.86652E-1	0.14465	0.19269
0.375	0.23781E-1	0.10501	0.16832	0.21837
0.5	0.29235E-1	0.12338	0.19198	0.24405
0.625	0.34690E-1	0.14174	0.21563	0.26835
0.75	0.40144E-1	0.16010	0.23930	0.29383
0.875	0.45598E-1	0.17847	0.26295	0.31932
1.0	0.51053E-1	0.19683	0.28468	0.34959
1.5	0.72870E-1	0.27029	0.37813	0.44674
2.0	0.94087E-1	0.34375	0.47158	0.54870
3.0	0.13832	0.49066	0.65514	0.75258
4.0	0.18195	0.63757	0.84087	0.95644
5.0	0.22559	0.78448	1.0265	1.1603

* Grid independence: 2.2%
† Grid independence: 1.5%

Table 9: Poiseuille number versus shear stress at the liquid-vapor interface for various values of meniscus contact angle ($\beta = 1.0$, $\theta = 0°$).

	Po			
τ_{lv}^*	$\phi = 0°$	$\phi = 30°$	$\phi = 60°$	$\phi = 90°$
-0.45	—	—	—	40.605
-0.40	—	—	—	33.803
-0.35	—	—	40.137	28.803
-0.30	—	—	30.719	25.091
-0.25	—	—	25.185	22.236
-0.20	—	33.313	21.341	19.950
-0.15	—	24.615	18.514	18.096
-0.10	27.918*	19.546	16.414	16.570
-0.05	17.907	16.384	14.680	15.259
0.0	13.181	13.939	13.277	14.158
0.125	7.9414†	10.132	10.730	11.974
0.25	5.0257	7.9851	8.9752	10.378
0.375	3.8730	6.5888	7.7129	9.1589
0.5	3.1505	5.6081	6.7624	8.1947
0.625	2.6551	4.8816	6.0208	7.4528
0.75	2.2944	4.3217	5.4251	6.8064
0.875	2.0199	3.8770	4.9372	6.2632
1.0	1.8041	3.5153	4.5603	5.7804
1.5	1.2639	2.5598	3.4333	4.4767
2.0	0.97275	2.0128	2.7530	3.6449
3.0	0.66589	1.4102	1.9816	2.6575
4.0	0.50620	1.0852	1.5439	2.0910
5.0	0.40829	0.88203	1.2646	1.7236

* Grid independence: 2.2%
† Grid independence: 1.5%

Table 10: Volumetric flow rate versus shear stress at the liquid-vapor interface for various values of meniscus contact angle ($\beta = 1.0$, $\theta = 0°$).

τ_{lv}^*	V^*			
	$\phi = 0°$	$\phi = 30°$	$\phi = 60°$	$\phi = 90°$
-0.45	—	—	—	0.98398E-1
-0.40	—	—	—	0.11832
-0.35	—	—	0.52969E-1	0.13887
-0.30	—	—	0.69210E-1	0.15941
-0.25	—	—	0.90857E-1	0.17988
-0.20	—	0.24531E-1	0.99625E-1	0.20048
-0.15	—	0.33199E-1	0.11484	0.22104
-0.10	0.14160E-2*	0.41809E-1	0.12808	0.24140
-0.05	0.22016E-2	0.49877E-1	0.14483	0.26212
0.0	0.29991E-2	0.58626E-1	0.16013	0.28252
0.125	0.49780E-2†	0.80339E-1	0.19813	0.33402
0.25	0.78660E-2	0.10193	0.23688	0.38538
0.375	0.10270E-1	0.12353	0.27565	0.43674
0.5	0.12548E-1	0.14514	0.31439	0.48810
0.625	0.14889E-1	0.16674	0.35312	0.53670
0.75	0.17230E-1	0.18834	0.39189	0.58766
0.875	0.19571E-1	0.20995	0.43062	0.63864
1.0	0.21912E-1	0.23155	0.46620	0.69918
1.5	0.31276E-1	0.31923	0.61924	0.89348
2.0	0.40640E-1	0.40599	0.77228	1.0974
3.0	0.59368E-1	0.57951	1.0728	1.5051
4.0	0.78096E-1	0.75302	1.3770	1.9128
5.0	0.96824E-1	0.92653	1.6810	2.3206

* Grid independence: 2.2%
† Grid independence: 1.5%

Table 11: Mean velocity versus shear stress at the liquid-vapor interface for various values of meniscus contact angle ($\beta = 1.0$, $\theta = 30°$).

τ_{lv}^*	$\overline{v^*}$			
	$\phi = 0°$	$\phi = 20°$	$\phi = 40°$	$\phi = 60°$
-0.375	—	—	—	0.74804E-1
-0.3125	—	—	0.41206E-1	0.93526E-1
-0.25	—	—	0.56119E-1	0.11224
-0.1875	—	0.21137E-1	0.71387E-1	0.13096
-0.125	—	0.32001E-1	0.86165E-1	0.14969
-0.0625	0.57800E-2	0.42814E-1	0.10150	0.16841
0.0	0.11068E-1	0.53861E-1	0.11664	0.18713
0.125	0.21608E-1	0.74276E-1	0.14770	0.22457
0.25	0.32361E-1	0.97689E-1	0.17876	0.26202
0.375	0.43114E-1	0.12013	0.20982	0.29946
0.5	0.53599E-1	0.14258	0.23959	0.33509
0.625	0.64249E-1	0.16503	0.27028	0.37225
0.75	0.74898E-1	0.18748	0.30097	0.40941
0.875	0.85547E-1	0.20993	0.33165	0.44657
1.0	0.96197E-1	0.23119	0.36234	0.48374
1.5	0.13879	0.32003	0.48508	0.63238
2.0	0.18139	0.40887	0.60782	0.78103
3.0	0.26658	0.58655	0.85008	1.0783
4.0	0.35177	0.76423	1.0943	1.3756
5.0	0.43697	0.94191	1.3386	1.6723

Table 12: Poiseuille number versus shear stress at the liquid-vapor interface for various values of meniscus contact angle ($\beta = 1.0$, $\theta = 30°$).

τ_{lv}^*	Po			
	$\phi = 0°$	$\phi = 20°$	$\phi = 40°$	$\phi = 60°$
-0.375	—	—	—	38.253
-0.3125	—	—	41.349	30.629
-0.25	—	—	30.361	25.493
-0.1875	—	36.513	23.867	21.849
-0.125	—	24.117	19.774	19.116
-0.0625	21.721	18.026	16.785	16.991
0.0	11.343	14.329	14.607	15.291
0.125	5.8103	10.390	11.535	12.741
0.25	3.8797	7.9005	9.5312	10.921
0.375	2.9121	6.4246	8.1203	9.5556
0.5	2.3424	5.4127	7.1112	8.5395
0.625	1.9541	4.6764	6.3039	7.6870
0.75	1.6763	4.1165	5.6611	6.9893
0.875	1.4676	3.6763	5.1374	6.4077
1.0	1.3051	3.3383	4.7023	5.9154
1.5	0.90460	2.4116	3.5124	4.5250
2.0	0.69217	1.8876	2.8031	3.6638
3.0	0.47096	1.3158	2.0043	2.6537
4.0	0.35691	1.0098	1.5569	2.0802
5.0	0.28732	0.81939	1.2727	1.7105

Table 13: Volumetric flow rate versus shear stress at the liquid-vapor interface for various values of meniscus contact angle ($\beta = 1.0$, $\theta = 30°$).

τ_{lv}^*	V^*			
	$\phi = 0°$	$\phi = 20°$	$\phi = 40°$	$\phi = 60°$
-0.375	—	—	—	0.19279
-0.3125	—	—	0.81949E-1	0.24104
-0.25	—	—	0.14197	0.28928
-0.1875	—	0.28292E-1	0.11160	0.33752
-0.125	—	0.42833E-1	0.17136	0.38580
-0.0625	0.32234E-2	0.57307E-1	0.20186	0.43405
0.0	0.59752E-2	0.72093E-1	0.23197	0.48229
0.125	0.11665E-1	0.99419E-1	0.29374	0.57879
0.25	0.17470E-1	0.13075	0.35551	0.67531
0.375	0.23275E-1	0.16079	0.41728	0.77181
0.5	0.28936E-1	0.19084	0.47651	0.86364
0.625	0.34685E-1	0.22089	0.53753	0.95941
0.75	0.40434E-1	0.25094	0.59856	1.0551
0.875	0.46183E-1	0.28099	0.65959	1.1509
1.0	0.51933E-1	0.30945	0.72062	1.2467
1.5	0.75025E-1	0.42836	0.96473	1.6298
2.0	0.97926E-1	0.54727	1.2088	2.0129
3.0	0.14391	0.78510	1.6906	2.7791
4.0	0.18990	1.0229	2.1763	3.5454
5.0	0.23590	1.2607	2.6621	4.3101

Table 14: Mean velocity versus shear stress at the liquid-vapor interface for various values of meniscus contact angle ($\beta = 1.0$, $\theta = 60°$).

	$\overline{v^*}$			
τ_{lv}^*	$\phi = 0°$	$\phi = 10°$	$\phi = 20°$	$\phi = 30°$
-0.375	—	—	—	0.75897E-1
-0.3125	—	—	0.41983E-1	0.98354E-1
-0.25	—	—	0.59724E-1	0.12081
-0.1875	—	0.28621E-1	0.77466E-1	0.14326
-0.125	0.73396E-2*	0.41509E-1	0.94812E-1	0.16572
-0.0625	0.14995E-1†	0.54181E-1	0.11263	0.18818
0.0	0.22642E-1	0.66951E-1	0.13046	0.21107
0.125	0.37623E-1	0.92099E-1	0.16100	0.25554
0.25	0.53077E-1	0.11829	0.20175	0.30046
0.375	0.68746E-1	0.14448	0.23768	0.34537
0.5	0.84415E-1	0.17067	0.27364	0.39028
0.625	0.10008	0.19648	0.30959	0.43296
0.75	0.11477	0.22243	0.34554	0.47756
0.875	0.13205	0.24839	0.38149	0.52217
1.0	0.14776	0.27435	0.41744	0.56677
1.5	0.20674	0.37816	0.56125	0.74520
2.0	0.26815	0.48199	0.70506	0.92361
3.0	0.39098	0.68963	0.99268	1.2804
4.0	0.51380	0.89727	1.2802	1.6372
5.0	0.63663	1.1049	1.5679	1.9941

* Grid independence: 2.6%
† Grid independence: 1.1%

Table 15: Poiseuille number versus shear stress at the liquid-vapor interface for various values of meniscus contact angle ($\beta = 1.0$, $\theta = 60°$).

	Po			
τ_{lv}^*	$\phi = 0°$	$\phi = 10°$	$\phi = 20°$	$\phi = 30°$
-0.375	—	—	—	40.780
-0.3125	—	—	43.296	31.469
-0.25	—	—	30.434	25.619
-0.1875	—	30.202	23.464	21.604
-0.125	31.963*	20.699	19.171	18.676
-0.0625	15.644†	15.858	16.138	16.447
0.0	10.361	12.833	13.932	14.663
0.125	6.2354	9.3294	10.943	12.111
0.25	4.4199	7.2637	9.0097	10.301
0.375	3.4125	5.9470	7.6474	8.9617
0.5	2.7791	5.0344	6.6426	7.9304
0.625	2.3440	4.3730	5.8712	7.1487
0.75	2.0440	3.8627	5.2604	6.4810
0.875	1.8017	3.4591	4.7646	5.9274
1.0	1.6108	3.1318	4.3543	5.4609
1.5	1.1347	2.2720	3.2386	4.1534
2.0	0.87487	1.7826	2.5780	3.3526
3.0	0.60003	1.2459	1.8311	2.4172
4.0	0.45659	0.95760	1.4197	1.8904
5.0	0.36850	0.77764	1.1593	1.5521

* Grid independence: 2.6%
† Grid independence: 1.1%

Table 16: Volumetric flow rate versus shear stress at the liquid-vapor interface for various values of meniscus contact angle ($\beta = 1.0$, $\theta = 60°$).

τ_{lv}^*	V^*			
	$\phi = 0°$	$\phi = 10°$	$\phi = 20°$	$\phi = 30°$
-0.375	—	—	—	0.28325
-0.3125	—	—	0.12007	0.36706
-0.25	—	—	0.17081	0.45086
-0.1875	—	0.56279E-1	0.22155	0.53465
-0.125	0.75407E-2*	0.81621E-1	0.27116	0.61847
-0.0625	0.15405E-1†	0.10651	0.32212	0.70229
0.0	0.23264E-1	0.13164	0.37311	0.78772
0.125	0.38656E-1	0.18109	0.46046	0.95368
0.25	0.54535E-1	0.23260	0.57700	1.1213
0.375	0.70634E-1	0.28409	0.67976	1.2889
0.5	0.86734E-1	0.33559	0.78261	1.4565
0.625	0.10282	0.38635	0.88543	1.6158
0.75	0.11792	0.43739	0.98825	1.7822
0.875	0.13567	0.48843	1.0910	1.9487
1.0	0.15181	0.53947	1.1940	2.1152
1.5	0.21242	0.74359	1.6051	2.7811
2.0	0.27551	0.94776	2.0164	3.4469
3.0	0.40172	1.3560	2.8390	4.7785
4.0	0.52791	1.7643	3.6613	6.1101
5.0	0.65412	2.1726	4.4842	7.4420

* Grid independence: 2.6%
† Grid independence: 1.1%

Table 17: Mean velocity versus shear stress at the liquid-vapor interface for various values of groove aspect ratio ($\phi = 30°$, $\theta = 0°$).

τ_{lv}^*	$\overline{v}^*$		
	$\beta = 0.5$	$\beta = 1.0$	$\beta = 1.5$
-0.375	0.14752E-1*	—	—
-0.3125	0.19853E-1**	—	—
-0.25	0.25245E-1	—	—
-0.1875	0.30603E-1	0.22287E-1††	—
-0.125	0.35952E-1	0.31469E-1**	0.12684E-1‡
-0.0625	0.41301E-1	0.40743E-1	0.19402E-1
0.0	0.45883E-1	0.49638E-1	0.26119E-1
0.125	0.56930E-1	0.68289E-1	0.39552E-1
0.25	0.67443E-1	0.86652E-1	0.52986E-1
0.375	0.77955E-1	0.10501	0.66420E-1
0.5	0.88468E-1	0.12338	0.79853E-1
0.625	0.98981E-1	0.14174	0.93287E-1
0.75	0.10949	0.16010	0.10672
0.875	0.12047	0.17847	0.12015
1.0	0.13102	0.19683	0.13358
1.5	0.17326	0.27029	0.18732
2.0	0.21545†	0.34375	0.24105
3.0	0.30005†	0.49066	0.34852
4.0	0.38444**	0.63757	0.45599
5.0	0.46891**	0.78448	0.56346

* Grid independence: 2.2%

** Grid independence: 1.2%

† Grid independence: 1.1%

†† Grid independence: 2.0%

‡ Grid independence: 2.3%

Table 18: Poiseuille number versus shear stress at the liquid-vapor interface for various values of groove aspect ratio ($\phi = 30°$, $\theta = 0°$).

τ_{lv}^*	Po $\beta = 0.5$	$\beta = 1.0$	$\beta = 1.5$
-0.375	38.108*	—	—
-0.3125	28.317**	—	—
-0.25	22.260	—	—
-0.1875	18.370	31.045††	—
-0.125	15.636	21.987**	33.179‡
-0.0625	13.611	16.982	21.692
0.0	11.976	13.939	16.114
0.125	9.8457	10.132	10.641
0.25	8.3110	7.9851	7.9434
0.375	7.1902	6.5888	6.3368
0.5	6.3358	5.6081	5.2707
0.625	5.6629	4.8816	4.5117
0.75	5.1192	4.3217	3.9438
0.875	4.6665	3.8770	3.5029
1.0	4.2905	3.5153	3.1506
1.5	3.2446	2.5598	2.2468
2.0	2.6093†	2.0128	1.7460
3.0	1.8736†	1.4102	1.2076
4.0	1.4623**	1.0852	0.92301
5.0	1.1989**	0.88203	0.74697

* Grid independence: 2.2%
** Grid independence: 1.2%
† Grid independence: 1.1%
†† Grid independence: 2.0%
‡ Grid independence: 2.3%

Table 19: Volumetric flow rate versus shear stress at the liquid-vapor interface for various values of groove aspect ratio ($\phi = 30°$, $\theta = 0°$).

τ_{lv}^*	V^*		
	$\beta = 0.5$	$\beta = 1.0$	$\beta = 1.5$
-0.375	0.11731E-1*	—	—
-0.3125	0.15788E-1**	—	—
-0.25	0.20084E-1	—	—
-0.1875	0.24337E-1	0.26218E-1††	—
-0.125	0.28591E-1	0.37020E-1**	0.14548E-1‡
-0.0625	0.32845E-1	0.47929E-1	0.22456E-1
0.0	0.36076E-1	0.58626E-1	0.29954E-1
0.125	0.45208E-1	0.80339E-1	0.45361E-1
0.25	0.53556E-1	0.10193	0.60767E-1
0.375	0.61904E-1	0.12353	0.76174E-1
0.5	0.70252E-1	0.14514	0.91580E-1
0.625	0.78600E-1	0.16674	0.10698
0.75	0.86948E-1	0.18834	0.12239
0.875	0.95806E-1	0.20995	0.13780
1.0	0.10420	0.23155	0.15320
1.5	0.13779	0.31923	0.21483
2.0	0.17134†	0.40599	0.27645
3.0	0.23862†	0.57951	0.39971
4.0	0.30573**	0.75302	0.52296
5.0	0.37291**	0.92653	0.64621

* Grid independence: 2.2%
** Grid independence: 1.2%
† Grid independence: 1.1%
†† Grid independence: 2.0%
‡ Grid independence: 2.3%

101

Table 20: Mean velocity versus shear stress at the liquid-vapor interface for various values of groove aspect ratio ($\phi = 30°$, $\theta = 30°$).

τ_{lv}^*	$\overline{v^*}$			
	$\beta = 0.0$	$\beta = 0.5$	$\beta = 1.0$	$\beta = 1.5$
-0.25	—	0.33511E-1	0.31252E-1	—
-0.1875	0.10930E-1	0.44442E-1	0.44545E-1	0.30859E-1*
-0.125	0.15939E-1	0.55373E-1	0.57663E-1	0.43708E-1†
-0.0625	0.21027E-1	0.66304E-1	0.70993E-1	0.56557E-1
0.0	0.26234E-1	0.77458E-1	0.83936E-1	0.68965E-1
0.125	0.36293E-1	0.99459E-1	0.11017	0.94766E-1
0.25	0.46235E-1	0.12154	0.13723	0.12056
0.375	0.56325E-1	0.14362	0.16429	0.14636
0.5	0.66416E-1	0.16468	0.19135	0.17216
0.625	0.76507E-1	0.18654	0.21841	0.19796
0.75	0.86598E-1	0.20840	0.24547	0.22376
0.875	0.96689E-1	0.23026	0.27253	0.24956
1.0	0.10678	0.25212	0.29959	0.27537
1.5	0.14714	0.33957	0.40545	0.37857
2.0	0.18750	0.42702	0.51262	0.48177
3.0	0.26823	0.60191	0.72697	0.68818
4.0	0.34896	0.77680	0.94131	0.89458
5.0	0.42968	0.95170	1.1556	1.1009

* Grid independence: 1.9%
† Grid independence: 1.3%

Table 21: Poiseuille number versus shear stress at the liquid-vapor interface for various values of groove aspect ratio ($\phi = 30°$, $\theta = 30°$).

	Po			
τ_{lv}^*	$\beta = 0.0$	$\beta = 0.5$	$\beta = 1.0$	$\beta = 1.5$
-0.25	—	29.167	38.710	—
-0.1875	28.606	21.993	27.158	37.289*
-0.125	19.617	17.651	20.980	26.327†
-0.0625	14.869	14.741	17.040	20.346
0.0	11.918	12.618	14.413	16.686
0.125	8.6153	9.8276	10.980	12.143
0.25	6.7628	8.0422	8.8153	9.5446
0.375	5.5513	6.8057	7.3635	7.8621
0.5	4.7078	5.9353	6.3222	6.6839
0.625	4.0869	5.2398	5.5390	5.8126
0.75	3.6107	4.6901	4.9284	5.1426
0.875	3.2338	4.2448	4.4391	4.6109
1.0	2.9282	3.8767	4.0381	4.1789
1.5	2.1250	2.8784	2.9838	3.0397
2.0	1.6675	2.2889	2.3600	2.3885
3.0	1.1657	1.6239	1.6641	1.6721
4.0	0.89603	1.2582	1.2852	1.2863
5.0	0.72769	1.0270	1.0468	1.0452

* Grid independence: 1.9%

† Grid independence: 1.3%

Table 22: Volumetric flow rate versus shear stress at the liquid-vapor interface for various values of groove aspect ratio ($\phi = 30°$, $\theta = 30°$).

τ_{lv}^*	V^*			
	$\beta = 0.0$	$\beta = 0.5$	$\beta = 1.0$	$\beta = 1.5$
-0.25	—	0.38764E-1	0.52371E-1	—
-0.1875	0.49904E-2	0.51410E-1	0.74649E-1	0.62142E-1*
-0.125	0.72773E-2	0.64055E-1	0.96632E-1	0.88016E-1†
-0.0625	0.96006E-2	0.76699E-1	0.11897	0.11389
0.0	0.11977E-1	0.89602E-1	0.14066	0.13887
0.125	0.16570E-1	0.11505	0.18464	0.19083
0.25	0.21109E-1	0.14059	0.22998	0.24278
0.375	0.25716E-1	0.16613	0.27532	0.29472
0.5	0.30323E-1	0.19050	0.32066	0.34668
0.625	0.34931E-1	0.21578	0.36602	0.39846
0.75	0.39538E-1	0.24106	0.41136	0.45060
0.875	0.44145E-1	0.26636	0.45670	0.50245
1.0	0.48752E-1	0.29164	0.50206	0.55450
1.5	0.67181E-1	0.39280	0.67946	0.76232
2.0	0.85609E-1	0.49396	0.85906	0.97014
3.0	0.12246	0.69628	1.2182	1.3857
4.0	0.15932	0.89859	1.5774	1.8014
5.0	0.19618	1.1009	1.9366	2.2170

* Grid independence: 1.9%
† Grid independence: 1.3%

104

Table 23: Mean velocity versus shear stress at the liquid-vapor interface for various values of groove aspect ratio ($\phi = 30°$, $\theta = 60°$).

	$\overline{v^*}$			
τ_{lv}^*	$\beta = 0.0$	$\beta = 0.5$	$\beta = 1.0$	$\beta = 1.5$
-0.375	—	0.53334E-1	0.75897E-1	0.90127E-1
-0.3125	0.33653E-1	0.72695E-1	0.98354E-1	0.11443
-0.25	0.48754E-1	0.92056E-1	0.12081	0.13874
-0.1875	0.63856E-1	0.11141	0.14326	0.16306
-0.125	0.78957E-1	0.13077	0.16572	0.18737
-0.0625	0.94058E-1	0.15013	0.18818	0.21168
0.0	0.10915	0.17030	0.21107	0.23708
0.125	0.13936	0.20824	0.25554	0.28461
0.25	0.16956	0.24694	0.30046	0.33324
0.375	0.19976	0.28566	0.34537	0.38185
0.5	0.22996	0.32438	0.39028	0.43047
0.625	0.26017	0.36311	0.43296	0.47910
0.75	0.29037	0.40183	0.47756	0.52772
0.875	0.32057	0.44055	0.52217	0.57634
1.0	0.35080	0.47927	0.56677	0.62496
1.5	0.47161	0.63416	0.74520	0.81945
2.0	0.58941	0.78905	0.92361	1.0088
3.0	0.82971	1.0988	1.2804	1.3955
4.0	1.0700	1.4086	1.6372	1.7821
5.0	1.3103	1.7183	1.9941	2.1688

Table 24: Poiseuille number versus shear stress at the liquid-vapor interface for various values of groove aspect ratio ($\phi = 30°$, $\theta = 60°$).

τ_{lv}^*	Po			
	$\beta = 0.0$	$\beta = 0.5$	$\beta = 1.0$	$\beta = 1.5$
-0.375	—	44.783	40.780	40.563
-0.3125	44.571	32.856	31.469	31.946
-0.25	30.766	25.946	25.619	26.348
-0.1875	23.490	21.437	21.604	22.420
-0.125	18.997	18.263	18.676	19.511
-0.0625	15.947	15.908	16.447	17.270
0.0	13.741	14.025	14.663	15.419
0.125	10.763	11.469	12.111	12.845
0.25	8.8461	9.6722	10.301	10.970
0.375	7.5087	8.3612	8.9617	9.5739
0.5	6.5225	7.3631	7.9304	8.4926
0.625	5.7654	6.5779	7.1487	7.6307
0.75	5.1657	5.9440	6.4810	6.9276
0.875	4.6790	5.4216	5.9274	6.3432
1.0	4.2758	4.9835	5.4609	5.8497
1.5	3.1805	3.7663	4.1534	4.4613
2.0	2.5448	3.0270	3.3526	3.6239
3.0	1.8078	2.1736	2.4172	2.6197
4.0	1.4018	1.6956	1.8904	2.0513
5.0	1.1447	1.3899	1.5521	1.6856

Table 25: Volumetric flow rate versus shear stress at the liquid-vapor interface for various values of groove aspect ratio ($\phi = 30°$, $\theta = 60°$).

τ_{lv}^*	V^*			
	$\beta = 0.0$	$\beta = 0.5$	$\beta = 1.0$	$\beta = 1.5$
-0.375	—	0.14571	0.28325	0.42648
-0.3125	0.58288E-1	0.19860	0.36706	0.54152
-0.25	0.84444E-1	0.25150	0.45086	0.65656
-0.1875	0.11060	0.30439	0.53465	0.77160
-0.125	0.13675	0.35729	0.61847	0.88664
-0.0625	0.16291	0.41018	0.70229	1.0016
0.0	0.18907	0.46526	0.78772	1.1219
0.125	0.24138	0.56892	0.95368	1.3468
0.25	0.29368	0.67466	1.1213	1.5769
0.375	0.34600	0.78045	1.2889	1.8069
0.5	0.39830	0.88624	1.4565	2.0370
0.625	0.45062	0.99203	1.6158	2.2670
0.75	0.50294	1.0978	1.7822	2.4972
0.875	0.55524	1.2036	1.9487	2.7272
1.0	0.60760	1.3094	2.1152	2.9573
1.5	0.81686	1.7325	2.7811	3.8776
2.0	1.0208	2.1557	3.4469	4.7737
3.0	1.4370	3.0020	4.7785	6.6035
4.0	1.8532	3.8483	6.1101	8.4334
5.0	2.2695	4.6947	7.4420	10.263

Table 26: Liquid-vapor shear stress when the mean velocity is zero versus meniscus contact angle for $\beta = 1.0$.

| | $-\tau^*_{lv,0}$ | | | | | |
| | Analytical | | | Numerical | | |
ϕ	$\theta = 0°$	$\theta = 30°$	$\theta = 60°$	$\theta = 0°$	$\theta = 30°$	$\theta = 60°$
0°	0.13662	0.14152	0.17957	0.16743	0.12910	0.18826
10°	—	—	0.35260	—	—	0.32225
20°	—	0.39066	0.52077	—	0.30236	0.45252
30°	0.48838	—	0.68301	0.33968	—	0.59013
40°	—	0.61770	—	—	0.48096	—
60°	0.78192	0.81699	—	0.53204	0.62874	—
90°	1.0000	—	—	0.69298	—	—

Table 27: Liquid-vapor shear stress when the mean velocity is zero versus groove aspect ratio for $\phi = 30°$.

| | $-\tau^*_{lv,0}$ | | | | | |
| | Analytical | | | Numerical | | |
β	$\theta = 0°$	$\theta = 30°$	$\theta = 60°$	$\theta = 0°$	$\theta = 30°$	$\theta = 60°$
0	—	0.37758	0.50000	—	0.32342	0.45198
0.5	0.65768	0.51267	0.61200	0.54363	0.44253	0.54762
1	0.48838	0.50727	0.68301	0.33968	0.39337	0.59013
1.5	0.31907	0.46283	0.73205	0.24279	0.33430	0.61283

Table 28: Mean velocity, Poiseuille number and volumetric flow rate versus groove half-angle ($\phi = 30.0°$, $\tau_{lv}^* = 5.0$).

β	θ	$\overline{v^*}$	Po	V^*
0.0	15°	0.15039	0.63916	0.34134E-1
0.0	30°	0.42968	0.72769	0.19618
0.0	45°	0.77729	0.87321	0.64037
0.0	60°	1.3103	1.1447	2.2695
0.5	0°	0.46840*	1.2002*	0.37250*
0.5	15°	0.72524	1.0147	0.88294
0.5	30°	0.95170	1.0270	1.1009
0.5	45°	1.2307	1.1405	1.9737
0.5	60°	1.7183	1.3899	4.6947
1.0	0°	0.78448	0.88203	0.92653
1.0	15°	0.95403	0.92271	1.2882
1.0	30°	1.1556	1.0468	1.9366
1.0	45°	1.4570	1.2408	3.3446
1.0	60°	1.9941	1.5521	7.4420
1.5	0°	0.56346	0.74697	0.64621
1.5	15°	0.83014	0.82527	1.2318
1.5	30°	1.1009	1.0452	2.2170
1.5	45°	1.15058	1.3144	4.3656
1.5	60°	2.1688	1.6856	10.263

* Grid independence: 1.9%

Table 29: Mean velocity, Poiseuille number and volumetric flow rate versus groove half-angle ($\beta = 1.0$, $\tau_{lv}^* = 5.0$).

ϕ	θ	$\overline{v^*}$	Po	V^*
0°	0°	0.22559	0.40829	0.96824E-1
0°	15°	0.35819	0.26472	0.15874
0°	30°	0.43697	0.28732	0.23590
0°	45°	0.51700	0.34103	0.37059
0°	60°	0.63663	0.36850	0.65412
10°	0°	0.41271*	0.65741*	0.30402*
10°	15°	0.56551†	0.54255†	0.45080†
10°	30°	0.69597	0.57652	0.67168
10°	45°	0.85547	0.66278	1.0996
10°	60°	1.1049	0.77764	2.1726
20°	0°	0.63489	0.75699	0.62239
20°	15°	0.79550	0.72604	0.87007
20°	30°	0.94191	0.81939	1.2607
20°	45°	1.1689	0.95753	2.1112
20°	60°	1.5679	1.1593	4.4842
30°	0°	0.78448	0.88203	0.92653
30°	15°	0.95512	0.92166	1.2896
30°	30°	1.1556	1.0468	1.9366
30°	45°	1.4570	1.2408	3.3446
30°	60°	1.9941	1.5521	7.4420
40°	0°	0.91623	0.99751	1.2387
40°	15°	1.0914	1.1027	1.7231
40°	30°	1.3386	1.2727	2.6621
40°	45°	1.7251	1.5229	4.7736
50°	0°	0.98256	1.1480	1.4758
50°	15°	1.2066	1.2793	2.1575
50°	30°	1.5161	1.4856	3.4670
60°	0°	1.0265	1.2646	1.6810
60°	15°	1.3069	1.4552	2.5940
60°	30°	1.6723	1.7105	4.3101

* Grid independence: 1.5%
† Grid independence: 1.7%

110

Table 30: Geometric values for the parametric analysis to determine the volumetric flow rate versus groove fill ratio ($h = 3.831 \times 10^{-4}$ m, $w = 3.445 \times 10^{-4}$ m, $\phi_0 = 7.0°$, $A_g = 1.703 \times 10^{-7}$ m^2).

β	θ	ϕ	h_l (m)	w_l (m)	R (m)	A_l (m^2)	A_l/A_g
0.0	52.31°	7.0°	1.653×10^{-5}	4.279×10^{-5}	4.192×10^{-5}	3.674×10^{-10}	0.00216
0.0	52.31°	7.0°	3.401×10^{-5}	8.804×10^{-5}	8.625×10^{-5}	1.555×10^{-9}	0.00913
0.0	52.31°	7.0°	5.140×10^{-5}	1.331×10^{-4}	1.303×10^{-4}	3.552×10^{-9}	0.02086
0.0	52.31°	7.0°	6.879×10^{-5}	1.781×10^{-4}	1.744×10^{-4}	6.362×10^{-9}	0.03737
1.049	14.62°	7.0°	1.642×10^{-4}	4.302×10^{-4}	2.314×10^{-4}	1.805×10^{-8}	0.10603
0.8991	14.62°	7.0°	1.916×10^{-4}	4.445×10^{-4}	2.390×10^{-4}	2.696×10^{-8}	0.15833
0.7868	14.62°	7.0°	2.189×10^{-4}	4.587×10^{-4}	2.467×10^{-4}	3.612×10^{-8}	0.21214
0.6993	14.62°	7.0°	2.463×10^{-4}	4.730×10^{-4}	2.544×10^{-4}	4.561×10^{-8}	0.26785
0.6294	14.62°	7.0°	2.737×10^{-4}	4.873×10^{-4}	2.621×10^{-4}	5.538×10^{-8}	0.32528
0.5722	14.62°	7.0°	3.010×10^{-4}	5.015×10^{-4}	2.697×10^{-4}	6.541×10^{-8}	0.38419
0.5245	14.62°	7.0°	3.284×10^{-4}	5.158×10^{-4}	2.774×10^{-4}	7.577×10^{-8}	0.44503
0.4841	14.62°	7.0°	3.558×10^{-4}	5.301×10^{-4}	2.851×10^{-4}	8.642×10^{-8}	0.50757
0.4496	14.62°	7.0°	3.831×10^{-4}	5.444×10^{-4}	2.928×10^{-4}	9.732×10^{-8}	0.57159
0.4496	14.62°	15.0°	3.831×10^{-4}	5.444×10^{-4}	3.131×10^{-4}	1.091×10^{-7}	0.64063
0.4496	14.62°	25.0°	3.831×10^{-4}	5.444×10^{-4}	3.534×10^{-4}	1.218×10^{-7}	0.71541
0.4496	14.62°	35.0°	3.831×10^{-4}	5.444×10^{-4}	4.201×10^{-4}	1.330×10^{-7}	0.78100
0.4496	14.62°	45.0°	3.831×10^{-4}	5.444×10^{-4}	5.382×10^{-4}	1.431×10^{-7}	0.84019
0.4496	14.62°	55.0°	3.831×10^{-4}	5.444×10^{-4}	7.816×10^{-4}	1.524×10^{-7}	0.89505
0.4496	14.62°	65.0°	3.831×10^{-4}	5.444×10^{-4}	1.511×10^{-3}	1.613×10^{-7}	0.94722
0.4496	14.62°	75.0°	3.831×10^{-4}	5.444×10^{-4}	4.104×10^{-2}	1.699×10^{-7}	0.99808

Table 31: Mean velocity, volumetric flow rate and dimensional flow parameters versus groove fill ratio ($h = 3.831 \times 10^{-4}$ m, $w = 3.445 \times 10^{-4}$ m, $\phi_0 = 7.0°$, $\tau_{lv}^* = 0.0$).

A_l/A_g	$\overline{v_0^*}$	V^*	F_1 (m^2)	F_2 (m^4)
0.00216	0.35025×10^{-1}	0.23545×10^{-1}	9.5703×10^{-12}	3.5158×10^{-21}
0.00913	0.35025×10^{-1}	0.23545×10^{-1}	4.0513×10^{-11}	6.3002×10^{-20}
0.02086	0.35025×10^{-1}	0.23545×10^{-1}	9.2535×10^{-11}	3.2869×10^{-19}
0.03737	0.35025×10^{-1}	0.23545×10^{-1}	1.6574×10^{-10}	1.0545×10^{-18}
0.10603	0.14748×10^{-1}	0.98748×10^{-2}	3.9763×10^{-10}	7.1783×10^{-18}
0.15833	0.20927×10^{-1}	0.15367×10^{-1}	7.6824×10^{-10}	2.0710×10^{-17}
0.21214	0.27194×10^{-1}	0.20498×10^{-1}	1.3031×10^{-9}	4.7065×10^{-17}
0.26785	0.32454×10^{-1}	0.24398×10^{-1}	1.9688×10^{-9}	8.9787×10^{-17}
0.32528	0.36072×10^{-1}	0.26669×10^{-1}	2.7022×10^{-9}	1.4966×10^{-16}
0.38419	0.38622×10^{-1}	0.27884×10^{-1}	3.4992×10^{-9}	2.2889×10^{-16}
0.44503	0.39823×10^{-1}	0.27979×10^{-1}	4.2948×10^{-9}	3.2542×10^{-16}
0.50757	0.40251×10^{-1}	0.27477×10^{-1}	5.0955×10^{-9}	4.4035×10^{-16}
0.57159	0.40053×10^{-1}	0.26559×10^{-1}	5.8784×10^{-9}	5.7208×10^{-16}
0.64063	0.46394×10^{-1}	0.34479×10^{-1}	6.8090×10^{-9}	7.4268×10^{-16}
0.71541	0.53536×10^{-1}	0.44431×10^{-1}	7.8572×10^{-9}	9.5705×10^{-16}
0.78100	0.59941×10^{-1}	0.54307×10^{-1}	8.7973×10^{-9}	1.1698×10^{-15}
0.84019	0.65595×10^{-1}	0.63933×10^{-1}	9.6271×10^{-9}	1.3771×10^{-15}
0.89505	0.70861×10^{-1}	0.73575×10^{-1}	1.0400×10^{-8}	1.5848×10^{-15}
0.94722	0.75803×10^{-1}	0.83295×10^{-1}	1.1125×10^{-8}	1.7942×10^{-15}
0.99808	0.80163×10^{-1}	0.92993×10^{-1}	1.1765×10^{-8}	2.0031×10^{-15}

Table 32: Dimensionless velocity, volumetric flow rate and Poiseuille number versus groove fill ratio ($h = 3.831 \times 10^{-4}$ m, $w = 3.445 \times 10^{-4}$ m, $\phi_0 = 7.0°$, $\tau_{lv,a}^* = 5.0$).

β	θ	ϕ	A_l/A_g	$\overline{v_a^*}$	V^*	Po
1.049	14.62°	7.0°	0.10603	0.44951	0.45997	0.30098
0.8991	14.62°	7.0°	0.15833	0.55128	0.52375	0.40480
0.7868	14.62°	7.0°	0.21214	0.61118*	0.46070*	0.56117*
0.6993	14.62°	7.0°	0.26785	0.65735**	0.49417**	0.57269**
0.6294	14.62°	7.0°	0.32528	0.66535	0.59419	0.49190
0.5722	14.62°	7.0°	0.38419	0.66313	0.60976	0.47876
0.5245	14.62°	7.0°	0.44503	0.64877**	0.45581**	0.62692**
0.4841	14.62°	7.0°	0.50757	0.62513	0.64739	0.42674
0.4496	14.62°	7.0°	0.57159	0.59685	0.66990	0.39574
0.4496	14.62°	15.0°	0.64063	0.62644	0.80169	0.46555
0.4496	14.62°	25.0°	0.71541	0.65255	0.95976	0.54157
0.4496	14.62°	35.0°	0.78100	0.66745	1.1183	0.60472
0.4496	14.62°	45.0°	0.84019	0.68388	1.2631	0.66656
0.4496	14.62°	55.0°	0.89505	0.69685	1.4068	0.72354
0.4496	14.62°	65.0°	0.94722	0.71080	1.5446	0.78105
0.4496	14.62°	75.0°	0.99808	0.72674	1.6838	0.84305

* Grid independence: 1.5%

** Grid independence: 1.2%

Table 33: Maximum heat transport predicted by the closed-form solution versus groove fill ratio (Straight axial grooves, no body forces, $T_{\text{sat}} = 40°C$, Ethanol)

A_l/A_g	Q_{cap} (W)		
	Semi-Analytical	Two-Point Numerical	No Shear
0.10598	0.13573	0.13570	0.13590
0.15830	0.39121	0.39097	0.39217
0.21209	0.88732	0.88654	0.89115
0.26782	1.6887	1.6867	1.7001
0.32519	2.8062	2.8028	2.8329
0.38408	4.2781	4.2732	4.3323
0.44492	6.0615	6.0553	6.1585
0.50745	8.1727	8.1669	8.3322
0.57146	10.578	10.575	10.822
0.64063	13.703	13.676	14.049
0.71520	17.609	17.541	18.093
0.78097	21.483	21.369	22.112
0.84028	25.247	25.072	26.027
0.89489	28.992	28.753	29.933
0.94715	32.759	32.449	33.879
0.99765	36.416	36.023	37.725

Table 34: Maximum heat transport predicted by the closed-form solution versus groove fill ratio (Straight axial grooves, no body forces, $T_{\text{sat}} = 40°$C, Water)

A_l/A_g	Q_{cap} (W)		
	Semi-Analytical	Two-Point Numerical	No Shear
0.10598	1.7825	1.7787	1.8044
0.15830	5.0811	5.0508	5.2059
0.21209	11.338	11.243	11.825
0.26782	21.130	20.902	22.545
0.32519	34.292	33.915	37.534
0.38408	50.924	50.408	57.333
0.44492	70.242	69.617	81.384
0.50745	92.136	91.584	109.92
0.57146	116.02	115.79	142.50
0.64063	147.75	145.45	184.52
0.71520	186.60	181.02	236.89
0.78097	224.33	215.29	288.62
0.84028	260.28	246.91	338.69
0.89489	295.11	277.51	388.35
0.94715	329.09	307.01	438.22
0.99765	361.03	333.96	486.54

Table 35: Maximum heat transport versus groove fill ratio for several working temperatures (Ethanol, $|\vec{a}_r| = 0.0$-g).

A_l/A_g	Q_{cap} (W)			
	$T_{\text{sat}} = 40°\text{C}$	$T_{\text{sat}} = 60°\text{C}$	$T_{\text{sat}} = 80°\text{C}$	$T_{\text{sat}} = 100°\text{C}$
0.10603	0.0	0.0	0.12	0.23
0.15833	0.20	0.35	0.61	1.13
0.21214	0.68	0.97	1.60	2.82
0.26785	1.47	2.09	3.26	5.55
0.32528	2.60	3.59	5.53	9.38
0.38419	4.03	5.61	8.58	14.46
0.44503	5.86	8.07	12.25	20.64
0.50757	7.89	10.98	16.66	27.97
0.57159	10.39	14.30	21.66	36.35
0.64063	13.49	18.63	28.12	47.21
0.71541	17.43	24.03	36.34	60.94
0.78100	21.30	29.40	44.42	74.44
0.84019	25.06	34.59	52.29	87.63
0.89505	28.85	39.79	60.19	100.85
0.94722	32.65	45.02	68.12	114.15
0.99808	36.32	50.13	75.85	127.22

Table 36: Maximum heat transport versus groove fill ratio for several working temperatures (Ethanol, $|\vec{a}_r| = 10.0$-g).

	Q_{cap} (W)			
A_l/A_g	$T_{\mathrm{sat}} = 40°C$	$T_{\mathrm{sat}} = 60°C$	$T_{\mathrm{sat}} = 80°C$	$T_{\mathrm{sat}} = 100°C$
0.10603	0.34	0.59	0.99	1.87
0.15833	1.29	1.92	3.11	5.63
0.21214	3.11	4.53	7.24	12.95
0.26785	6.07	8.73	13.93	24.80
0.32528	10.20	14.60	23.29	41.44
0.38419	15.59	22.44	35.66	63.40
0.44503	22.18	31.90	50.72	90.16
0.50757	30.00	43.16	68.63	121.94
0.57159	38.97	56.05	89.13	158.41
0.64063	50.55	72.77	115.67	205.61
0.71541	65.11	93.73	149.02	264.93
0.78100	79.15	114.49	182.12	323.73
0.84019	93.52	134.75	214.30	381.04
0.89505	107.55	155.01	246.58	438.41
0.94722	121.71	175.46	279.05	496.46
0.99808	135.45	195.30	310.81	552.75

Table 37: Maximum heat transport versus radial acceleration ($A_l/A_g = 0.5$).

	Q_{cap} (W)			
	Castle et al. (2000)			Present
$|\vec{a_r}|$ (g)	No Dryout	Partial Dryout	Analytical	Analytical
0.01	—	—	19	7.40
2.0	—	—	22	9.56
4.0	—	—	31	13.78
6.0	7.0	10.0	42	18.32
8.0	9.5	13.0	58	22.95
10.0	11.0	13.5	70	27.65

Table 38: Maximum heat transport versus radial acceleration ($A_l/A_g = 1.0$).

	Q_{cap} (W)			
	Castle et al. (2000)			Present
$|\vec{a_r}|$ (g)	No Dryout	Partial Dryout	Analytical	Analytical
0.01	17.3	25.4	20	34.97
2.0	17.3	25.4	24	44.64
4.0	32.7	40.0	39	70.29
6.0	59.1	64.5	52	98.07
8.0	88.2	96.4	75	138.04
10.0	106.4	110.9	92	172.67

Table 39: Mean velocity, Poiseuille number and volumetric flow rate versus shear stress at the liquid-vapor interface for various values of meniscus contact angle ($\beta = 0.5$, $w_l^*/2 = 0.25$, $P^* = 1.15245$).

ϕ	τ_{lv}^*	$\overline{v^*}$	Po	V^*
0°	-0.1	0.18878×10^{-2}	27.088	0.17394×10^{-3}
0°	-0.075	0.26896×10^{-2}	19.013	0.24782×10^{-3}
0°	-0.05	0.35104×10^{-2}	14.567	0.32344×10^{-3}
0°	-0.025	0.43465×10^{-2}	11.765	0.40048×10^{-3}
0°	0.0	0.51353×10^{-2}	9.9581	0.47316×10^{-3}
0°	0.0625	0.71345×10^{-2}	7.1676	0.65738×10^{-3}
0°	0.125	0.91525×10^{-2}	5.5873	0.84330×10^{-3}
0°	0.25	0.13188×10^{-1}	3.8774	0.12152×10^{-2}
0°	0.375	0.17224×10^{-1}	2.9689	0.15870×10^{-2}
0°	0.5	0.21260×10^{-1}	2.4053	0.19589×10^{-2}
0°	0.75	0.29332×10^{-1}	1.7434	0.27026×10^{-2}
0°	1.0	0.37404×10^{-1}	1.3672	0.34464×10^{-2}
0°	2.0	0.69691×10^{-1}	0.73377	0.64214×10^{-2}
25°	-0.1	0.32506×10^{-2}	27.245	0.39414×10^{-3}
25°	-0.075	0.41572×10^{-2}	21.303	0.50408×10^{-3}
25°	-0.05	0.50437×10^{-2}	17.559	0.61158×10^{-3}
25°	-0.025	0.59348×10^{-2}	14.923	0.71962×10^{-3}
25°	0.0	0.68259×10^{-2}	12.974	0.82768×10^{-3}
25°	0.0625	0.90536×10^{-2}	9.7820	0.10978×10^{-2}
25°	0.125	0.11229×10^{-1}	7.8870	0.13616×10^{-2}
25°	0.25	0.15650×10^{-1}	5.6588	0.18977×10^{-2}
25°	0.375	0.20072×10^{-1}	4.4123	0.24338×10^{-2}
25°	0.5	0.24493×10^{-1}	3.6158	0.29700×10^{-2}
25°	0.75	0.33336×10^{-1}	2.6566	0.40422×10^{-2}
25°	1.0	0.42179×10^{-1}	2.0997	0.51144×10^{-2}
25°	2.0	0.77551×10^{-1}	1.1420	0.94034×10^{-2}
50°	-0.1	0.45097×10^{-2}	27.149	0.64296×10^{-3}
50°	-0.075	0.54643×10^{-2}	22.406	0.77904×10^{-3}
50°	-0.05	0.64189×10^{-2}	19.074	0.91514×10^{-3}
50°	-0.025	0.73345×10^{-2}	16.693	0.10457×10^{-2}
50°	0.0	0.82746×10^{-2}	14.796	0.11797×10^{-2}
50°	0.0625	0.10625×10^{-1}	11.523	0.15148×10^{-2}
50°	0.125	0.12975×10^{-1}	9.4363	0.18498×10^{-2}
50°	0.25	0.17586×10^{-1}	6.9621	0.25072×10^{-2}
50°	0.375	0.22255×10^{-1}	5.5014	0.31728×10^{-2}
50°	0.5	0.26922×10^{-1}	4.5477	0.38382×10^{-2}
50°	0.75	0.36256×10^{-1}	3.3769	0.51690×10^{-2}
50°	1.0	0.45590×10^{-1}	2.6855	0.64998×10^{-2}
50°	2.0	0.82926×10^{-1}	1.4764	0.11823×10^{-1}
72.34°	-0.1	0.54127×10^{-2}	28.188	0.86146×10^{-3}
72.34°	-0.075	0.64152×10^{-2}	23.783	0.10210×10^{-2}
72.34°	-0.05	0.74177×10^{-2}	20.569	0.11805×10^{-2}
72.34°	-0.025	0.84202×10^{-2}	18.120	0.13401×10^{-2}
72.34°	0.0	0.94227×10^{-2}	16.192	0.14996×10^{-2}
72.34°	0.0625	0.11929×10^{-1}	12.790	0.18985×10^{-2}
72.34°	0.125	0.14354×10^{-1}	10.629	0.22844×10^{-2}
72.34°	0.25	0.19309×10^{-1}	7.9016	0.30730×10^{-2}
72.34°	0.375	0.24264×10^{-1}	6.2880	0.38618×10^{-2}
72.34°	0.5	0.29219×10^{-1}	5.2217	0.46504×10^{-2}
72.34°	0.75	0.39129×10^{-1}	3.8992	0.62276×10^{-2}
72.34°	1.0	0.49039×10^{-1}	3.1112	0.78048×10^{-2}
72.34°	2.0	0.88244×10^{-1}	1.7290	0.14044×10^{-1}

119

Table 40: Wetted perimeter, mean velocity, Poiseuille number and volumetric flow rate versus groove fill ratio for various values of groove aspect ratio ($\tau_{lv}^* = 0.0$, $\phi = 0°$).

β	w_l^*/w^*	P^*	$\overline{v^*}$	Po	$\dot{V}^*$
0.25	0.1	0.0731191	0.13005×10^{-4}	8.4006	0.35142×10^{-8}
0.25	0.2	0.223950	0.20221×10^{-3}	9.6365	0.70676×10^{-6}
0.25	0.3	0.450806	0.63058×10^{-3}	11.141	0.84242×10^{-5}
0.25	0.4	0.734032	0.12616×10^{-2}	12.059	0.40386×10^{-4}
0.25	0.5	1.04707	0.20592×10^{-2}	12.514	0.12238×10^{-3}
0.25	0.6	1.36011	0.29299×10^{-2}	12.849	0.27336×10^{-3}
0.25	0.7	1.64333	0.38585×10^{-2}	12.871	0.49958×10^{-3}
0.25	0.8	1.87019	0.47149×10^{-2}	12.940	0.77004×10^{-3}
0.25	0.9	2.02102	0.55519×10^{-2}	13.346	0.10799×10^{-2}
0.25	0.999	2.09364	0.74536×10^{-2}	15.203	0.18573×10^{-2}
0.5	0.1	0.114187	0.35380×10^{-5}	9.4469	0.82578×10^{-9}
0.5	0.2	0.288528	0.19851×10^{-3}	8.4052	0.82718×10^{-6}
0.5	0.3	0.531454	0.10922×10^{-2}	8.7511	0.20062×10^{-4}
0.5	0.4	0.827649	0.28055×10^{-2}	9.3706	0.13311×10^{-3}
0.5	0.5	1.15245	0.51353×10^{-2}	9.9581	0.47316×10^{-3}
0.5	0.6	1.47724	0.78593×10^{-2}	10.398	0.11735×10^{-2}
0.5	0.7	1.77344	0.10755×10^{-1}	10.780	0.22962×10^{-2}
0.5	0.8	2.01636	0.13817×10^{-1}	11.282	0.38892×10^{-2}
0.5	0.9	2.19070	0.17762×10^{-1}	12.443	0.64680×10^{-2}
0.5	0.999	2.30389	0.25467×10^{-1}	14.698	0.12692×10^{-1}
0.75	0.1	0.160025	0.11137×10^{-5}	10.092	0.21124×10^{-9}
0.75	0.2	0.367435	0.10959×10^{-3}	8.9207	0.44516×10^{-6}
0.75	0.3	0.634966	0.93568×10^{-3}	8.4299	0.18655×10^{-4}
0.75	0.4	0.951588	0.31271×10^{-2}	8.5312	0.17184×10^{-3}
0.75	0.5	1.29509	0.67001×10^{-2}	8.8579	0.74738×10^{-3}
0.75	0.6	1.63860	0.11328×10^{-1}	9.2444	0.21238×10^{-2}
0.75	0.7	1.95522	0.16731×10^{-1}	9.7209	0.46642×10^{-2}
0.75	0.8	2.22275	0.23143×10^{-1}	10.489	0.89608×10^{-2}
0.75	0.9	2.43016	0.32404×10^{-1}	11.885	0.17278×10^{-1}
0.75	0.999	2.58868	0.47659×10^{-1}	13.997	0.35626×10^{-1}
1.0	0.1	0.207697	0.45992×10^{-6}	10.367	0.73744×10^{-10}
1.0	0.2	0.453879	0.59860×10^{-4}	9.4362	0.22830×10^{-6}
1.0	0.3	0.752420	0.66244×10^{-3}	8.7481	0.13415×10^{-4}
1.0	0.4	1.09559	0.27276×10^{-2}	8.4926	0.16081×10^{-3}
1.0	0.5	1.46369	0.67927×10^{-2}	8.5590	0.84758×10^{-3}
1.0	0.6	1.83180	0.12785×10^{-1}	8.8427	0.27842×10^{-2}
1.0	0.7	2.17497	0.20665×10^{-1}	9.3068	0.69688×10^{-2}
1.0	0.8	2.47351	0.31143×10^{-1}	10.106	0.15279×10^{-1}
1.0	0.9	2.71969	0.46597×10^{-1}	11.485	0.32778×10^{-1}
1.0	0.999	2.92539	0.69923×10^{-1}	13.281	0.69692×10^{-1}